Containment of Radioactive Material in the Z, ZX, and X-1 Facilities: Progress Report for the Period January 1, 1999 to December 31, 1999

R.R. Peterson, G.L. Kulcinski, M.H. Anderson, M.L. Corradini,
D.A. Haynes, D.L. Henderson, D.C. Kammer, H.Y. Khater, P. McKenna,
E.A. Mogahed, G.A. Moses, K. Olson, G.A. Rochau, J.F. Santarius,
C. Sauer, M.E. Sawan, I.N. Sviatoslavsky, T. Utschig, P.P.H. Wilson, J. Yuan

December 1999

UWFDM-1124

FUSION TECHNOLOGY INSTITUTE

UNIVERSITY OF WISCONSIN

MADISON WISCONSIN

Containment of Radioactive Material in the Z, ZX, and X-1 Facilities: Progress Report for the Period January 1, 1999 to December 31, 1999

R.R. Peterson, G.L. Kulcinski, M.H. Anderson, M.L. Corradini, D.A. Haynes, D.L. Henderson, D.C. Kammer, H.Y. Khater, P. McKenna, E.A. Mogahed, G.A. Moses, K. Olson, G.A. Rochau, J.F. Santarius, C. Sauer, M.E. Sawan, I.N. Sviatoslavsky, T. Utschig, P.P.H. Wilson, J. Yuan

Fusion Technology Institute
Department of Engineering Physics
University of Wisconsin-Madison
1500 Engineering Drive
Madison, WI 53706

December 1999

UWFDM-1124

1. Introduction

There has recently been a great deal of progress in the physics and technology of Z-pinch generated x-rays. These x-rays can be used to study the basic properties of matter under high pressures and at high temperatures. In addition, the x-rays can be used to drive fusion targets to ignition and beyond, thus opening up the possibility of thermonuclear reactors in the not so distant future. As the energy released increases from kJ's to MJ's to 100's of MJ's, a serious concern surrounds the viability of the chamber that is needed to contain the microexplosion.

The Fusion Technology Institute (FTI) at the University of Wisconsin-Madison was asked to address the general issues surrounding the chamber needed to contain large energy releases in the Z, ZX, and eventually X-1 devices. There is a wide range of topics that could be considered and the FTI has chosen a small subset for initial examination. This report summarizes the work performed in CY 1999 on those subjects.

It is important to recognize that there is an important feedback between the engineering issues and the fundamental design of the targets, experiments, and Z-pinch related hardware. Therefore, we have deliberately spent some of our effort in modeling the target performance, target output, and interaction of the target debris with the chamber walls (Sections 3 and 5). The transport of the radiation from the target to the solid members inside the chamber is also an important input to our work and that is described in Section 3.

The target chamber of ZX or X-1 must allow the injection of tens of MA's. One option is the use of a vacuum insulator stack, which also serves as a vacuum boundary. These insulator rings will not only be required to hold off a voltage of 10 MV, but will also have to withstand external static loads on an evacuated chamber in addition to the pulsed internal loads from the energy released by the target. We have considered some possible solutions to this problem in Section 6.

The release of neutrons and the activation that they cause in the chamber is also an important area of investigation. Section 7 scopes out the problem of the loss of neutrons from the backlighter of the Z device. Some of the fundamental experiments using a Z pinch facility include equation of state (EOS) studies of actinides. These materials must be contained during and after the shots. Section 8 outlines the level of release that may be acceptable from a regulatory standpoint although a "zero release" policy should be vigorously pursued. Section 9 addresses the movement and potential release of activated "dust" from ports in a containment chamber. Experiments and simulations from the University of Wisconsin Shock Tube facility give us an idea of the timescales and particle size dependence of the phenomena.

Sections 10 and 11 discuss some possible experiments that could be performed on the existing Z facility. The aim of these proposed experiments is to measure the EOS of certain inert gases, as well as to quantitatively measure the degree of fragmentation of targets and internal components.

Mechanical analysis of Z, ZX, and X-1 began with some preliminary work to identify accelerometer locations for proposed vibration experiments to be conducted on Z. The purpose of the experiments is to identify the source of the severe shock observed during the firing of Z. It is hoped that by identifying the source, steps can be taken to suppress its effects in Z and especially in new machines that are more powerful.

On the structural analysis side, hardware was purchased and software was leased to couple detailed CAD models of Z, ZX, and X-1 with structural dynamic analyses and state of the art animation programs. Three students are currently working on the project to couple the three-dimensional structural model from Pro Engineer™ with both ANSYS™ transient finite element simulations of Z chambers and the animation program, MAYA™. The preliminary results with Z have shown that the SGI computer platform, model 320, has more than enough speed and memory to allow rapid manipulation, in Pro Engineer™, of complex shapes, such as MITL, post-hole convolutes, etc. Procedures for the implementation of full transient finite element analyses have been developed, and several reduced analysis methods are under consideration. Preparations are now being made to apply this technology to the analysis of Z and the eventual design of ZX and X-1.

2. Mechanical Analysis of Experiments for Z, ZX and X-1 – Z Vibration Experiment Design

Eleven different locations have been identified at which it would be desirable to have measurements in various directions. Figure 2.1 illustrates the locations numbered 1 through 11. The selected locations, for the most part, run radially from the central part of Z out to the north wall. Having most of the accelerometers along a radial line such as this might allow the study of wave travel times in the structure and help detect the source of the shock. Basically, locations on all of the major Z structural components were selected. Table 2.1 gives a detailed listing of the locations and the desired measurement directions. The location number roughly corresponds to the importance of the location (1 being the most important) in the event that there is a need to limit the number of accelerometers. Currently, this candidate set contains 26 accelerometers. Locations 8 and 9 were added to the set at 90° with respect to the radially oriented locations to check the symmetry of the shock. Locations 10 and 11 were added to study the response of the wall and the crane.

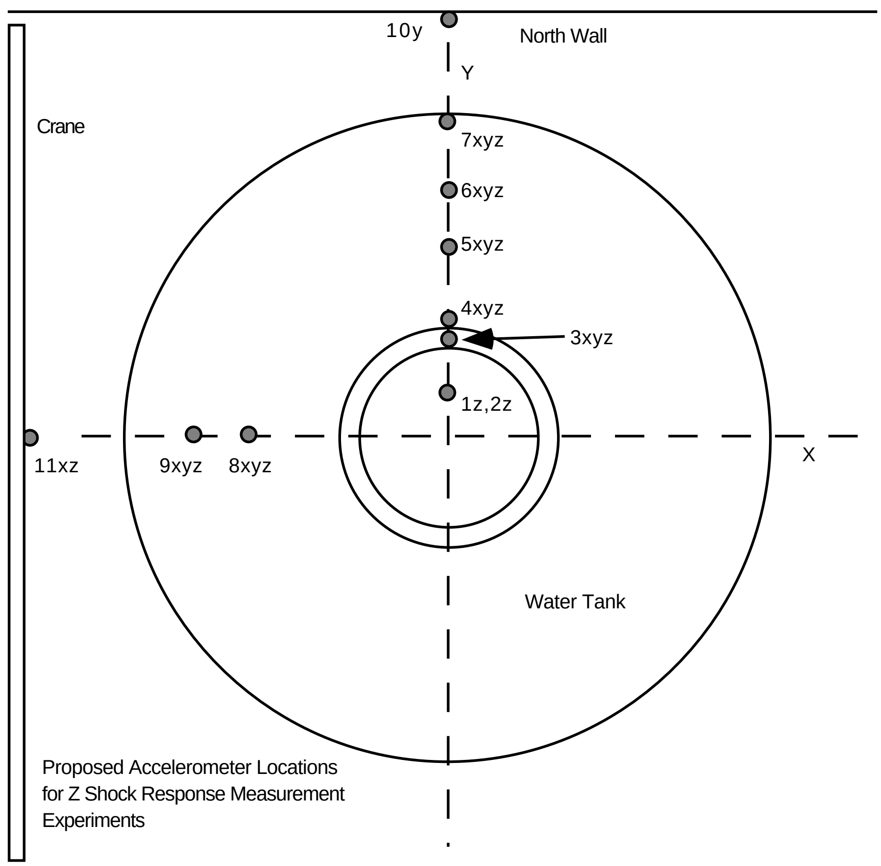

Figure 2.1. Proposed accelerometer locations for Z vibration experiments.

Table 2.1. Proposed accelerometer locations for Z vibration experiments.

Location Number	Directions	Description
1	z	Top MITL, make sure accelerometer axis is mounted parallel to the vertical axis.
2	z	Bottom MITL.
3	xyz	Bottom of circular beam at base of vacuum chamber.
4	xyz	Inside wall of vacuum chamber below water line.
5	xyz	Bottom of water tank, can be on underside.
6	xyz	Housing surrounding water switch
7	xyz	Outer wall of water tank.
8	xyz	Bottom of water tank, can be on underside.
9	xyz	Housing surrounding water switch.
10	y	North wall by crane track.
11	Xz	Face of crane

2.1 Solid Model Manipulation and Animation

Considerable progress has been made toward coupling the finite element models in Pro Engineer™ version 20 with detailed structural dynamic analyses of Z carried out with ANSYS™ 5.5. In addition, the output from the Pro Engineer™ code is being integrated with the MAYA™ animation code. The objective of this work is to eventually develop a complete package that will be applied toward the structural design of the ZX and X-1 target chambers as well as producing high-end visualization videos of the design options.

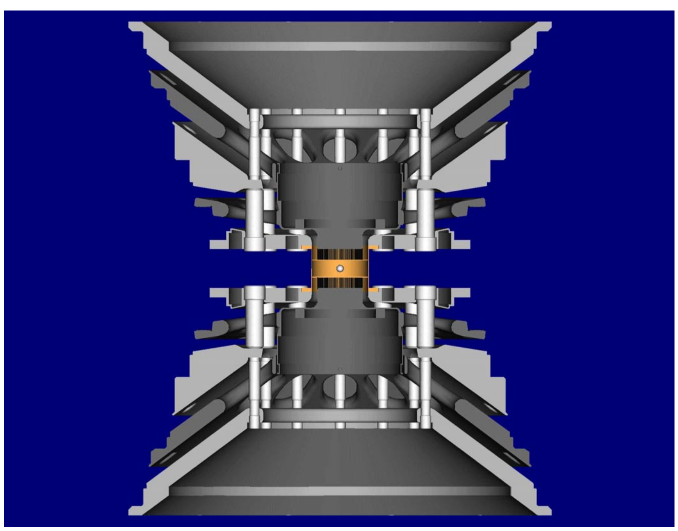

Figure 2.2. Pro Engineer™ model of the Z convolute assembly.

Two students have been involved in the solid model manipulation and animation aspects of the project, and an SGI model 320 computer platform has been purchased to perform the necessary work. License agreements for Pro Engineer™ and MAYA™ have been put in place. The students have been using a series of SNL generated, Pro Engineer™ files of Z component assemblies to demonstrate the ability to rapidly manipulate complex shapes. The Z convolute assembly, shown in Figure 2.2, has been used as a test case for model manipulation. In addition, various local experimental fusion facilities have been modeled from 2D drawings in preparation for the more complex job of modeling of conceptual ZX components. These models are now being integrated into the MAYA™ program to demonstrate the final link in the integration.

2.2 Structural Dynamic Analysis

The goal of the structural dynamic analysis thrust of this task is to perform transient finite element analyses of the Z, ZX, or X-1 chambers using meshes generated directly from Pro Engineer™ models. To this point, work on the structural dynamic analysis has been focused on the refinement of ANSYS™ modeling and transient analysis techniques. A basic finite element model of the lower spool of the Z Vacuum Stack Assembly, part no. R47901-000, has been created in ANSYS™. This component, highlighted in Figure 2.3, was selected because it provided a simple structure and finite element mesh that could be used to evaluate the transient analysis capabilities of ANSYS™ and to practice the application of theses techniques to a structure.

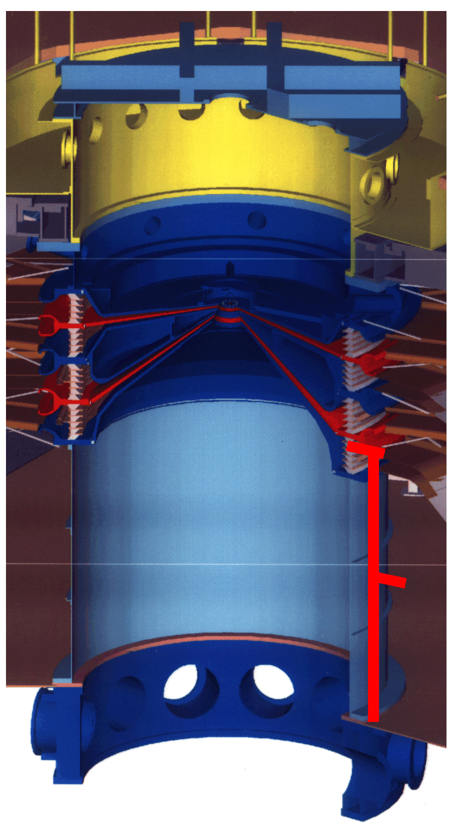

Figure 2.3. Existing Z Vacuum Stack Assembly with the lower spool highlighted.

Since the Pro Engineer™ work was in its early stages at the time of the initiation of the structural dynamic analysis, this finite element model was generated manually within the ANSYS™ preprocessing environment. Dimensions of the spool were estimated from component drawings provided by SNL, and the structure was assumed to be constructed from 304 stainless steel. The walls of the spool were modeled using elastic shell elements, 3-D structural solid elements were used to represent the upper and lower flanges of the spool, and 3-D tapered unsymmetrical beam elements were included to model the wall reinforcement rings. The shell elements were meshed using automated routines, but the solid elements in the flanges and the beam elements had to be meshed node-by-node to ensure correct connectivity and element orientation. In addition, special care had to be taken to ensure that the automatic meshing routine created an array of shell elements with all element normal vectors directed radially outward from the cylinder's axis of symmetry. The final model consisted of 1382 elements and 7344 degrees of freedom.

Modal analyses were conducted in ANSYS™ to validate the finite element model of the lower spool. First, the free-free mode shapes were investigated and ANSYS™ was forced to compute all of the rigid body modes. Next, the upper and lower flanges were constrained and the mode shapes corresponding to the first 30 natural frequencies were extracted.

Figure 2.4 displays the mode shapes corresponding to the first and the 30th natural frequencies of the structure. These computed mode shapes and frequencies were then compared to analytical results derived from the expressions presented in *Formulas for Natural Frequency and Mode Shape*, by Robert Blevins. Since the computed mode shapes and frequencies showed good agreement with the analytical predictions and no mechanisms were revealed, the finite element model was deemed acceptable for use in more complex analyses.

Using the lower spool model, a full transient structural analysis was then performed. In the full transient analysis, the lower spool model was subjected to a pressure load profile taken from predicted target explosion effects on the X-1 target chamber. Initially, the extremely small time steps, approximately 1×10^{-10} seconds, caused some difficulty with the Newton-Raphson integration algorithm used by ANSYS™. Modification of one integration parameter proved successful in alleviating this difficulty. Standard ANSYS™ post-processing functions were used to examine the deformed shape and corresponding stress distributions produced by the applied pressure load profile.

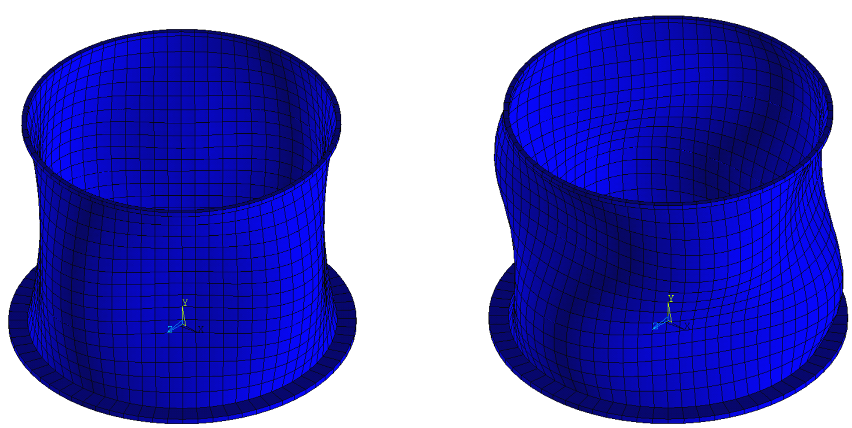

Figure 2.4. First, at right, and 30th mode shapes, for constrained lower spool, with frequencies corresponding to 53 Hz and 112 Hz, respectively.

The peak-deformed shape can be found in Figure 2.5 and the contours of Von Mises stresses corresponding to the peak displacement are shown in Figure 2.6.

Current work involves the implementation of several reduced transient analysis methodologies. Since the full transient analysis in ANSYS™ predicts the behavior of a structure by sequentially solving the full set of structural equations at each time step, this approach is costly in terms of memory and computation time. To reduce the costs of transient structural analysis, alternate techniques that solve smaller equation sets are often utilized. ANSYS™ mode superposition analyses are being implemented as a first step toward the application of reduced analysis techniques. In the near term, the structural dynamics work will be focused upon a comparison of the accuracy of the results produced by mode superposition, designation of master degrees of freedom, and mode acceleration with the results from the full transient analysis. Work will also begin on the importation of complete finite element models into ANSYS™ directly from Pro Engineer™.

In addition, consideration has been given to the incorporation of nonlinear material behavior in the finite element analyses, in an effort to simulate strain-rate effects in the structure. ANSYS™ does have the ability to simulate strain-hardening behavior in full transient analyses, but this feature can only be applied to 3-D solid elements. Since the eventual finite element models of Z, ZX, and X-1 will be modeling such large and complex structures, it is unlikely that these models will be formed using solid structural elements. It is believed that the exclusion of strain hardening from the material constitutive model is conservative from a structural failure standpoint. It also seems to be common practice in containment vessel design and analysis. Thus, no further efforts will be undertaken to incorporate strain rate effects directly in the finite element solutions.

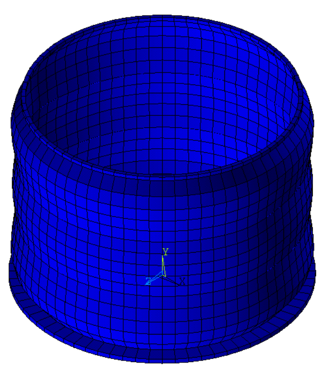

Figure 2.5. Peak deformed shape of the Z lower spool model subjected to a blast load.

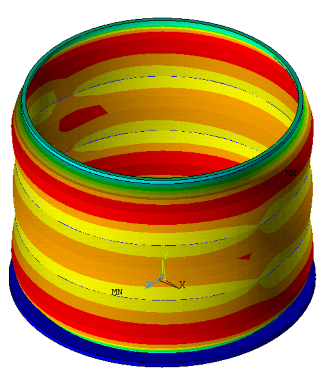

Figure 2.6. Von Mises stress distribution corresponding to the peak displacement.

3. Target Capsule Implosion Calculations

One of the critical inputs into the design and analysis of an experimental chamber for ZX and/or X-1 is the energy output from ignited and burning targets. To obtain target output spectra and powers, we have decided to use the BUCKY computer code. The first step in calculating target output is obtaining the conditions at the time of ignition and burn in the capsule. We are also using BUCKY for these calculations. First, we performed simulations of implosion on burn near to published capsule designs [1] to show that BUCKY is a credible code. Then we turned our attention to the X-1 capsule and show preliminary results giving 160 MJ of yield. This target is based on the z-pinch driven static-wall hohlraum target concept [2,3]. In the future, we will show results for ZX targets and do target output calculations for specific ZX target designs.

Our first task is to show that BUCKY does a credible job of capsule implosion and burn. There are published implosion and burn calculations done for NIF capsules with reduced drive conditions [1]. The reduced NIF conditions imply 900 kJ absorbed in the hohlraum. In these calculations, only the capsule is modeled and it is performed in 1-D spherical geometry. The implosions are driven by an applied radiation temperature history at the outside of the capsule. Shocks are launched through the capsule, which must approximately coalesce at the inside edge of the frozen fuel for a minimum entropy implosion. The published and the BUCKY calculations are all performed on slightly different capsules with slightly different drive histories. In the case of BUCKY calculations, many small adjustments to the radiation drive history and target geometry were made to achieve the proper shock timing to get ignition. The LLNL capsule used a graded Cu dopant in a Be ablator [1]. SNL [2,3] and UW capsule designs use a 2% O dopant in a Be ablator. The implosions stagnate in high ρR assemblies with hot inner spark plugs. The fuel burns, producing a thermonuclear yield.

In Table 3.1, BUCKY calculations are compared with the published results based on energy coupled into the ablator, ρR, and yield. The BUCKY target design optimization led both designs to higher peak drive radiation temperatures, had more energy absorbed in their ablators and gave higher yields. In Figure 3.1, the two UW NIF capsule designs are shown. The two capsules are very similar, with the 270 eV target having a larger outer radius and ablator thickness by 5 μm. The capsules are driven by the radiation temperature histories shown in Figure 3.2. The pulse shapes are carefully adjusted to launch four shocks that sequentially exit the DT vapor/DT ice interface in rapid succession.

In the 260 eV design, approximately 70 BUCKY calculations were performed to optimize the shock timing, where very small changes in the drive history lead to large changes in the target yield. The implosion hydrodynamics for the 260 eV design are shown in Figure 3.3. Three shocks break through the interface between 13 and 14 ns. Bang time is seen to be about 17.3 ns. The peak ρR of

Table 3.1. Summary of NIF Reduced Drive Capsule Implosion Calculations

	LLNL Graded Cu	SNL Be 2% O	BUCKY Be 2% O	BUCKY Be 2% O
Peak Drive Temperature (eV)	250	250	260	270
Outer Radius (mm)	1.088	1.100	1.080	1.085
Albator Thickness (mm)	0.122	0.140	0.110	0.115
Fuel Ice Thickness (mm)	0.055	0.080	0.070	0.070
Energy to Capsule (kJ)	114	125	131	135
Peak Fuel ρR (g/cm^2)	1.28	1.5	1.42	1.53
Fusion Yield (MJ)	6.8	12	19.6	19.6

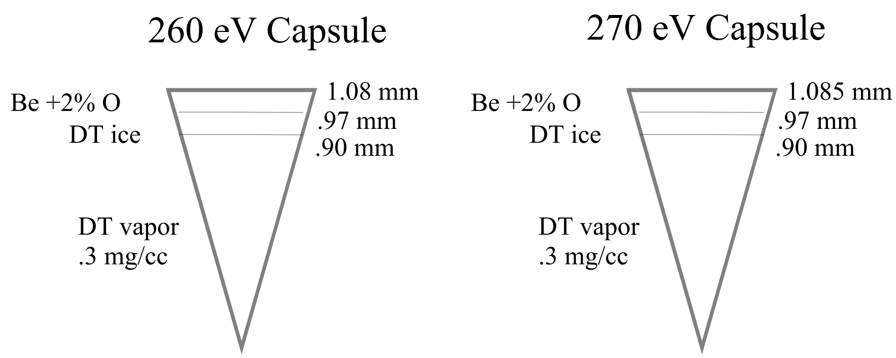

Figure 3.1. UW reduced drive NIF capsule designs.

1.42 g/cm^2 is reached at this time. Over less than 30 ps, 19.6 MJ of thermonuclear fusion occur, which rapidly drives the capsule outward after bang time. In Figure 3.4, the mass density profiles during the implosion are seen. The imploding shell gets very thin shortly after the shock breakout of the ice/vapor interface, which leads to a high in-flight aspect ratio (IFAR), shown as a function of time in Figure 3.5. The peak mass density increases during the implosion, reaching a peak of about 2000 g/cm^3. The peak IFAR is about 35 at 14 ns. This may or may not be low enough to avoid damaging fluid instabilities. These calculations show that BUCKY allows the design of a capsule close to the LLNL and SNL designs and that the BUCKY predicted behavior of the capsules is not dissimilar for what LLNL and SNL might predict.

The X-1 capsule and drive history obtained from Rick Olson of SNL is shown in Figure 3.6. The capsule is twice as wide as the NIF capsules. The ablator has a layer of BeO outside a layer of $Be_{98}O_2$. This structure is designed to be a pulse-shaping layer. The drive history in X-1 cannot have the fine details of a NIF history because X-1 uses z-pinch x-rays. Therefore, internal pulse shaping is needed. The pulse shaping relies on the time it takes for the radiation to burn through the O dopants in the ablator. For BUCKY to predict reasonable capsule behavior, it must get the atomic physics of burnthrough right. This is done within opacity tables created by EOSOPA for BUCKY. SNL predicted that this capsule would ignite for this drive history and give about 200 MJ of yield. The results of the BUCKY simulation are shown in Figure 3.7, where the implosion hydro is shown. The shock timing predicted by BUCKY is less than perfect, but it still predicts 160 MJ of yield, which is reasonable. Different equations of state are used by BUCKY than at SNL, so differences in shock timing are not unexpected.

The NIF and X-1 results show that BUCKY is ready to design a capsule for ZX, which is the next step.

References for Section 3

[1] T.R. Dittrich, S.W. Haan, M.M. Marinak, S.M. Pollaine, and R. McEachern, "Reduced Scale National Ignition Facility Capsule Design," Phys. Plasmas, 5, 2708 (1998).

[2] R.J. Leeper, et al., "Z-pinch Driven Inertial Confinement Fusion Target Physics Research at Sandia National Laboratories," 17th IAEA Fusion Energy Conf. (Yokohama, Japan, 19-24 October 1998).

[3] R.E. Olson, et al., "Evaluation of a Z-pinch Driven ICF Concept," 40th Ann. Meeting APS Div. Plas. Phys. (New Orleans, LA, November 16-20, 1998).

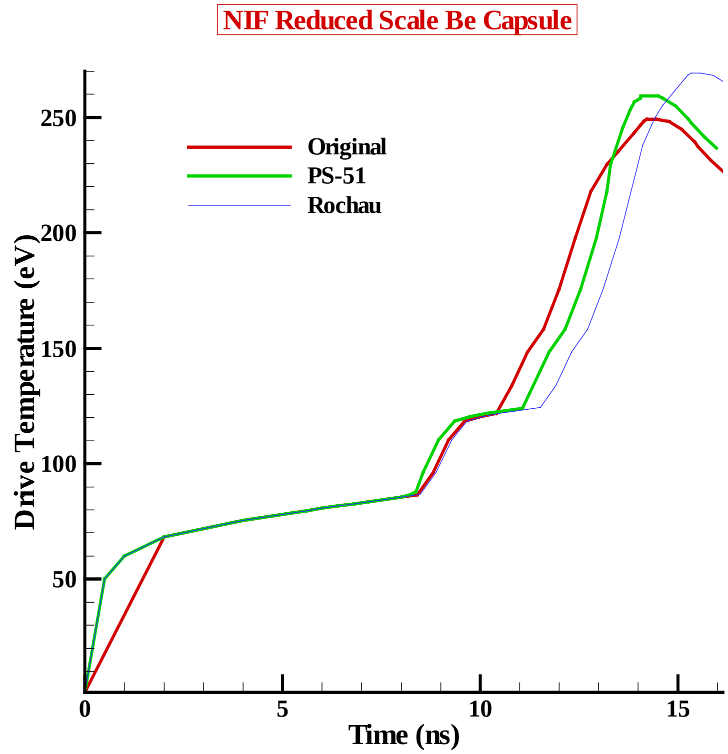

Figure 3.2. Drive radiation temperature histories for UW reduced drive NIF capsules.

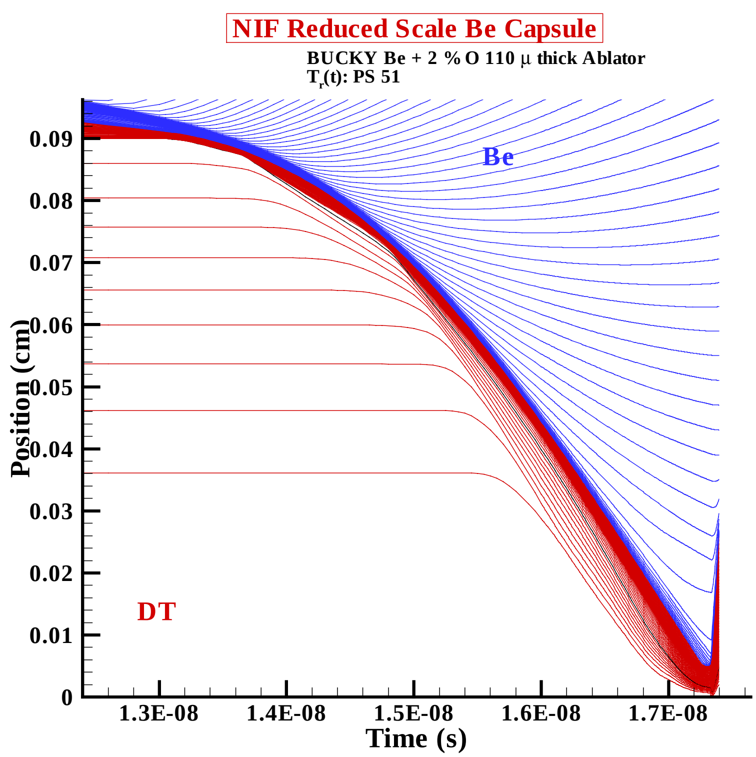

Figure 3.3. BUCKY code reduced NIF drive capsule with a BeO ablator implosion and burn simulation: Lagrangian zone boundaries in capsule versus time. Target yield is 19.6 MJ.

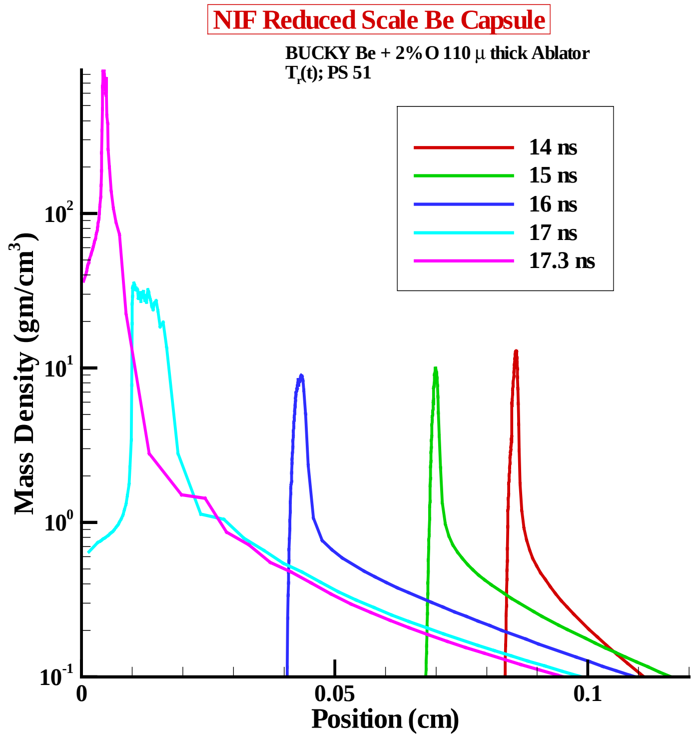

Figure 3.4. Mass density profiles in an implosion and burn BUCKY simulation of a reduced NIF drive capsule with a BeO ablator.

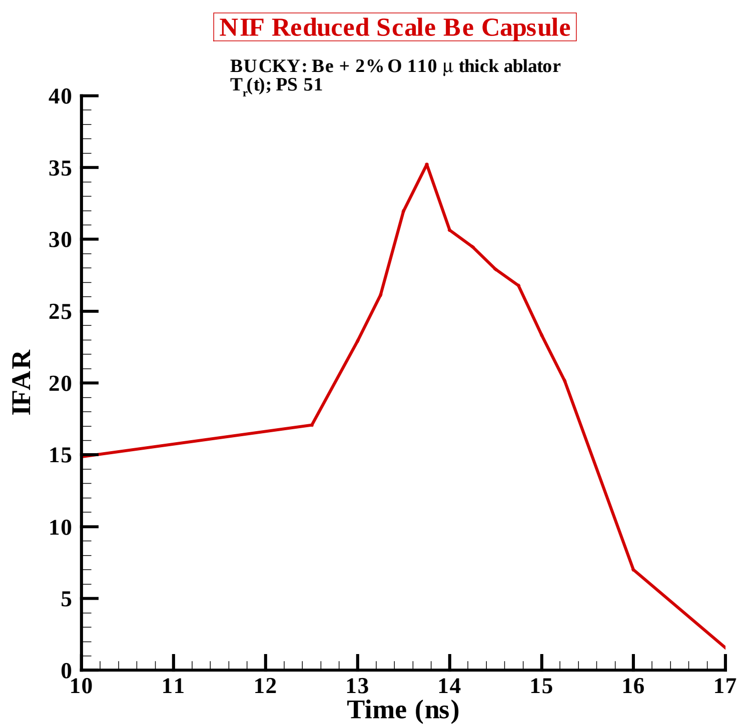

Figure 3.5. In-flight aspect ratio for an implosion and burn BUCKY simulation of a reduced NIF drive capsule with a BeO ablator.

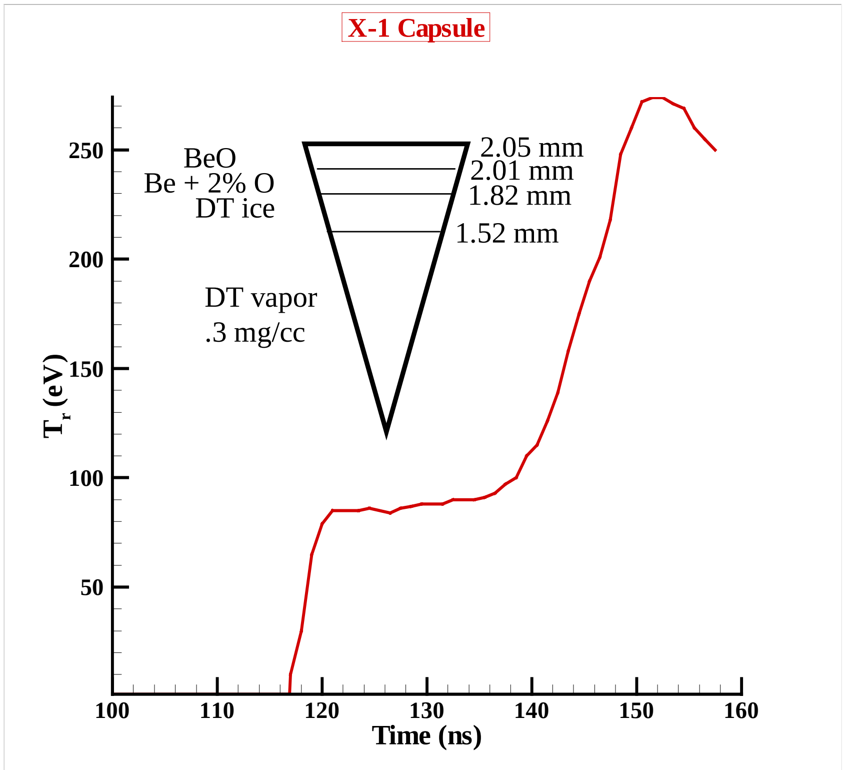

Figure 3.6. X-1 drive temperature history and X-1 capsule design.

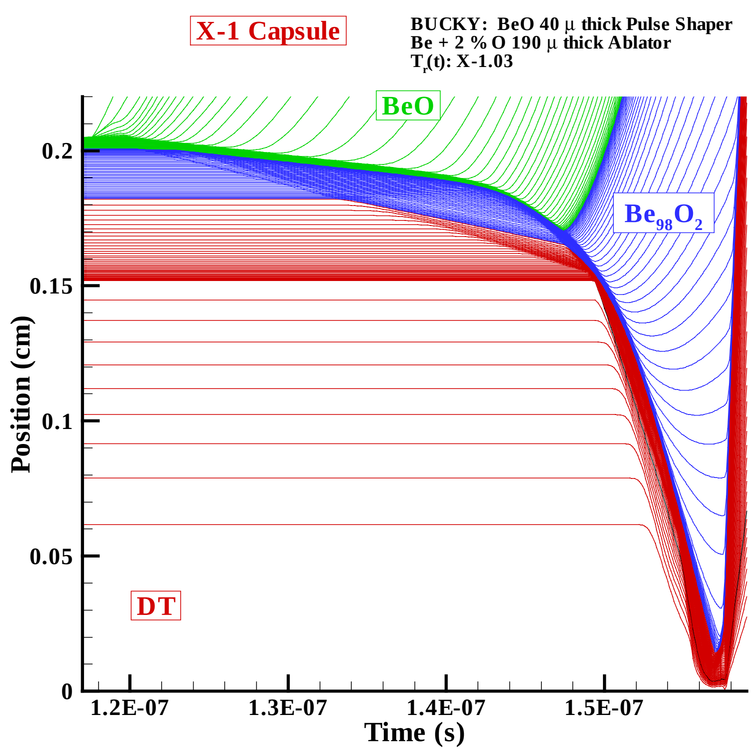

Figure 3.7. X-1 target implosion and burn simulation: Lagrangian zone boundaries in capsule versus time. Target yield is 160 MJ.

4. Integral Transport Theory

From the initial illumination of the target capsule to its subsequent burn and disassembly, radiation transport plays an important role throughout the compression, ignition and burn phases of inertial fusion energy (IFE) capsules [1]. Time-dependent diffusion based methods have frequently been used to simulate radiation transport within these target capsules [2,3,4]. It is well known that these methods have difficulty describing the radiation field in optically thin media because of the infinite propagation speed of the radiation in the diffusion approximation [1]. Various methods have been devised to remedy these problems; foremost, flux-limited diffusion methods that seek to limit the propagation speed of the radiation [5,6]. Though improvements have been made, the optically thin regime still poses some problems for diffusion-based methods.

The time-dependent Angle Integrated Integral Transport (AIIT) method has been shown to achieve highly accurate results for neutral particle transport in optically thick and thin regions with finite propagation speeds [7,8,9,10]. Central to the AIIT method are the time-dependent single-collision kernels. These kernels contain Heaviside or delta functions that provide causality information for the neutral particle's transport [7]. A neutral particle at a position r' at a time t' traveling with a speed v cannot affect the intensity at a position r at a time t until enough time has passed for its translation. This is expressed by the condition (t - t') = |r - r'| / v, the argument of the Heaviside function. This method has been adapted to radiation transport and has been used to examine the uniformity of x-ray radiation illumination on a DT capsule as the radiation enters through the ends caps and is re-emitted for the walls of a NOVA hohlraum [11,12]. Although the AIIT method produced accurate results, the drawbacks of the method are the potential CPU and storage requirements. To increment in time, one must integrate back from time zero to the current time of interest. This can be quite CPU and storage intensive depending on the length of the simulation and size of the program. A time-dependent angle dependent Integral Transport time-step method was developed to circumvent this problem.

4.1.1 Derivation of Calculational Method

The Time-Dependent Bubble Integral Transport (TBIT) is a time-step method based on the angular radiation intensity integral equation. It only requires information from the previous time step improving the simulation time and reducing the storage requirements over that of the AIIT method. The transport equation for x-rays in a given frequency group in a heterogeneous medium with an arbitrary isotropic source is:

$$\left(\frac{1}{c}\frac{\partial}{\partial t} + \hat{\Omega}\cdot\vec{\nabla} + \Sigma\right) I\left(\vec{r},\Omega,v,t\right) = \frac{Q\left(\vec{r},t\right)}{4\pi} \qquad \text{(Eq. 4.1)}$$

Applying the method of characteristics to Equation 4.1, one obtains a first order differential equation as a function of the neutral particle's path lengths:

$$\frac{d}{ds}\left[I\left(\vec{r}_o + s\hat{\Omega},\hat{\Omega},v,t_o + \frac{s}{c}\right)\exp\left[\int^{s}\Sigma\left(\vec{r}_o + s'\vec{\Omega},v\right)ds'\right]\right] = \exp\left[\int^{s}\Sigma\left(\vec{r}_o + s'\hat{\Omega},v\right)ds'\right]Q\left(r_o' + s'\hat{\Omega},\Omega' v,t_o + \frac{s}{c}\right) \qquad \text{(Eq. 4.2)}$$

One now integrates back one spatial mesh where the time-step is defined as $\Delta x = v_g/\Delta t$ and c is the speed of light, arriving at

$$I(\vec{r},\hat{\Omega},v,t) = \int_o^{\Delta r}\left[e^{-r(\vec{r}-s\hat{\Omega},v,t)}Q\left(r_o' + s\hat{\Omega},\hat{\Omega},v,t_o + \frac{s}{c}\right)\right]ds'$$
$$+I(r' - \Delta x\hat{\Omega},\hat{\Omega}v,t-\Delta t)e^{-r(\vec{r},\hat{\Omega}v,t)}. \qquad \text{(Eq. 4.3)}$$

The assumption is now made that all the scattering in the system is isotropic in the center of mass coordinate system (i.e., no scattering angles are preferred); then expanding the source term into its constituent components of its collided and uncollided sources, the following is arrived at:

$$I(\vec{r},\hat{\Omega},v,t) = \int_o^{\Delta r} e^{-r(\vec{r}-s\hat{\Omega},v,t)}\left[\Sigma_s(\vec{r},\hat{\Omega},v,t)\Phi(\vec{r},\hat{\Omega},v,t) + S_o(\vec{r},\hat{\Omega},vt)\right]ds'$$
$$+I_{boundary}(\vec{r} - \Delta x\hat{\Omega},\hat{\Omega},v,t-\Delta t)e^{-r(\vec{r}-s\hat{\Omega},v,t)}. \qquad \text{(Eq. 4.4)}$$

Figure 4.1 shows Equation 4.4 from a visual standpoint. The TBIT method calculates the time-dependent scalar flux at a particular point by drawing a sphere of radius one Δr around the calculational point. Thus, only particles that scatter during the current time-step into the calculational angle, or particles that are on the boundary of the sphere during the previous time-step will influence the angular flux at the current time-step. The scattered component is calculated by integrating along the line of sight until the boundary of the "sphere" or material/vacuum boundary is met. The boundary component is calculated through simple exponential attenuation along the line of sight (Figure 4.1).

In a simplistic manner, the scalar flux could be calculated by solving Equation 4.4 along specific angular directions and then integrating these directions in order to solve for the scalar flux. After each time-step, the boundary source term is updated and the calculation can proceed with only the information from the previous time-step needed. Details of the numerical implementation of the TBIT method can be found in Reference 12.

4.2 TBIT Applications to ICF Problems

The TBIT method will be used to simulate two problems pertaining to radiative transport in ICF targets. The first application will calculate 3D radiative transport in a spherical hohlraum. This is done to investigate the effect that the placement and size of the laser entrance holes have on the non-uniformity of the illumination on the capsule. The second application will be that of neutron transport down a diagnostic beam tube that measures the energy spectrum based on the time of flight from the fusion event to the detector. This will show how scattering events in the tube affect the perceived energy spectrum by scattering into lower energy groups and increasing the distance over which neutrons must travel.

4.2.1 Three-D Radiation Transport On Spherical Hohlraums

One of the routes to high gain targets and ignition is through the use of thin wall cylindrical hohlraums composed of a high Z material, usually gold, that surrounds a DT target suspended in the center. Laser energy enters through two laser entrance holes (LEH) on either side of the cylinder and proceeds to heat up the high Z material of the hohlraum resulting in the production of x-rays. The x-rays then irradiate the capsule as well as other portions of the hohlraum not directly heated by the laser energy. These "secondary" zones then proceed to emit x-rays of their own. Under ideal circumstances, the capsule is illuminated as uniformly as possible. For a capsule to properly

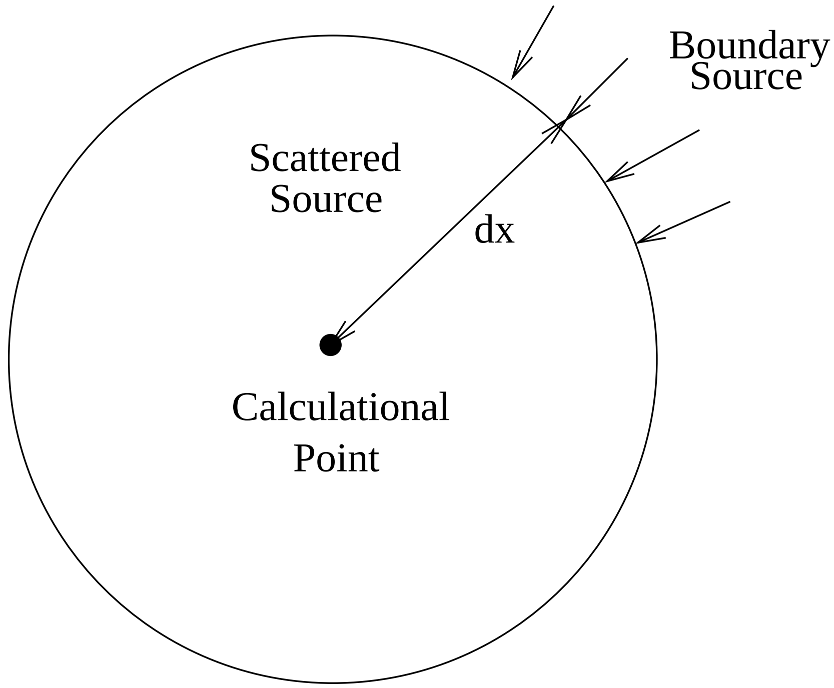

Figure 4.1. Graphical representation of TBIT method.

compress and initiate fusion, the non-uniformity of the x-ray illumination must be on the order of 1% [13].

In general, a cylindrical hohlraum has a length that is greater than its diameter. This type of geometry is needed to balance the lack of an x-ray source at the LEH with the large source caused by the lasers striking the hohlraum and the resultant x-ray emission.

An alternate design would be to make the hohlraum spherical instead of cylindrical and aim the lasers into the hohlraum such that they illuminate the area beyond the LEH. In contrast to cylindrical hohlraums, where beam phasing is needed to ensure a uniform illumination, spherical hohlraums can use identical temporal beam histories thereby producing more symmetrical capsule illuminations [14]. There are several disadvantages to using spherical hohlraums [14]:

- Beam placement for spherical hohlraums may be incompatible with cylindrical hohlraum designs.
- The hydrodynamics and radiative transport is more difficult to model in three-dimensional spherical coordinates.
- There may be greater radiative losses because of the added number of LEH.

When designing spherical hohlraums several considerations must be made when determining the area of the LEH as compared to the total area of the hohlraum. Ideally, the lasers should convert all of their energy into x-rays in the interior of the hohlraum. Obviously, total conversion is impossible; however, the LEH must be large enough such that the lasers enter the hohlraum unimpeded by the plasma ablation near the LEH.

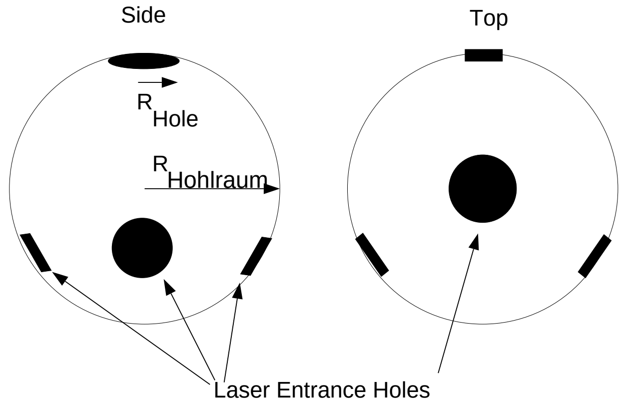

Figure 4.2. Proposed NIF spherical hohlraum.

On the other hand, an ideal design should also allow all of the x-ray energy to be transported into the capsule. This means that the LEH be as small as possible to avoid x-ray losses. These two design considerations are in direct conflict with one another. When balancing these two criteria, the overriding consideration must be the uniformity of the capsule illumination.

Provided in Table 4.1 and shown in Figure 4.2 are the proposed dimensions for a spherical hohlraum on the NIF [13].

Table 4.1. Proposed spherical hohlraum design for NIF.

Case Radius	R_c(mm)	4.55
Hole Radius	R_h (mm)	1.14
Capsule Radius	R_{cap} (mm)	1.13
R_{cap}/R_c		0.25
Case Area	A_c(mm^2)	243.8
Total Hole Area	A_h(mm^2)	16.33
A_h/A_c		0.067

The proposed spherical hohlraum for the NIF has four holes placed at the vertices of a tetrahedron, or known as a tetrahedral hohlraum. Although there have been different proposed angles for the LEH on the NIF tetrahedral hohlraum, the calculations will proceed using LEH that are uniformly distributed over the surface of the hohlraum at 60° angles from each other.

The TBIT method is used to investigate the uniformity of the capsule illumination for three different spherical hohlraum designs: 1) two LEH holes at either pole on the hohlraum, the NIF tetrahedral hohlraum, and 2) a six-hole design with two LEHs on either pole and four uniformly distributed LEHs on the equator. The total surface area will be the same for all three designs.

The figure of merit when determining the uniformity of the capsule illumination is the area of the LEH verses the total area of the hohlraum. For each of the three geometry types, three different LEH surface areas will be run. The first will have a LEH surface area of 50% that of the NIF design, the second equal to the NIF design, and the final 200% that of the NIF. The code will then calculate the capsule illumination for each of the three geometry types and for each of the three LEH surface areas.

Several complications arise when using the TBIT method. First, the LEH, not positioned at either pole of the spherical hohlraum, cannot be modeled as circular using the currently implemented TBIT method. The coordinate system for the code is defined at the center of the capsule and the material boundaries on the hohlraum can only change at discrete values for the azimuthal and polar angles. As a result, the area of these LEH are “arcs” on the hohlraum with areas of $A_{LEH} = P^2 d\theta d\phi$. These LEH holes have the same area as those at the poles with the only difference coming in the shape of the hole. The TBIT method was run using the numerical parameters shown in Table 4.2.

Table 4.2. Numerical parameters for TBIT method.

Nodes in Radial Direction	20
dr (mm)	0.2275
dt (picosecond)	0.758
Nodes in Polar Direction	40
Nodes in Azimuthal Direction	20

Several simplifying assumptions are made. First, the capsule is assumed to be completely black. This means that any incident x-ray flux will be absorbed and not transported through the capsule. This need not necessarily be the case. Real opacities could be used for the DT target. However, as the TBIT method is not coupled to a hydrodynamics code and the opacities and geometry for the problem are fixed, radiation would just travel through the capsule and affect the illumination on the other side. The present calculations are to determine the capsule illumination as a result of the x-ray flux incident on the capsule, and any “from the rear” illumination would distort the results.

Second, because the material changes on discrete nodes, the capsule in the simulation is slightly larger than the NIF target given in Table 4.2. For this particular problem, there are 20 nodes scattered uniformly in the interior of the hohlraum, dr=0.2275 mm. The capsule in the interior is completely black to all radiation and is composed of the inner five nodes, or 1.14 mm.

Only a signal frequency will be transported for the purpose of this simulation. This will allow the determination of the effect that the LEH size and placement has on the uniformity of the capsule illumination.

A uniform, isotropic, unit source will be distributed over each LEH. All of the outgoing photons from the LEH are pointed towards the hohlraum. Once the photon flux intersects with the hohlraum, 80% of the incoming intensity will be isotropically remitted as x-rays at the next time-step.

4.2.2 Two Laser Entrance Holes

The first simulation is of a spherical hohlraum with identical dimensions to that of the NIF hohlraum given in Table 4.1 including the total surface area of the LEH. The simulated two LEH hohlraum is shown in Figure 4.3.

Figure 4.4 shows the capsule illumination at 27.32 picoseconds. Figure 4.5 shows the capsule mapped onto a 2D plane. At this early time, x-rays have just enough time to travel from the LEH to the hohlraum and then to the capsule. The effect of the LEH is noticeable from both pictures as a

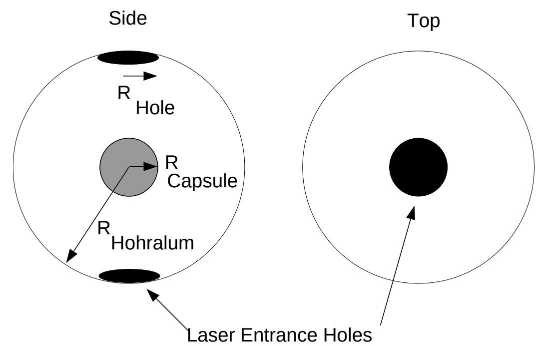

Figure 4.3. Two laser entrance hole spherical hohlraum.

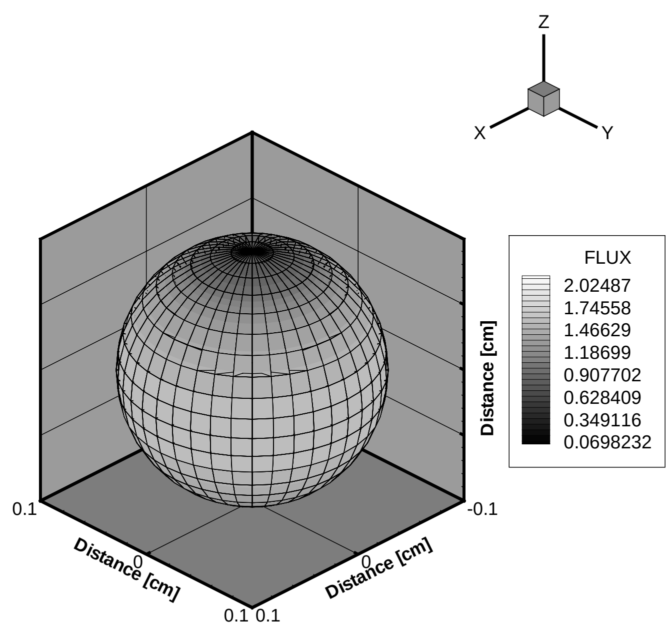

Figure 4.4. Two LEH capsule at 27.32 picoseconds.

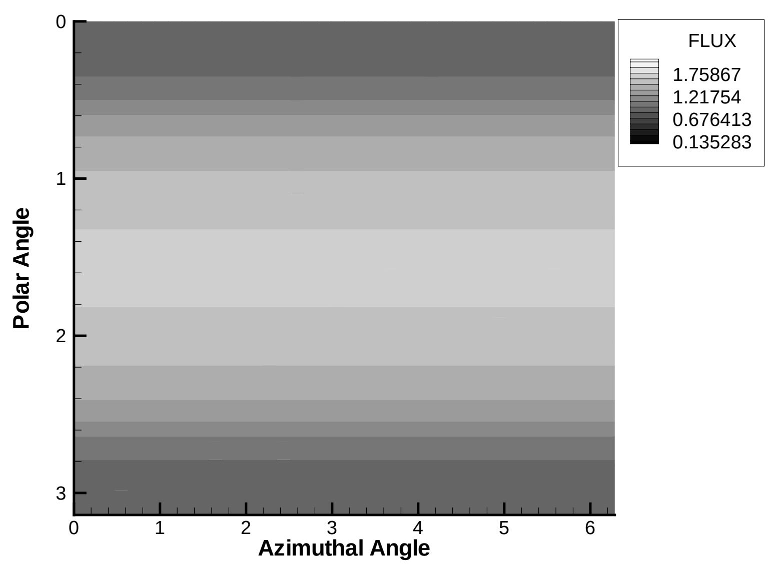

Figure 4.5. Two LEH capsule at 27.32 picoseconds.

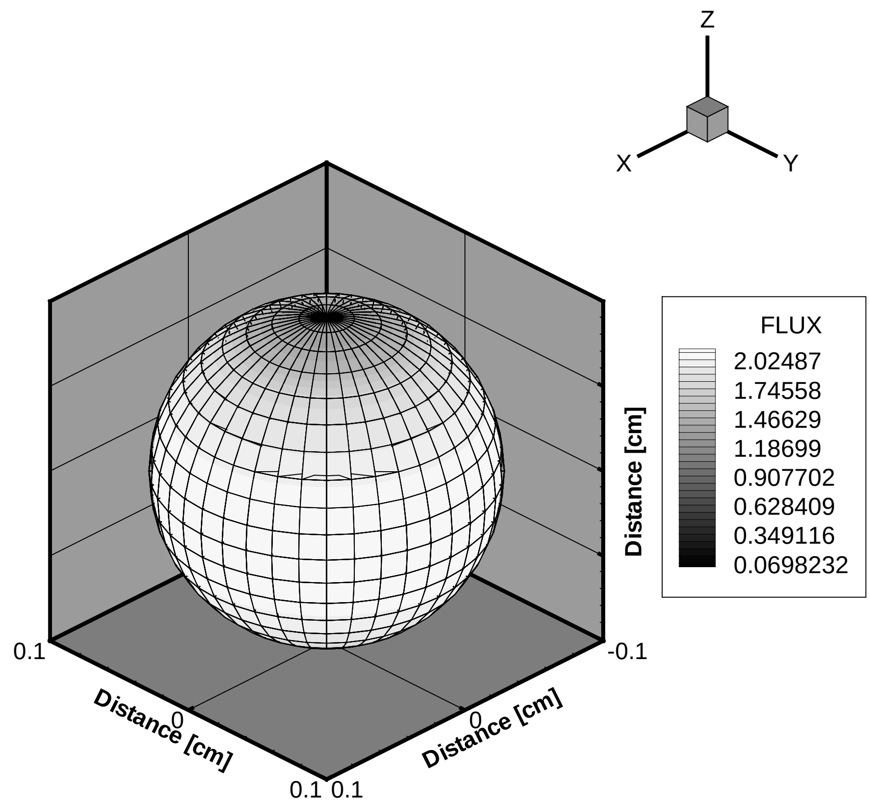

Figure 4.6. Two LEH capsule at 59.19 picoseconds.

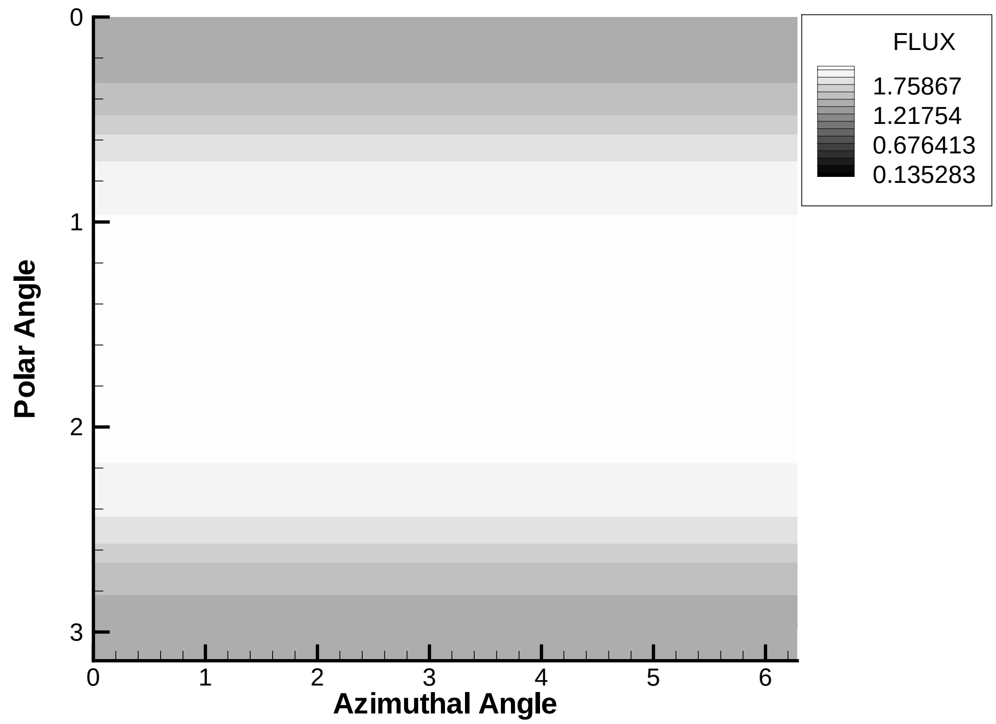

Figure 4.7. Two LEH capsule at 59.19 picoseconds.

large “cool” area located on either pole of the capsule. The middle of the capsule has the highest illumination because it is the only area that can be illuminated by both of the LEHs.

Figures 4.6 and 4.7 show the capsule illumination at 59.19 picoseconds. At this later time, x-rays can travel approximately twice across the diameter of the hohlraum. The basic features from the earlier time are featured in these two later figures. The LEH holes are the coolest regions of the capsule and the warmest is along the equator.

Two additional scenarios were run using the same two-holed LEH, with the only difference coming in the total surface area of the LEH. The first case was run with half the surface area of the NIF design and the second was run with twice the surface area. Table 4.3 compares the percent non-uniformity for each of the three cases.

Table 4.3. RMS non-uniformity for two-hole hohlraum.

Total Hole Area (mm^2)	RMS Non-uniformity (%)	Percentage Increase RMS Non-uniformity
8.17	12.04	-
1633	18.80	56.15
32.66	28.35	50.79

As expected, the smaller the LEH, the more uniform the capsule illumination. The third column of Table 4.3 shows the percent increase in the rms non-uniformity over the previous surface area configuration. The TBIT method predicts that doubling the LEH surface area will approximately double the capsule non-uniformity. From the data calculated, the two-LEH design is clearly unfavorable for successful implosions, as the best capsule illumination is over 10%, well above the 1% needed for successful implosion.

4.2.3 Four LEH “Tetrahedral” Hohlraum

The proposed spherical NIF hohlraum was simulated, Table 4.2 and show previously in Figure 4.2. Recall that the LEH holes that lay off the poles of the hohlraum are represented as “arc” on the hohlraum instead of circular holes.

Figures 4.8 and 4.9 show the capsule illumination at 27.32 picoseconds. At early times, the capsule illumination is fairly uniform except over the LEH. As expected, the portion of the capsule that has the most direct line of sight to the LEH is the coolest.

Figures 4.10 and 4.11 show the capsule illumination at 59.19 picoseconds. At this time, the hottest portion of the capsule are the three areas that are between the four LEH. At these locations, the capsule's surface has the greatest view of the hohlraum without LEH. As expected, the coolest regions are those that lay directly below the LEH. Schnittman ran a similar NIF tetrahedral capsule illumination using the *Buttercup* view-factor code. The calculated results showed a similar illumination pattern to that presented as the steady-state illumination patterns in Figures 4.9 and 4.10 [14].

As for the two-holed spherical hohlraum case, the tetrahedral hohlraum was run using identical conditions; however, the surface area of the LEH was changed. The smallest surface area is 50% that of the proposed NIF design, the middle value is the nominal case, and the largest is 200% of the NIF.

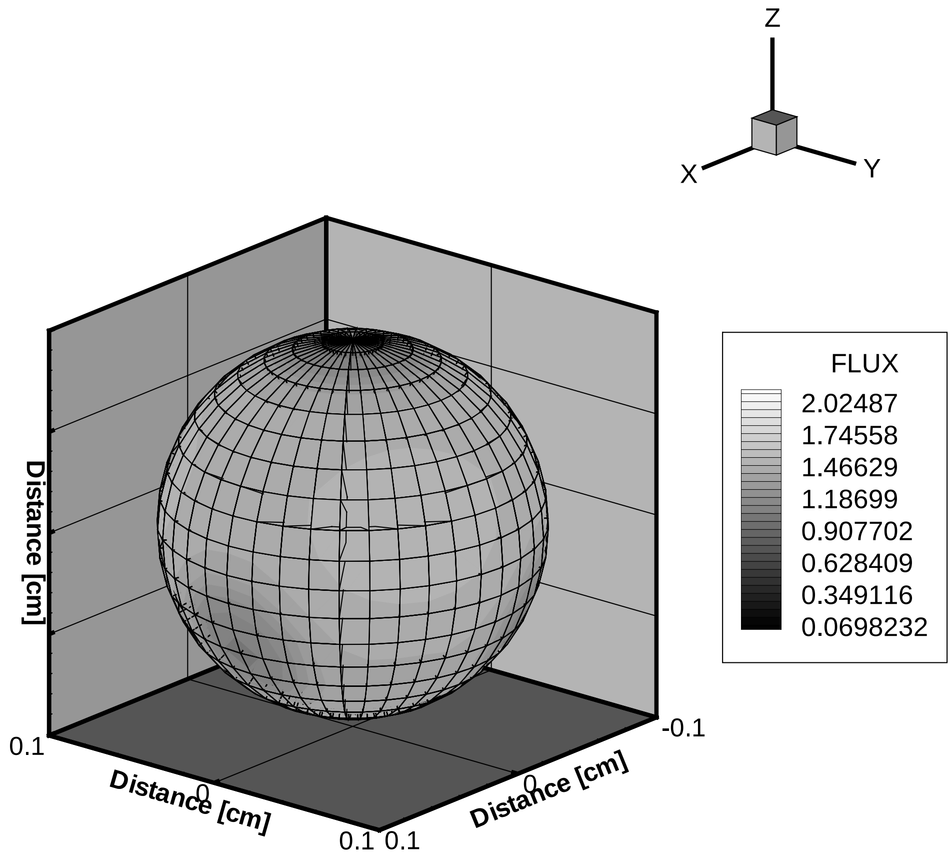

Figure 4.8. Four LEH capsule at 27.32 picoseconds.

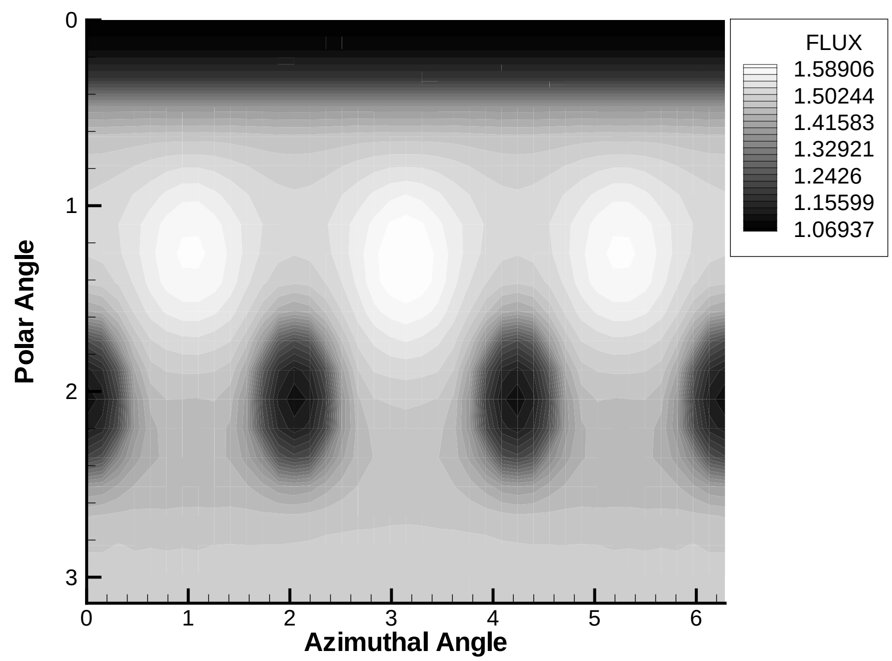

Figure 4.9. Four LEH capsule at 27.32 picoseconds.

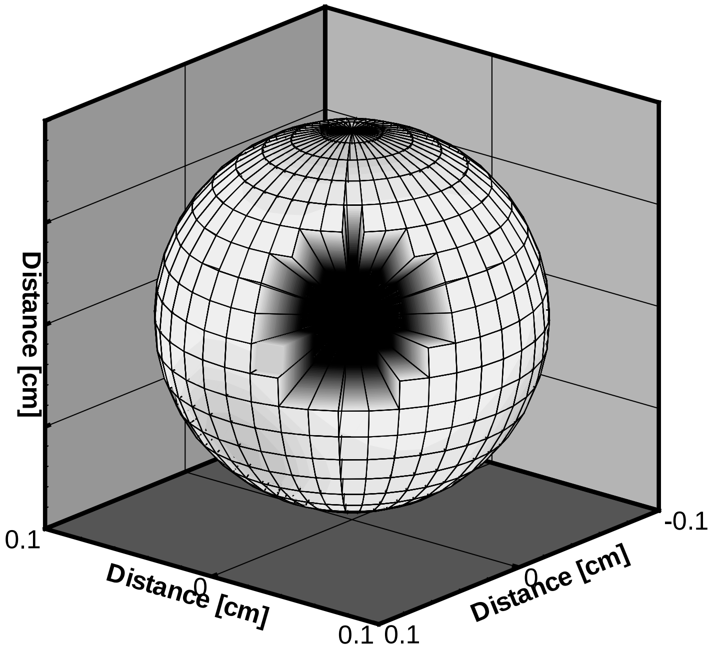

Distance [cm]
0.1
Distance [cm]
0
0.1
0.1
0
Distance [cm]
-0.1

Table 4.4. RMS non-uniformity for four-hole hohlraum.

Total Hole Area (mm^2)	RMS Non-uniformity (%)	Percentage Increase RMS Non-uniformity
8.17	5.76	-
16.33	6.55	13.72
332.66	10.94	67.02

As expected, the smaller the LEH the more uniform the capsule illumination. The third column of Table 4.4 shows the percent increase in the rms non-uniformity over the previous surface area configuration. TBIT predicts that the NIF tetrahedral hohlraum lays within an optimal range of LEH area to total hohlraum surface area. A reduction of 50% for the surface area of the LEH decreases the non-uniformity by 13.72%, whereas doubling the LEH area increases the non-uniformity by 67.02%.

Clearly, this capsule design is better than the two LEH presented earlier, as the illumination now varies over the capsule by a couple percent. The tetrahedral design has smaller radius LEH than the two-holed design. The smaller LEH mean that any given point that lays with the “shadow” of the LEH can see more of the x-ray source on the hohlraum.

4.2.4 Six Laser Entrance Hole Hohlraum

The final simulation is that of a six LEH hohlraum. The simulated six LEH hohlraum is shown in Figure 4.12. Again, as in the previous two cases the surface area is identical to the NIF design.

Figures 4.13 and 4.14 show the capsule illumination at 27.32 picoseconds. As with the tetrahedral design, the illumination over the capsule is fairly uniform except over the LEH. Figure 4.15 shows that the “shadow” cast by the square panel LEH is oval on the capsule. This shows that the radiative transport within the hohlraum tends to soften any hard edges.

After 59.19 picoseconds (Figures 4.15 and 4.16), the capsule illumination has reached 95% the magnitude of the steady state illumination and the illumination pattern has stabilized. The coolest areas are the regions on the capsule directly facing the LEH. As in the previous cases, the hottest portion of the capsule is the portion that lies between the LEH. For the six-LEH hohlraum, there are 12 hot spots on the capsule.

The six-LEH design was run with the same geometric configuration but with 50% and 200% of the surface area of the NIF design. As expected, the smaller the holes, the more uniform the capsule illumination. The non-uniformity for the six-hole hohlraum is less than the previous two cases for all surface areas. This is expected as the greater number of holes for a given surface area should provide a better capsule illumination.

Table 4.5. RMS non-uniformity for six-hole hohlraum.

Total Hole Area (mm^2)	RMS Non-uniformity (%)	Percent Increase RMS Non-uniformity
8.17	4.46	-
16.33	5.79	29.82
32.66	9.43	62.87

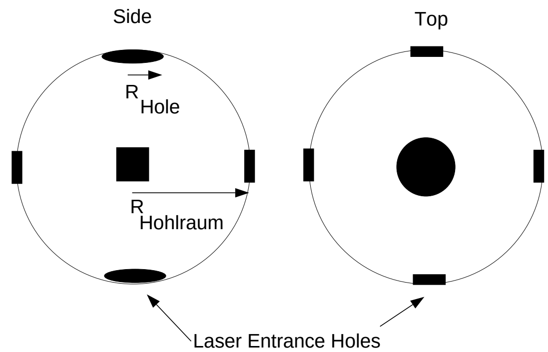

Figure 4.12 Six laser entrance hole spherical hohlraum.

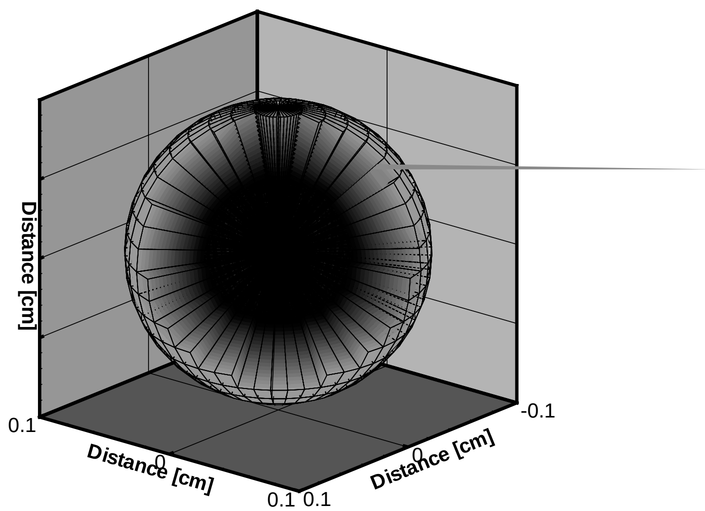

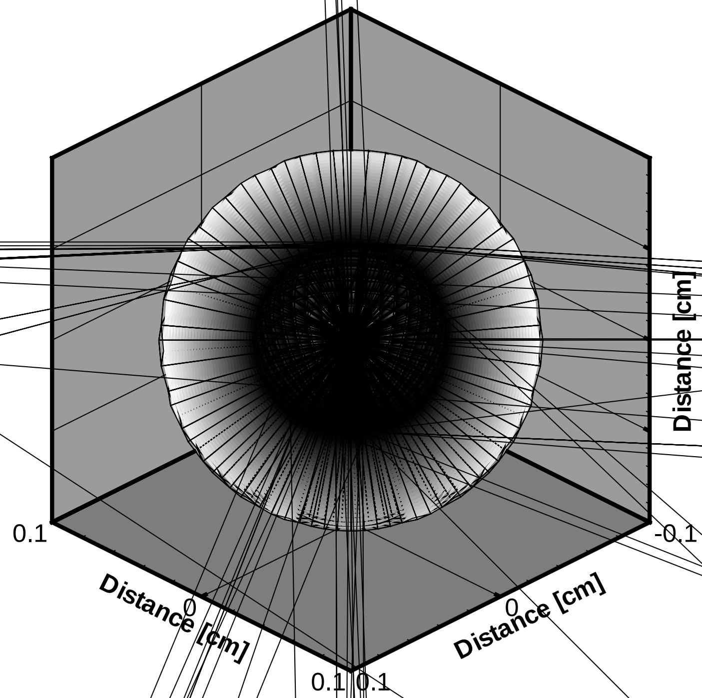
Distance [cm]
0.1
0
Distance [cm]
0.1 0.1
0
Distance [cm]
-0.1

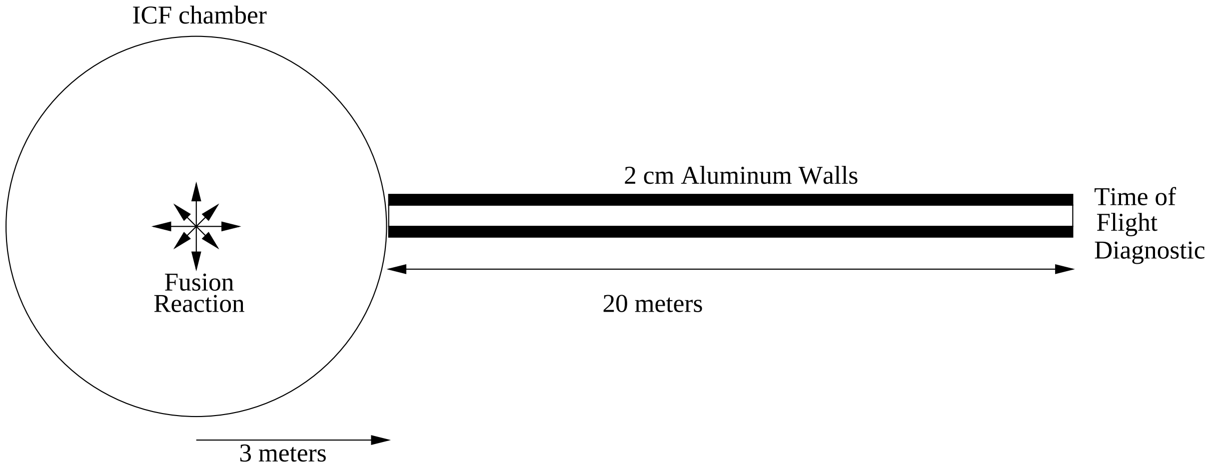

Figure 4.17. Neutron time of flight system – 1.

As with the tetrahedral design, as the surface area of the LEH is halved, the non-uniformity of the capsule illumination only decreases by 29.82%. Whereas once the surface area is doubled, the non-uniformity increases by 62.87%.

4.2.5 Two-D Simulation of Neutron Time of Flight Diagnostic

A second application to which the TBIT method will be applied is the neutron time of flight diagnostics found on experimental ICF systems. Simply put, these diagnostic devices determine the energy spectrum of an ICF target by using neutron time-of-flight techniques. Hence, the energy of the neutrons can be easily determined knowing the length from the target and the time that it takes for neutrons to arrive at the target.

Figure 4.17 shows the simple ICF time of flight diagnostic that was simulated. The fusion reaction occurs in a target chamber that has a three-meter radius. The time of flight diagnostic tube is made out of aluminum with a thickness of 2 cm. The tube is 20 meters long. As the TBIT method cannot model cylindrical geometries the time-of-flight tube is modeled using Cartesian coordinates. Thus, the tube is simulated as two parallel slabs of aluminum.

The neutrons entering the tube, because of the radius of the ICF chamber and the diameter of the neutron diagnostic, have a spread of 19° as shown in Figure 4.18.

This means that neutrons entering the tube are not necessarily traveling directly down the tube. As a result, particles can travel down the tube in several different methods. These are shown in Figure 4.19. Neutrons that enter the tube very nearly radially outward can travel directly down the diagnostic tube without undergoing any collisions with the walls (case 1).

However, particles that enter the diagnostic tube in a 0.25° arc to either side of vertical will interact with the wall once before they reach the detector. These particles could then scatter in such a way that they are angled back down the tube and towards the detector (case 2). Particles that arrive at the detector, after having scattered one or more times, appear to arrive with a lower energy. These scattered neutrons have traveled a longer distance to the detector and even if they retain their initial velocity will arrive later than a similar particle that travels directly down the tube.

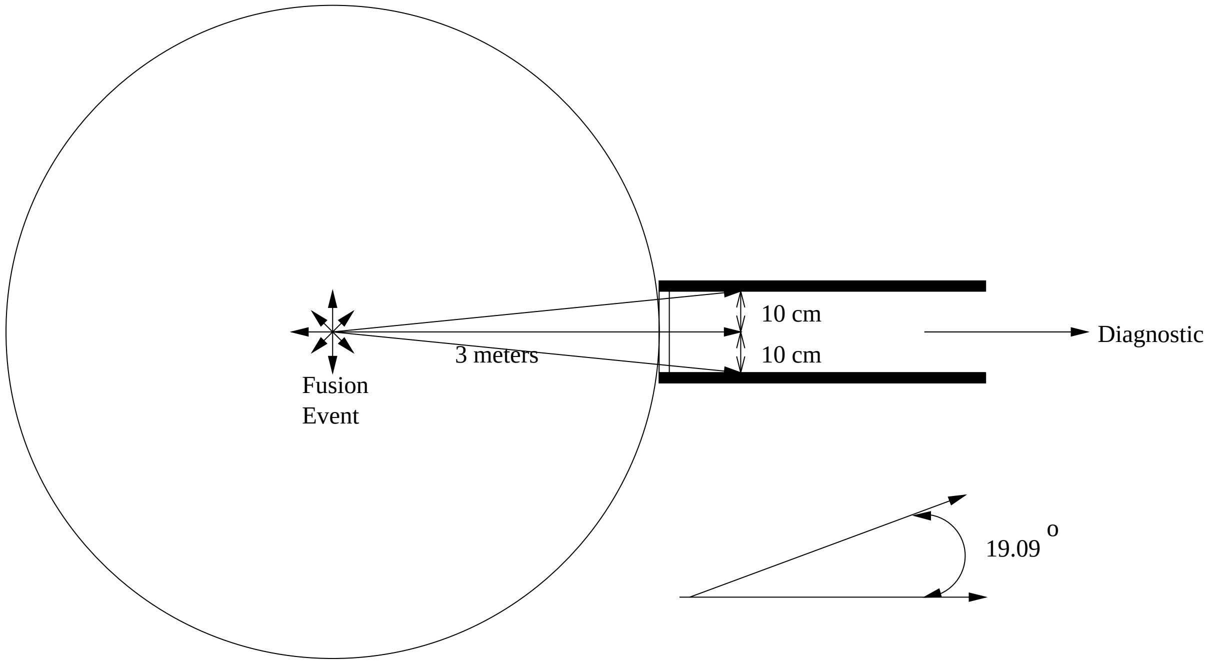

Figure 4.18. Neutron time of flight system – 2.

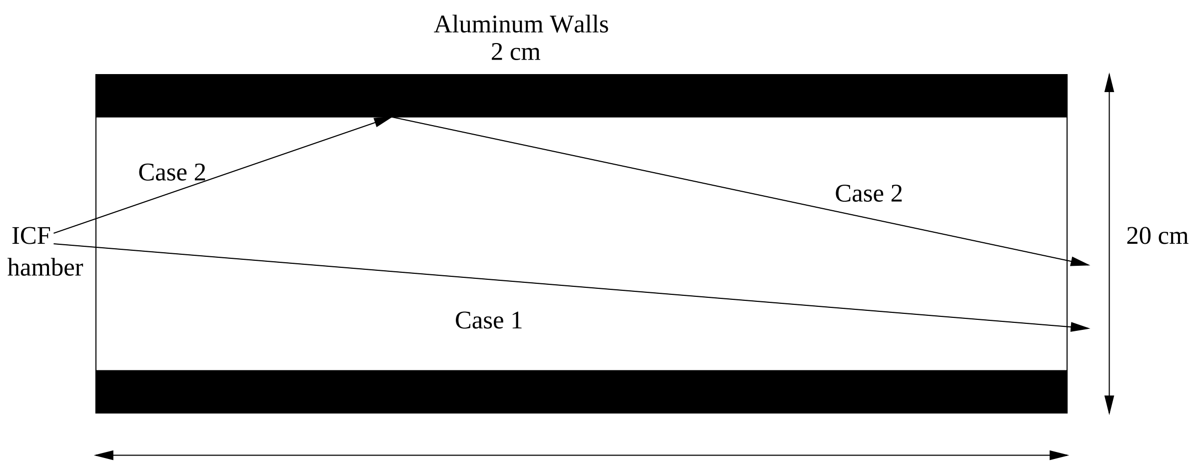

Figure 4.19. Neutron time of flight system – 3.

Twenty-four energy groups were used to simulate the continuous energy spectrum of incoming neutrons that will impact the first wall and enter the diagnostic tube. These energy groups are shown in Table 4.6. All energy groups, except the first for which the particles have a velocity that corresponds to an energy of 14.1 MeV, have a velocity that corresponds to $E_{Midpoint}$ for that group.

All the incoming neutrons are assumed to have initial angles between -19.0 and 19.0°. Time of flight calculations were then performed for each energy group and the two energy groups immediately below. Thus for the first calculation, the incoming source particles will have energies of 14.1 MeV

Table 4.6. Energy groups (MeV) for time of flight problem.

Group	E_{Top}	E_{low}	$E_{Midpoint}$
1	14.918	13.499	14.208
2	13.499	12.214	12.856
3	12.214	11.052	11.633
4	11.052	10.000	10.526
5	10.000	9.0484	9.5242
6	9.0484	8.1873	8.6187
7	8.1873	7.4082	7.7077
8	7.4082	6.7032	7.0557
9	6.7032	6.0653	6.3843
10	6.0653	5.4881	5.7767
11	5.4881	4.9659	5.2270
12	4.9659	4.4933	4.7296
13	4.4933	4.0657	4.2795
14	4.0657	3.6788	3.8722
15	3.6788	3.3287	3.5038
16	3.3287	3.0119	3.1703
17	3.0119	2.7253	2.8686
18	2.7253	2.4660	2.5956
19	2.4660	1.8268	2.1464
20	1.8268	1.3534	1.5901
21	1.3534	1.0026	1.1700
22	1.0026	0.74274	0.87267
23	0.74274	0.55023	0.64848
24	0.55023	0.40762	0.47892

and the code will then transport particles in this energy group and the resultant scattered particles from the second and the third energy group. Only two downscattered energy groups are needed because the energy of a neutron scattering at a 90° angle off aluminum results in the neutron retaining 96% of its initial energy. Thus, two energy groups will cover all neutrons that have two large scattering events. In any case, most of the scattered particles that end up at the diagnostic will be the result of small angle scattering events and thus possess nearly all of their original energy, but will travel a longer path length. The detector will tend to predict a spectrum slightly downshifted in energy from the spectrum that enters in the diagnostic tube.

Five hundred spatial nodes were used along the length of the time of flight tube, or one node every 4 cm. Ten nodes were placed in the radial direction, or one node every 2 cm. The geometry was simulated using 2D Cartesian coordinates. Ideally, the problem should be performed in cylindrical; however, as the method currently does not support cylindrical coordinates, Cartesian was used in substitution.

A source of uncollided neutrons was placed at the diagnostic entrance. The source has a pulse width of one *dt*, or the amount of time that it takes for particles to travel one *dx*. Downscattered neutrons are placed in the tube at the spatial and temporal position at which they are scattered from the higher

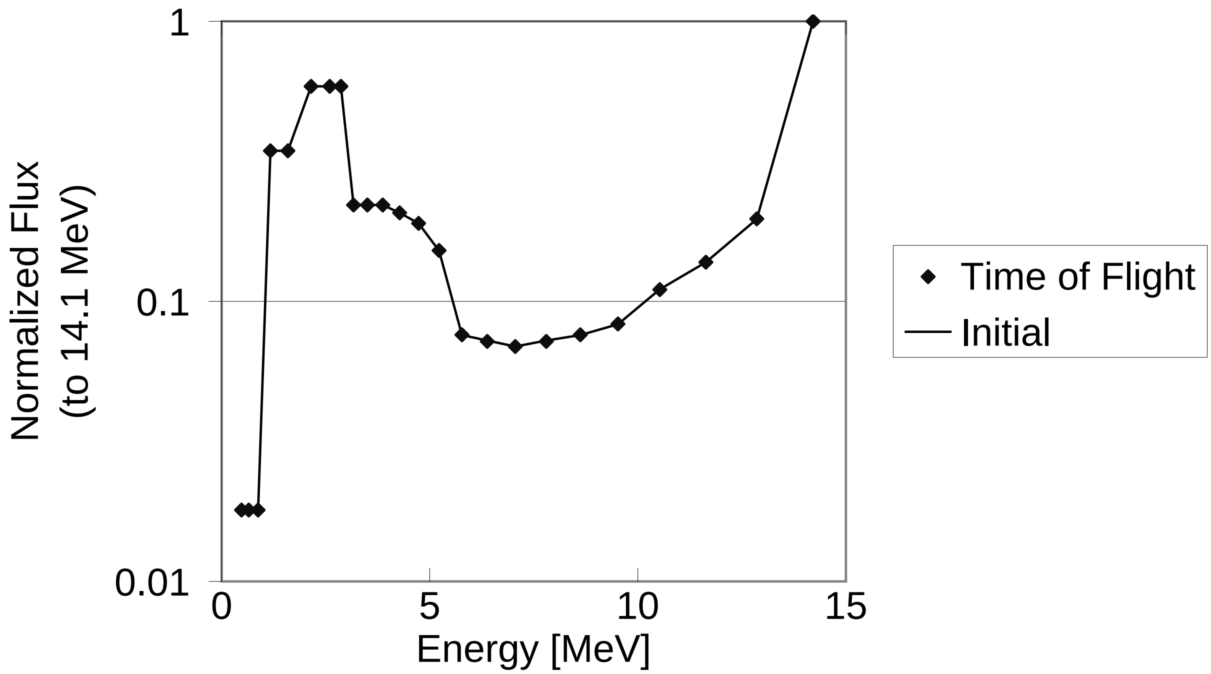

Figure 4.20. Spectrum at the diagnostic vs. initial spectrum.

energy group. The calculation was then allowed to proceed until there has been enough time for the particles in any given energy group to travel 30 meters, or 50% longer than the tube itself.

Figure 4.20 shows the neutron spectrum at the front of the tube (shown as the solid line) versus the spectrum that the diagnostic would see at the end of the 20 meter tube (data points) using the neutron energy groups provided in Table 4.6. There is very little difference between the two groups of data. This is because the energy groups are far apart. As a result, any difference caused by small angle scattering resulting in slightly longer path length would not show up in these widely spaced energy groups.

Figure 4.21 shows a more detailed view of the energy spectrum that the detector would "see" resulting from a pulse of 14.1 MeV neutrons entering the detector tube. The data is normalized to the flux value at the end of the tube for the "uncollided" direct flight 14.1 MeV neutrons. The figure shows that the vast majority of initial 14.1 MeV neutrons appear to the time of flight detector with energies above 13.9 MeV. This means, however, that if the detector can detect the differences of a fraction of a MeV, then there will be a slight drift towards lower energies.

The observations made for Figure 4.21 holds true for all the other energy groups. Figure 4.22, shows the observed energy spectrum for an initial particle flux of 1.5901 MeV (20th energy group). As in the previous case, a vast majority of particles lay within 95% of the energy of the initial particle flux. However, slight differences arise in the lower values of the graph. This is caused by the differences in the scattering cross section for the particular energy group. The higher the cross section, the more likely particles will be to scatter down the tube, once they interact with the aluminum tubing.

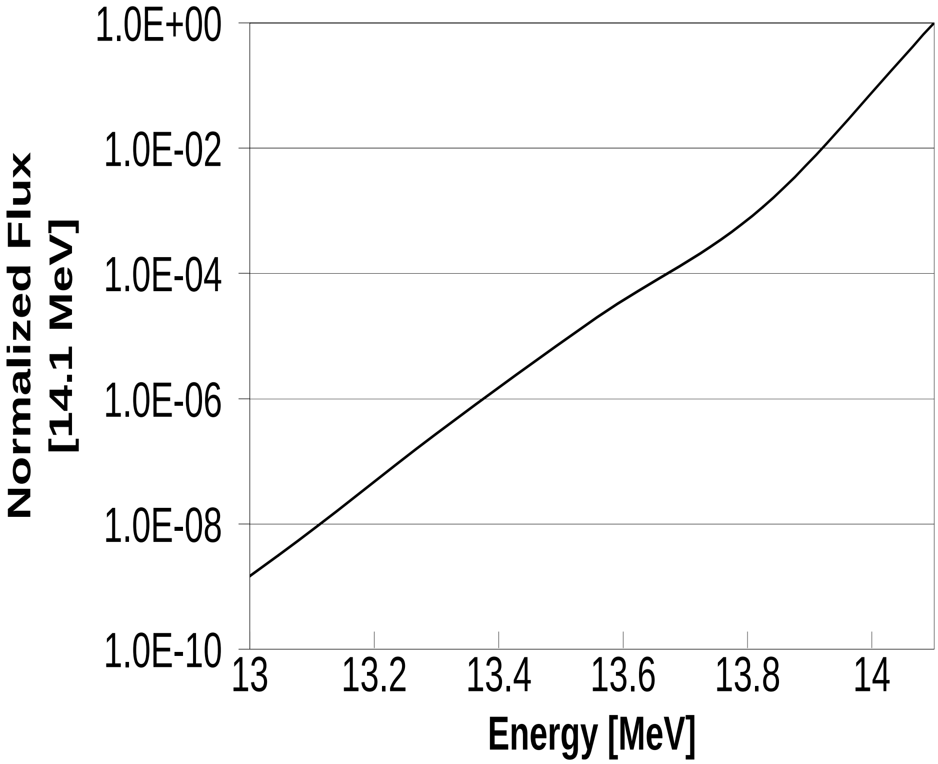

Figure 4.21. Spectrum seen by diagnostic for 14.1 MeV neutrons (energy group 1).

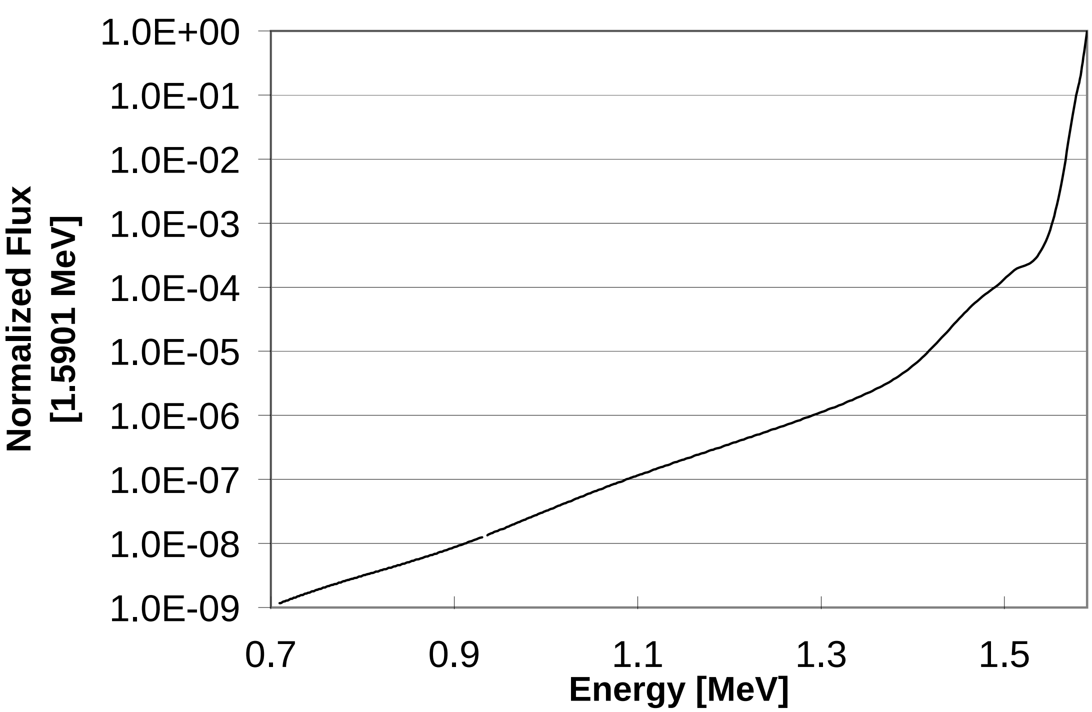

Figure 4.22. Spectrum seen by diagnostic for 1.5901 MeV neutrons (energy group 20).

References for Section 4

[1] J.J. Duderstadt and G.A. Moses, Inertial Confinement Fusion, John Wiley & Sons, New York, 125-130 (1982).

[2] "LASNEX: A Laser Fusion Simulations Code," UCRL-50021-80, Laser Program Annual Report, Lawrence Livermore National Laboratory (1980).

[3] J.E. Morel, E.W. Larsen, et al., "A Synthetic Acceleration Scheme for Radiative Diffusion Calculations," J. Quant. Spectrosc. Rad. Transfer, 34, 243 (1985).

[4] G.L. Olson, "Solution of the Radiation Diffusion Equation on an AMR Eulerian Mesh with Material Interfaces," LA-UR-95-4174, (1996).

[5] C.D. Levermore and G.C. Pomraning, "A Flux-Limited Diffusion Theory," The Astrophysical Journal, 248, 321 (1981).

[6] N.K. Winsor, "Velocity Space Methods for Fusion Reactor Plasmas," Nucl. Sci. and Engr., 64, 33 (1977).

[7] D.L. Henderson and C.W. Maynard, "Time-Dependent Single-Collision Kernels for Integral Transport Theory," Nucl. Sci. and Engr., 102, 172 (1989).

[8] K.R. Olson and D.L. Henderson, "Time-Dependent Neutral Particle Transport in Homogeneous Materials," Trans. Am. Nucl. Soc., 76, 211 (1997).

[9] K.R. Olson and D.L. Henderson, "Fuel Assembly Pulsing using Time-Dependent Integral Transport Methods," Trans. Am. Nucl. Soc., 77, 190 (1997).

[10] K.R. Olson and D.L. Henderson, "Time-Dependent Integral Transport in Homogeneous and Heterogeneous Media," to be published, Ann. Nucl. Engr.

[11] K.R. Olson and D.L. Henderson, "Time-Dependent Radiation Transport in Hohlraums Using Integral Transport Methods," Fusion Tech. 34, 848 (November 1998).

[12] K.R. Olson, "Neutral Particle Integral Transport in Inertial Confinement of Fusion Systems Using Time Dependent Integral Transport Methods," Ph.D. Thesis, University of Wisconsin-Madison, October 1999.

[13] J.D. Lindl, "Inertial Confinement Fusion," Springer-Verlag, New York, p. 11 (1998).

[14] J.D. Schnittman and R.S. Craxton, Phys. Plasmas 3, 3786 (1998).

[15] D.L. Henderson, "Time-Dependent Integral Transport Kernels, Leakage Rates and Collisions Rates for Plane and Spherical Geometries," Ph.D. Thesis, University of Wisconsin-Madison, p. 3 (1987).

5. Diagnostic Hole Closure Calculations for Z-Driven Static-Wall Hohlraum Experiments

An experimental campaign is in progress on the Z accelerator at Sandia National Laboratories (SNL) [1] that uses z-pinch generated x-rays directed into static-wall hohlraums to produce conditions expected to occur in various parts of the NIF x-ray pulse. By varying the size of the static-walled hohlraum, the radiation temperature can be adjusted to match various parts on the NIF pulse and ablator performance can be studied before the arrival of the full laser energy on NIF. In these experiments depicted in Figure 5.1, the radiation temperature is diagnosed from a bolometer measurement of the total radiation power leaving a diagnostics hole in the hohlraum. The total x-ray power is taken to be:

$$I_x = \sigma A T_r^4,$$

where A is the area of the diagnostics hole, and σ is the Stefan-Boltzmann constant. Since the object of the diagnostic is to obtain $T_r(t)$ and $I_x(t)$ is measured, one needs to know A(t), where t is time. We have performed 2-D computer simulations with the RAGE code of the radiation-driven hydrodynamic motion of the hohlraum that lead to an estimate of A(t). This then leads to an estimate of $T_r(t)$.

This procedure has been applied to shot Z442. A cylindrical hohlraum 4 mm in height and 4 mm in diameter (4 x 4) was irradiated with x-rays from a W wire-array z-pinch. A 1 mm radius diagnostics hole is placed on the side of the hohlraum. This hole is positioned so that the edge of the hole is only 0.15 mm from the top of the hohlraum. The behavior of the pinch [2,3] and the flow of radiation from the pinch into the hohlraum [4] have been studied computationally. These lead to predictions of $T_r(t)$. However, in the work presented here, $T_r(t)$ is estimated from the bolometer measurements, assuming a constant A. We plan to perform additional calculations for the calculated $T_r(t)$. In the calculation presented here, the two $T_r(t)$'s shown in Figure 5.2 have been tried. One has a peak of 146 eV, which was obtained from $I_x(t)$ by assuming a 1.7 mm diameter diagnostics hole and a 0.8 albedo for the hohlraum walls. The second curve peaks at 190 eV and is just proportionally scaled from the first curve.

The RAGE radiation-hydrodynamics computer code has been used to model the closure of the diagnostics hole on shot Z442 [5]. These calculations are performed on the open Blue Mountain ASCI computer and the open Cray computer at Los Alamos National Laboratory. RAGE is a 1-D, 2-D, or 3-D adaptive mesh refinement hydrodynamics code with 2-temperature (material and radiation) gray radiation diffusion. RAGE is jointly written and maintained by SAIC and Los Alamos National Laboratory. SESAME equation of state and opacity tables are used in these calculations. Here, the hohlraum is modeled in 2-D cylindrical geometry, with the axis of symmetry on the center of the hole. The top of the hohlraum is modeled as a 25 µm thick gold cylinder around the hole, 0.15 mm from the edge of the hole. The hole is 1 mm in radius. Radiation is sourced into the center of the hohlraum. Examples of the simulation results are shown in Figure 5.3 where contours of inverse mean-free-path are plotted at 2550 ns for the 146 eV peak $T_r(t)$. Here one sees a jet of high opacity gold blowing in from the corner between the side of the hohlraum in the top. This is the major effect in closing off the diagnostics hole. To determine the position of the edges of the hole, line integrals of

$$\int_{center}^{bolometer} \frac{1}{\lambda}\ dx$$

from the center of the hohlraum out through the diagnostic hole to the bolometer. The edge of the hole is defined at the point when the integral is 2/3.

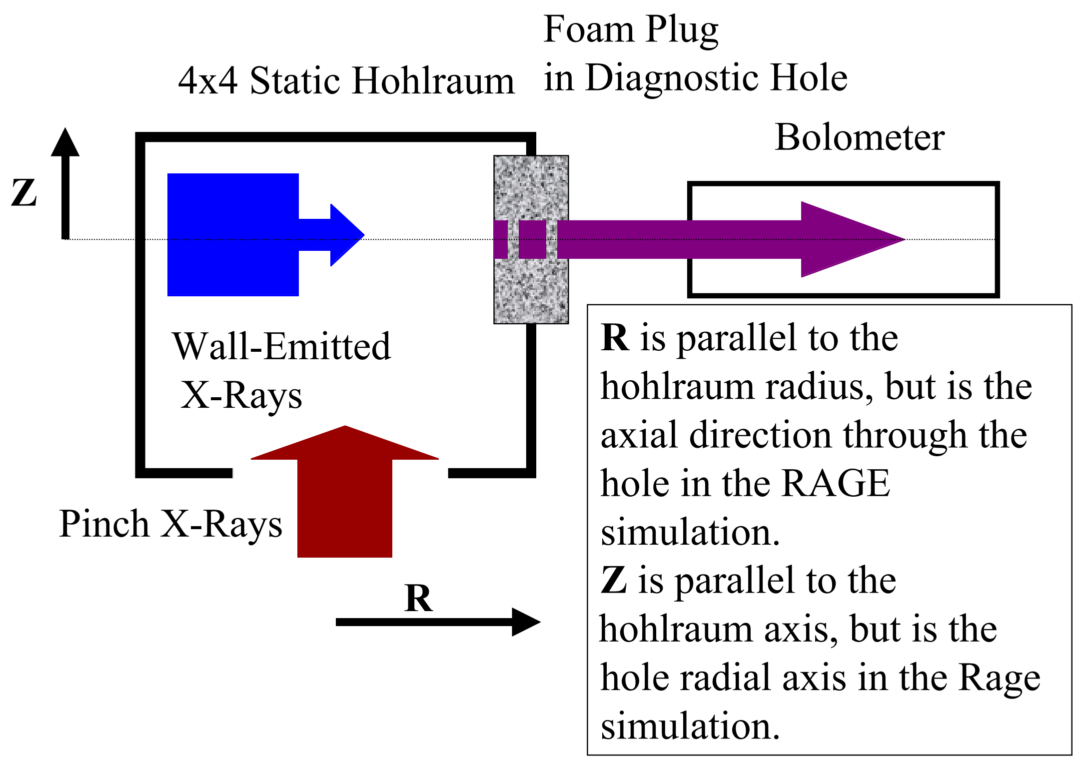

Figure 5.1. Schematic picture of static-wall hohlraum experiments.

The closing of the hole is actually asymmetric because the top is only on one side of the hole, so the jetting only obscures the hole from one side. The hole area A(t) is calculated from the post-processed RAGE results. The results are shown in Figure 5.4, where the hole areas are plotted versus time for the two-temperature histories. Calculational results are shown for a peak drive temperature of 146 eV with and without a 14 mg/cc plastic foam plug placed in the diagnostics hole and for a peak temperature of 190 eV without a foam plug. The results show that there is not much effect of the foam plug on the hole area. The predicted areas are then used to calculate the radiation emitted from the diagnostics hole,

$$I(t) = \sigma A(t) \alpha T_r^4(t)$$

where α is the albedo of the hohlraum wall. The calculated radiated power for 146 and 190 eV peak radiation temperatures are compared with the measured value in Figure 5.5. It is clear from this that the actual peak drive temperature is between 146 and 190 eV, probably about 160 eV. More calculations are needed using a peak temperature of 160 eV and using the calculated $T_r(t)$ [4].

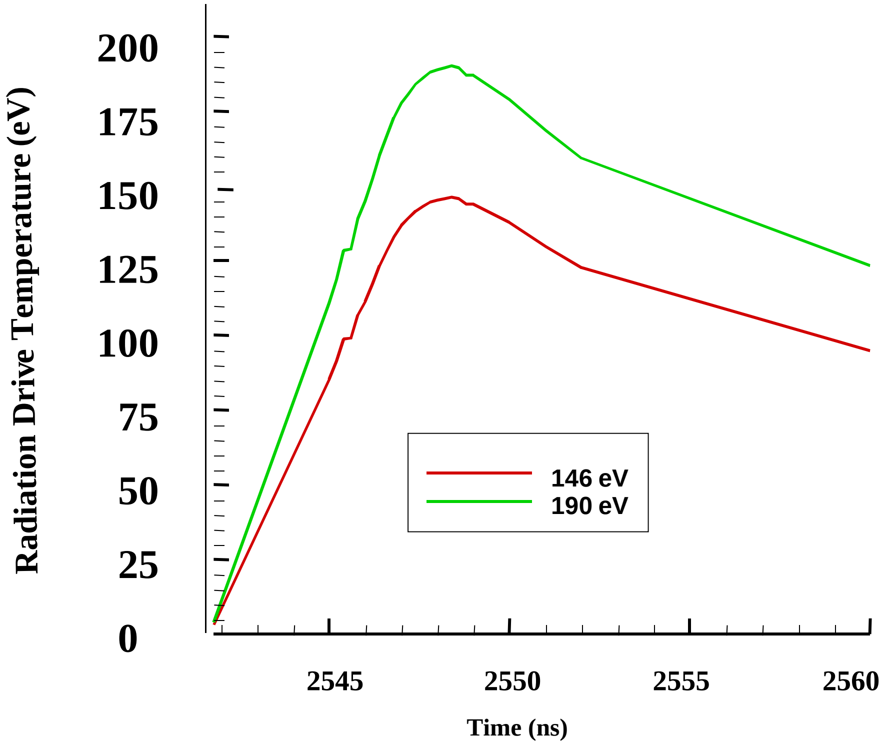

Figure 5.2. Input radiation temperature histories.

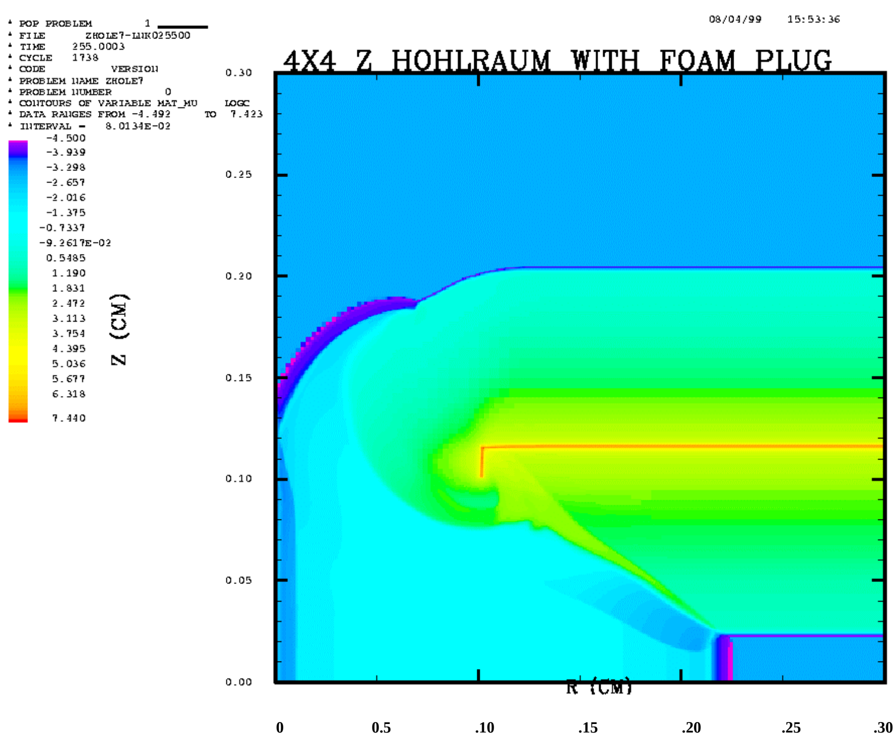

Figure 5.3. Inverse mean-free-path contours predicted by RAGE. The picture is at 2550 ns for a peak drive radiation temperature of 146 eV.

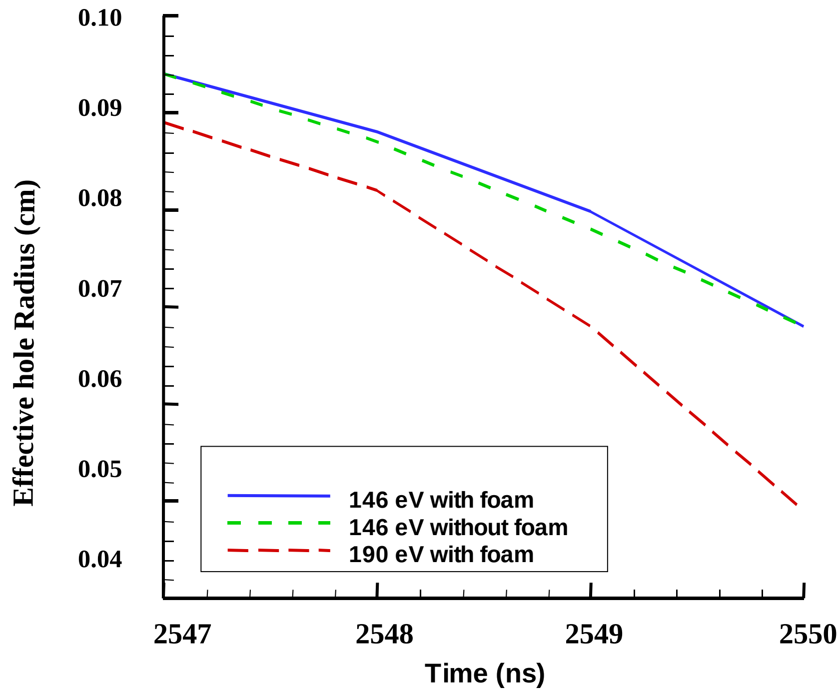

Figure 5.4. Calculated hole areas for $T_r(t)$ with a peak of 146 and 190 eV. For 146 eV, calculation with and without a foam plug in the diagnostics hole is presented.

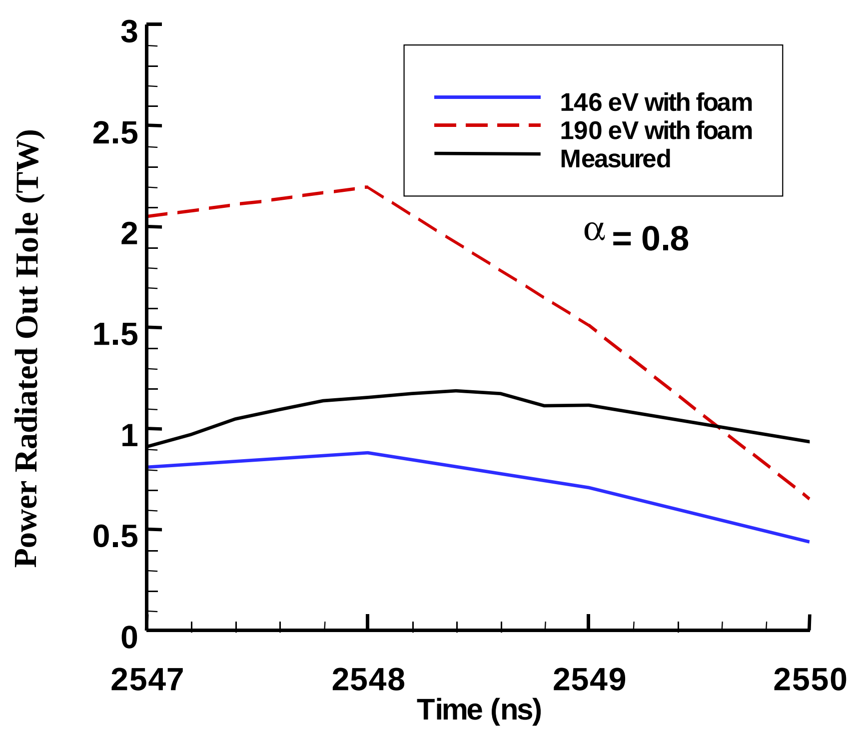

Figure 5.5. Calculated x-ray powers emitted from diagnostic hole versus time compared with bolometer measurement.

References for Section 5

[1] T.W.L. Sanford, et al., “Z-Pinch Generated X-rays in Static-Wall-Hohlraum Geometry Demonstrate Potential for Indirect Drive Studies,” 1st Intl. Conf. on Inertial Fusion Sciences and Applications (Bordeaux, France, September 12-17, 1999), Sandia National Laboratories Report SAND99-0662 (November 1999).

[2] D.L. Peterson, et al., “Instability Effects on Energy Flow in Z-Pinch Simulations," 41st Ann. Meeting of the APS Div. Plas. Phys. (Seattle, WA, November 1999), Bull. APS 44, 102 (1999).

[3] D.L. Peterson, et al., “Insights and Applications of Two-Dimensional Simulations of Z-pinch Experiments,” Phys. Plasmas 6, 2178 (1999).

[4] R.L. Bowers, Los Alamos National Laboratories, private communication (1999).

[5] R.R. Peterson, et al., “Diagnostic Hole Closure Calculations for Z-Pinch Driven Hohlraums on Z,” 41st Ann. Meeting of the APS Div. Plas. Phys. (Seattle, WA, November 1999), Bull. APS 44, 40 (1999).

6. Design and Analysis of Curved Insulating Rings for ZX

6.1 Introduction

In the past, one option proposed for the ZX target chamber was to use a stack of flat insulating rings for the walls of the chamber. A major challenge to this concept is the ability to withstand upsetting forces that would cause the stack to become unstable. We have proposed that a series of curved insulating rings be used to counter this effect. Figure 6.1 shows some of the details of the ZX target chamber. The curved interface between the insulating rings creates an additional lateral force to enhance the insulator stack stability against the residual pressure force. An external mechanism, a tie rod, and a tie nut as shown in the sketch create the stabilizing pressure on the insulator stack.

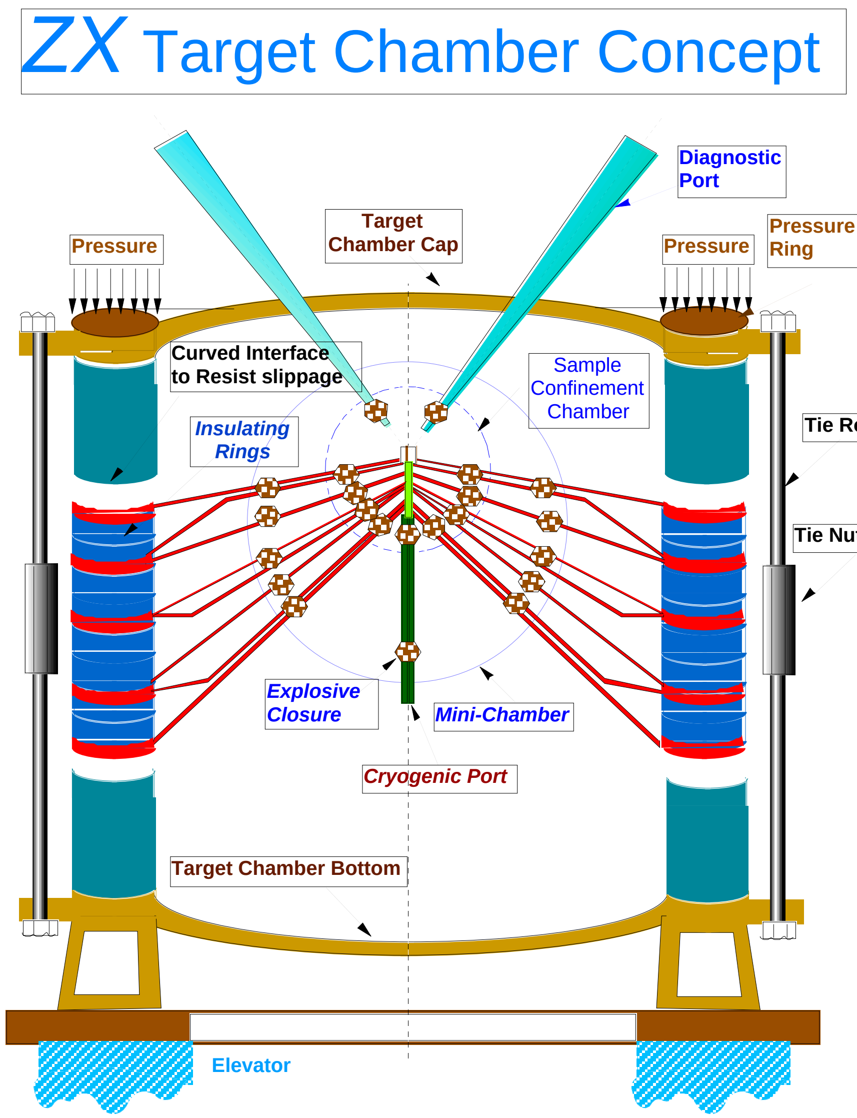

Figure 6.1. A sketch of the ZX target chamber showing the curved interface between insulating rings and some details of the internal parts.

6.2 Static frictional analysis

In the present design, the insulating rings have a flat interface and applying enough stabilizing pressure to hold the stack of rings together during operation creates the friction force between the rings. Increasing the target yield would require a higher stabilizing pressure. A higher stabilizing pressure may buckle or crush the insulator stack. In this section, we summarize the calculations that show how a set of curved interface rings would offer a solution to this problem and how the stack can be made stable under loads typical of a ZX target yield. Consider the sketch in Figure 6.2.

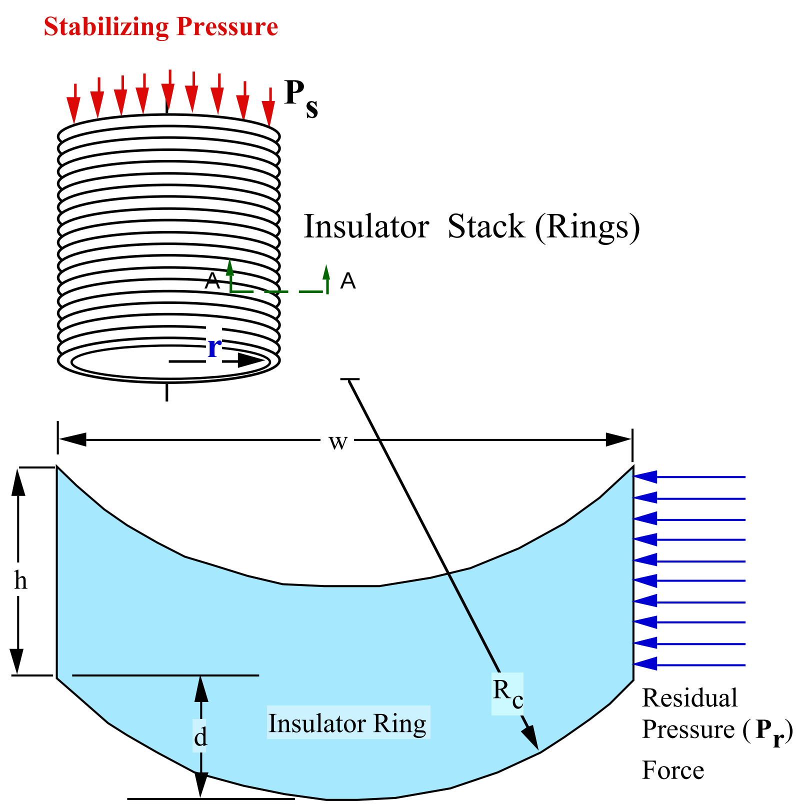

Figure 6.2. Forces and geometry of one insulating ring (section A-A).

The horizontal component due to (stabilizing pressure force + frictional force) =

$$2\,\mu\,(r + W/2)\,(2d\,P_s + 2\,\mu \mathbf{P_s}\,W) = 4\mu\;\mathbf{P_s}\,(r + W/2)(d + \mu\,W)$$

must equal (the residual pressure force ($2\,r\,h.\,\mathbf{P_r}$) x Factor of safety)

where:

$\mathbf{P_r}$	is the residual pressure
$\mathbf{P_s}$	is the stabilizing pressure
h	is the height of one insulating ring (0.06 m)
d	is the curvature depth
μ	is the static friction factor (0.25)
w	is the insulator stack width (0.15 m)
r	is the chamber radius (2.5 m)

$\mathbf{P_s}$ = (Factor of safety)[0.0291 $\mathbf{P_r}$ /(0.0375+d)]

for a flat interface, d = 0, and for a factor of safety of 1, $\mathbf{P_s}$ = 0.247 $\mathbf{P_r}$.

Now consider the three cases proposed for operation. The following is a list of parameters of the residual pressure versus the target yield.

Chamber/target parameters/Shots	Moderate	High	No Yield
Target Yield (MJ)	200	1008	0
Residual Pressure ($\mathbf{P_r}$) (MPa)	0.52	3.11	0.12
Insulator Stack Width (w) (cm)	15	15	15
Insulator Stack Depth (h) (cm)	6	6	6

The following analysis is for a moderate shot of a residual pressure $\mathbf{P_r}$ of 0.52 MPa:

assuming that d = 0 cm, with a factor of safety of 1, $\mathbf{P_s}$ would equal to 0.1286 MPa, and for d = 1 cm, with a factor of safety of 1, $\mathbf{P_s}$ equals to 0.101 MPa. Thus, the curvature depth of 1 cm of the interface would result in a reduction of 21.5% of $\mathbf{P_s}$ relative to the case of a flat interface. A parametric study is performed to show the effect of the depth of the curvature of the insulating ring interface on the stabilizing pressure. Figure 6.3 shows that if the curvature depth is about 3.5 cm the stabilizing pressure would be reduced by 50% from the case of a flat interface.

6.3 Static Transient Analysis of the Top Cover and the First Ring

The residual pressure loading is transient in nature. The following preliminary analysis is performed to investigate the transient nature of the residual pressure loading. The transient pressure loading on the inside walls of the cavity is calculated using the BUCKY code as shown in Figure 6.4. This pressure loading is used in the following transient analysis.

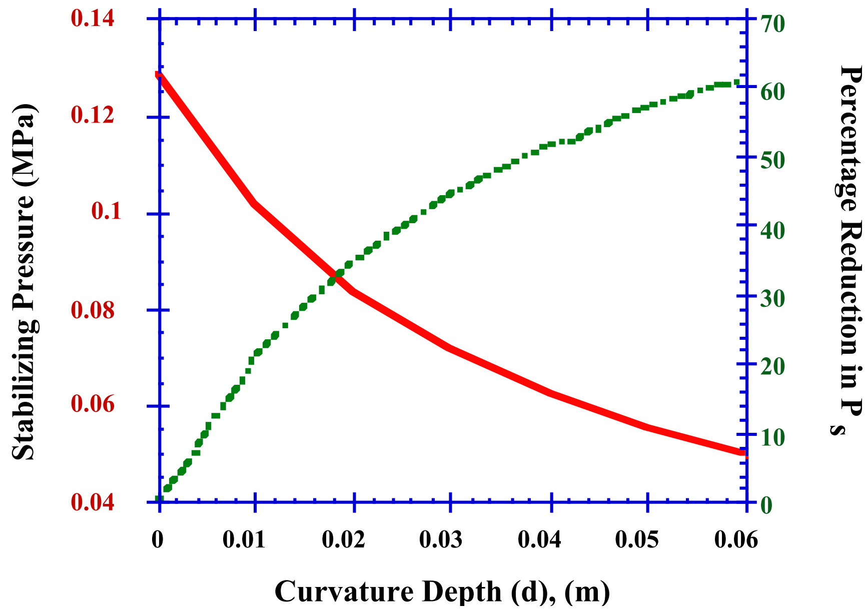

Figure 6.3. The effect of curvature of the insulating ring interface on the stabilizing pressure.

.

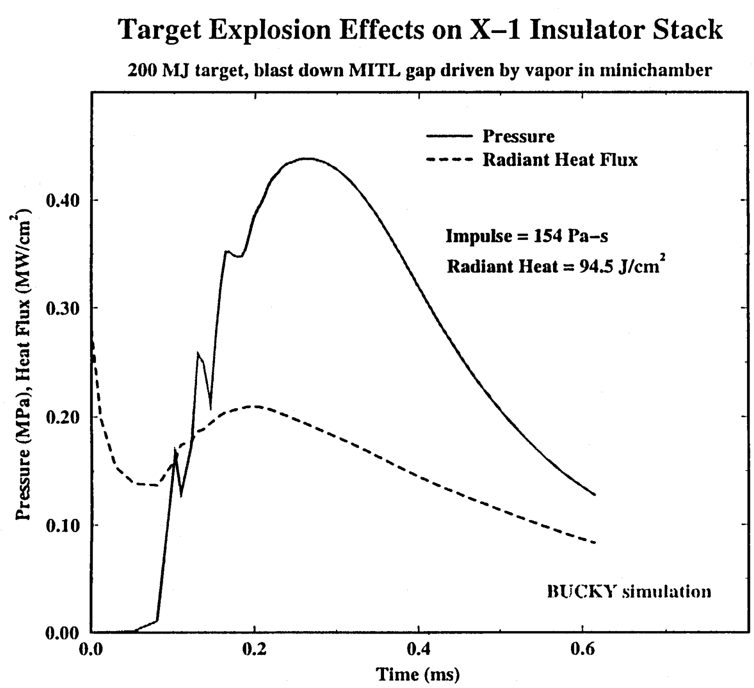

Figure 6.4. Pressure and heat on inner surface of X-1 insulator stack due to 200 MJ target explosion.

A Model to Study The Curved Interface Between Insulating Rings.

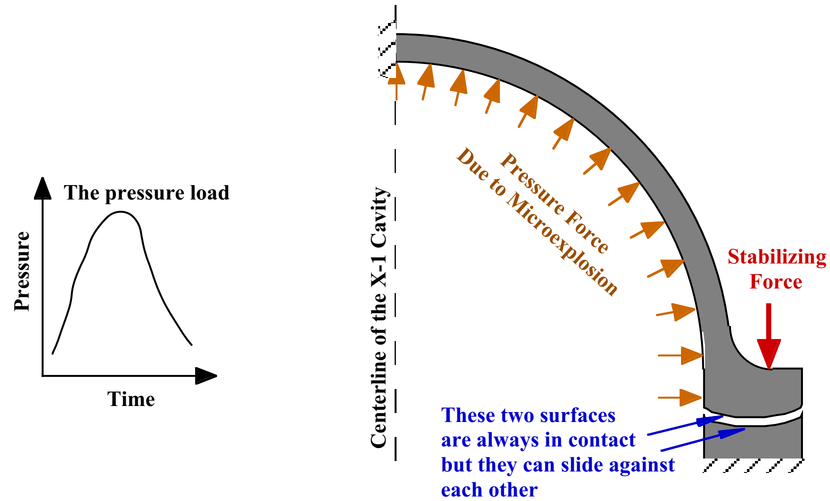

The Stabilizing Pressure for this Case = 1 MPa

Figure 6.5. A sketch of the model and the loading.

Figure 6.5 shows a sketch of the model and the loading on the top cover and the first ring of the X-1 insulator stack. An axisymmetric finite element model is furnished to analyze the transient performance of the top cover and the first ring of the X-1 insulator stack due to a 200 MJ target explosion, with a stabilizing pressure of 1 MPa. Figure 6.6 shows the finite element model of half of the top cover and the first ring. Contact elements have been used in the finite element analysis at the curved interface. These elements are not allowed to penetrate each other at the interface but can slide with friction. Gaps at the interface are permitted. Figure 6.7 shows an enlargement of the curved interface. Figures 6.8 and 6.9 show the displacement of the finite element model at different times. These preliminary results suggest that a gap could form at the interface due to the vertical force on the cover as well as a rotational slippage at the curved interface.

6.4 Future work

Analysis will be made to determine the optimum stabilizing pressure to prevent separation at the interface and without causing buckling or crushing of the insulator stack. Finding the optimum interface geometry with the aim of minimizing the stabilizing pressure will also be performed.

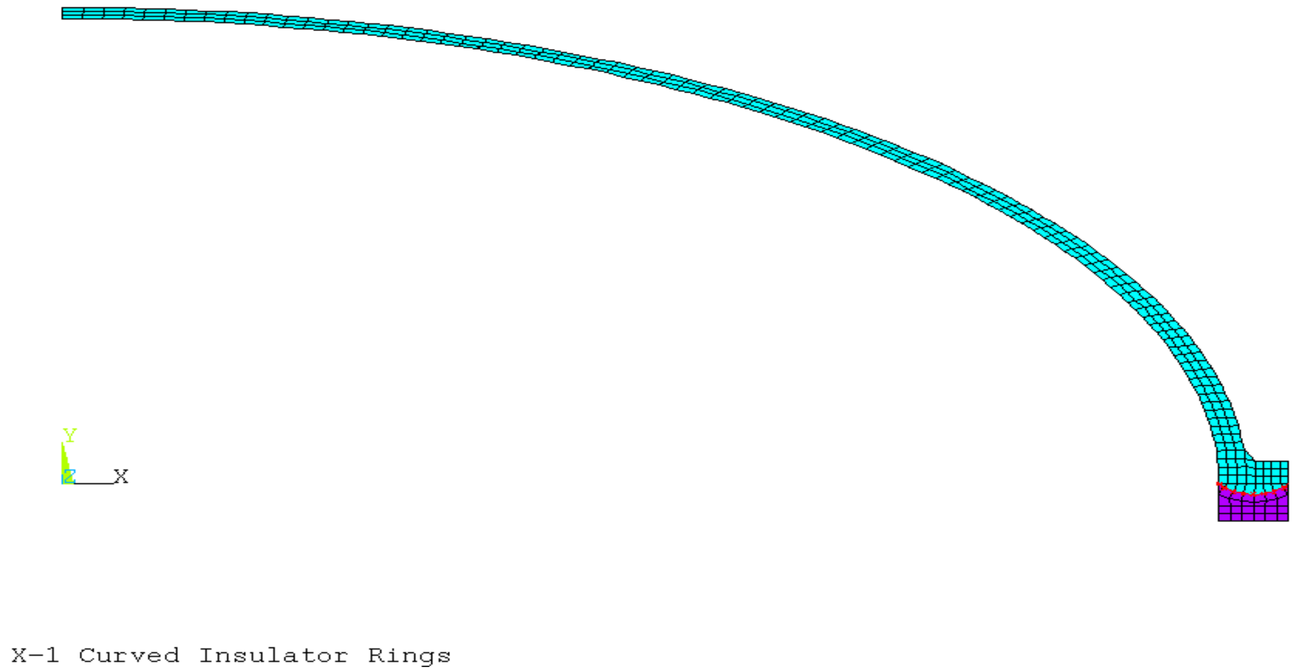

Figure 6.6. The finite element model of half of the top cover and the first ring.

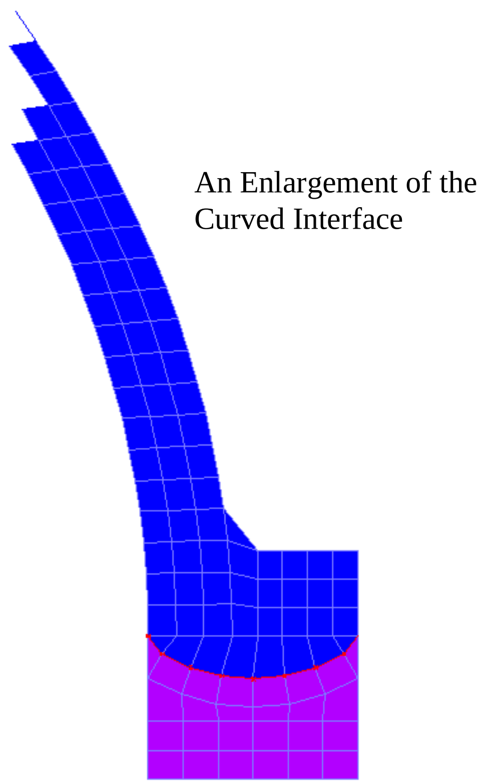

Figure 6.7. Finite element model of an enlargement of the curved interface.

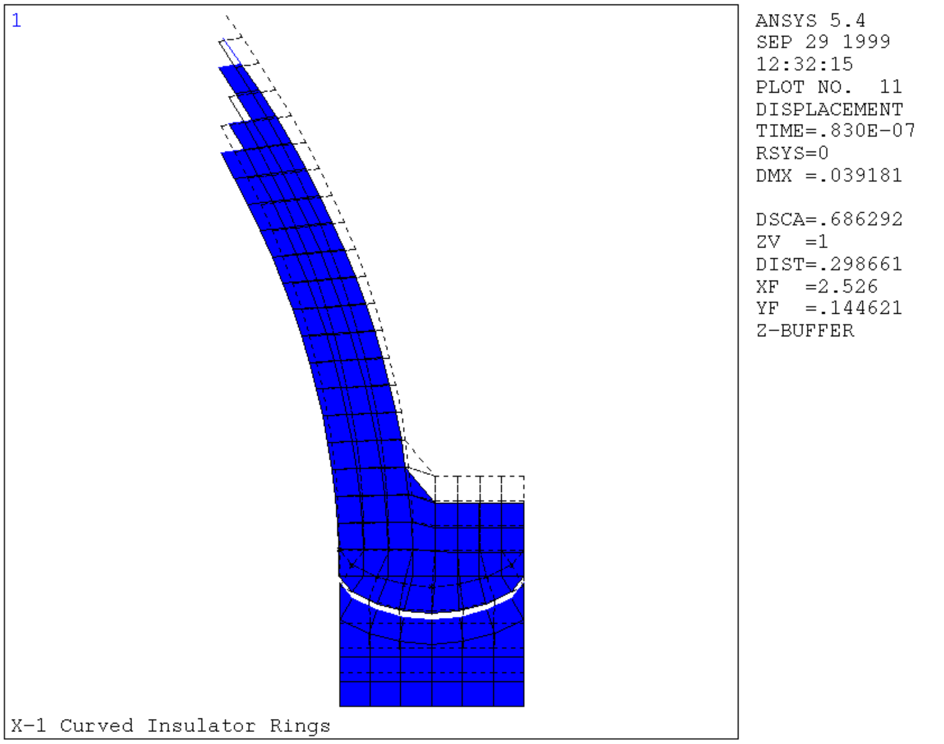

Figure 6.8. The displacement of the curved interface at time of 0.83×10^{-7} s.

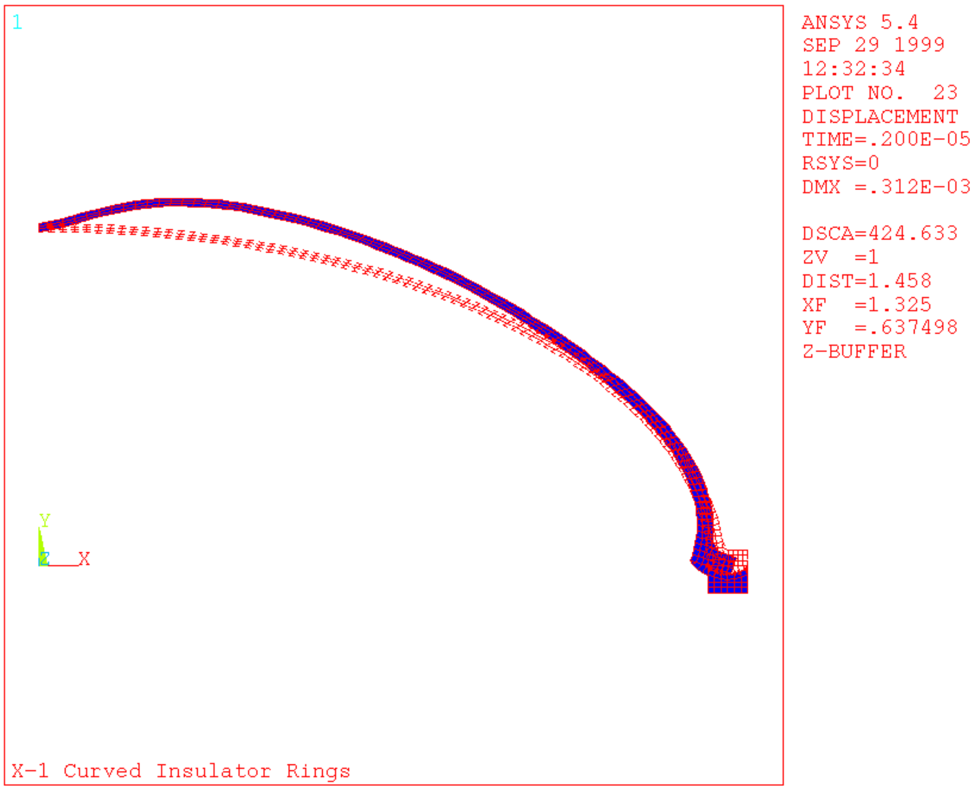

Figure 6.9. The displacement of the curved interface at time of 0.2×10^{-5} s .

7. Neutron Transport in Z Laser Backlighter

7.1 Calculation Method

A preliminary analysis was performed to examine the effect of neutron streaming through the proposed laser backlighter. Two-dimensional coupled neutron-gamma transport calculations are performed using the discrete ordinates neutron transport code DANTSYS [1] with FENDL-1 [2] cross section data. The analysis uses a P_3 approximation for the scattering cross sections and S_8 angular quadrature set. An inherent problem associated with multi-dimensional discrete ordinates calculations with localized sources is referred to as the "ray effect". It is related to the fact that the angular flux is given only in certain discrete directions. It is, therefore, not possible to exactly represent the component in the normal direction (μ= 1) along the laser beam penetration which can lead to underestimating neutron streaming. We have fully mitigated the ray effect by using the ray tracing first collision source method. In this method, the uncollided flux is determined analytically and the volumetrically distributed first collision source is used in the calculations.

The problem has been modeled in R-Z geometry with the target represented by an isotropic point source on the Z-axis. The source emits neutrons and gamma photons with energy spectra determined from target neutronics calculations for a generic single shell target [3]. The calculations are performed for two different types of shots. The first type is radiation shots with a pulsing schedule of 1 shot per day for the total of 240 shots per year. Only photoneutrons are produced during these shots. The photoneutrons are produced as a result of the interaction between the Bremsstrahlung radiation and the inner MITL materials. This analysis assumed a total Bremsstrahlung photon production of 5.62×10^{18} photon per shot. The photons are assumed to be monoenergetic with peak energy of 18 MeV. Using a conservative average iron (γ, n) cross section of 5 mb led to the production of 9.56×10^{15} neutrons per shot in the inner MITL. The neutrons had an average energy of 7 MeV. The second type of shots considered are moderate yield shots. These shots produce a yield of 200 MJ and have a pulsing schedule of 2 shots per month for the total of 24 shots per year. Figure 7.1 shows a schematic of the chamber and the laser backlighter. Figure 7.2 shows a schematic of the final focus lens mechanism detail. Since the design of the laser backlighter is still in its early stage [4], we had to make some assumptions about the materials used in its different components. In this analysis, we assumed that the mirror enclosure is made of the low activation Al-5083 alloy. The Al-5083 alloy was also used in the shock isolation mounts and the bellows. In addition, we assumed that the diagnostics cone is made of a tungsten alloy.

In order to model the final focus mechanism in two dimensions, we had to make several simplifications. The problem is assumed to be axisymmetric around the Z-axis. We modeled the cone shaped part as series of several small multi-steps and modeled the lens as a 5 cm thick layer of glass. We also had to homogenize some of the components. The rails were modeled as a homogenized mixture of 50% SS316 and 50% void. The mirror enclosure was modeled as a mixture of 50% Al-5083 and 50% void. The wall of the mirror enclosure is a 1 cm thick layer of Al-5083. Once the design of the laser backlighter is completed, a more detailed three-dimensional analysis would be needed in order to improve on the results obtained by this preliminary two-dimensional analysis.

7.2 Prompt Dose Rates

Figures 7.3 and 7.4 show the prompt dose during operation at the top of the final focus mirror assembly for the radiation and moderate yield shots, respectively. The dose values in the figures are given as a function of distance from the mirror enclosure center (R-direction). As shown in Figure 7.3, the prompt dose values at the top of the mirror enclosure are low during radiation shots. The dose values are dominated by contribution from photoneutrons streaming through the laser backlighter. On the other hand, as shown in Figure 7.4, the dose values during moderate yield shots are very high. Figures 7.5 and 7.6 show the prompt dose during operation at the side of the final focus mirror assembly for the radiation and moderate yield shots, respectively. The dose values in these figures are given as a function of distance from the tank surface (Z-direction). As shown in Figure 7.5, the prompt dose values at the side of the mirror enclosure remain low during radiation shots. Figure 7.6 shows that the dose values during moderate yield shots remain high. Due to the high prompt doses, access to the area surrounding the mirror enclosure should be restricted during moderate yield shots.

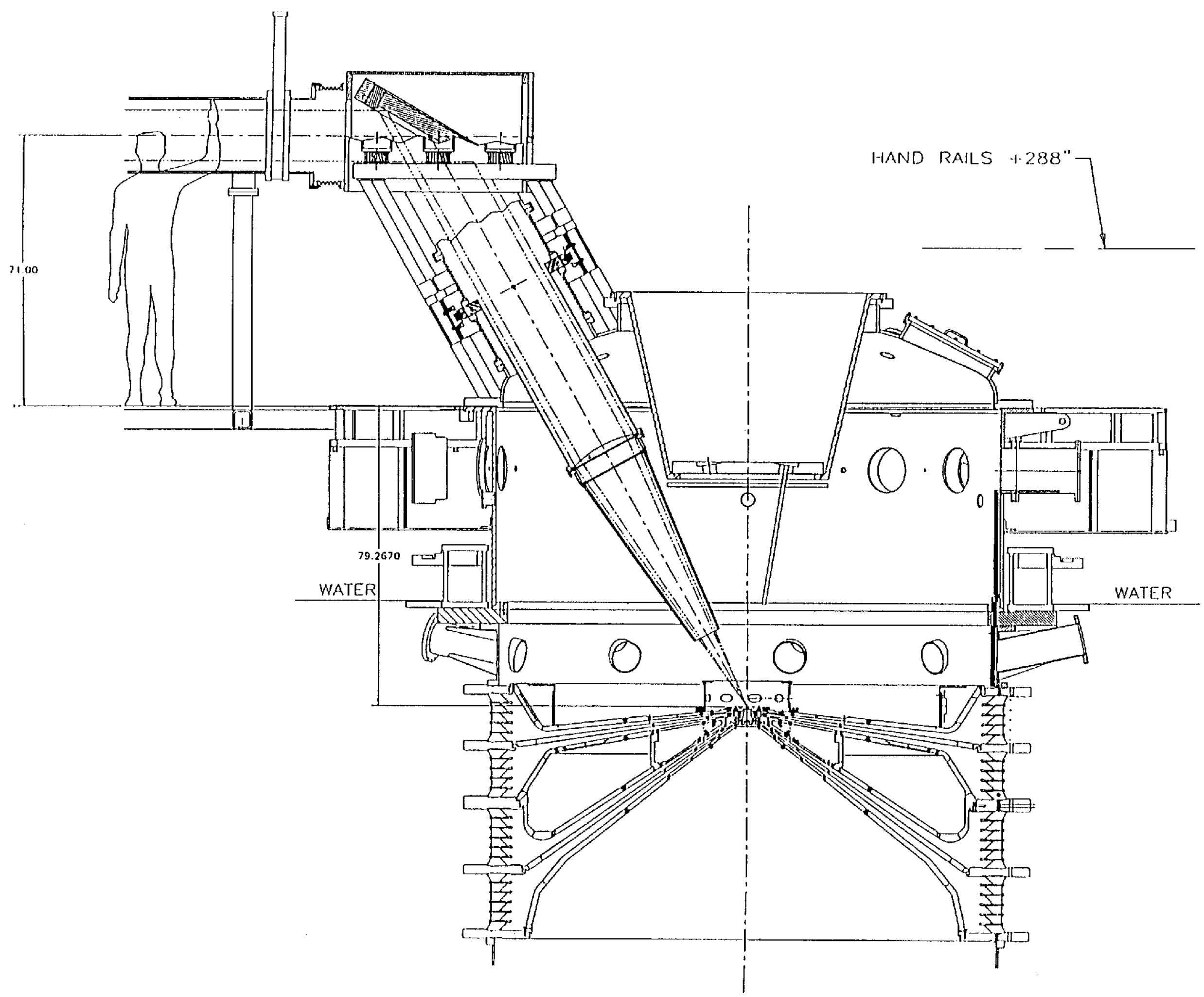

Figure 7.1. A schematic of the chamber and the laser backlighter.

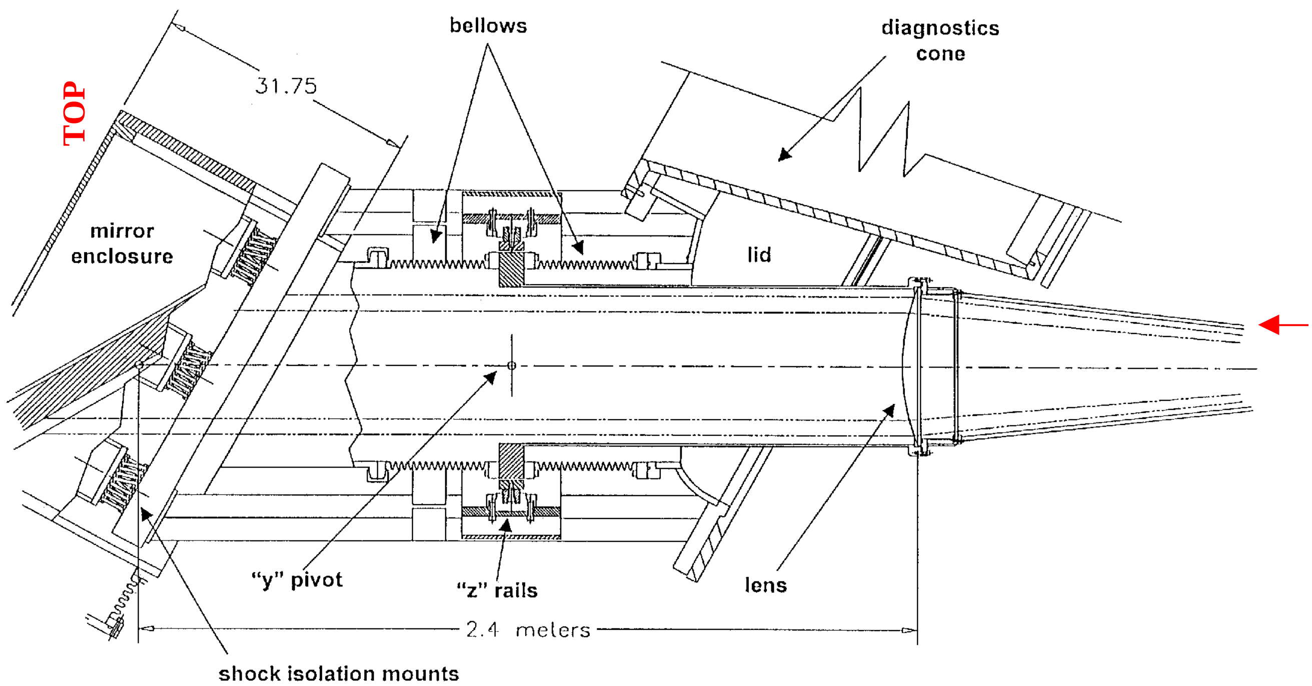

Figure 7.2. A schematic of the final focus lens mechanism detail.

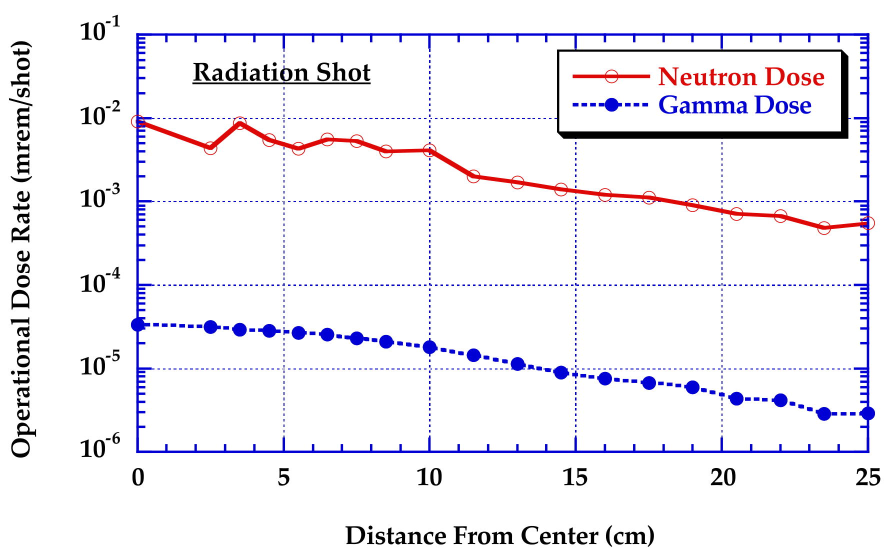

Figure 7.3. Dose rates during radiation shots at the top of the final focus mirror assembly.

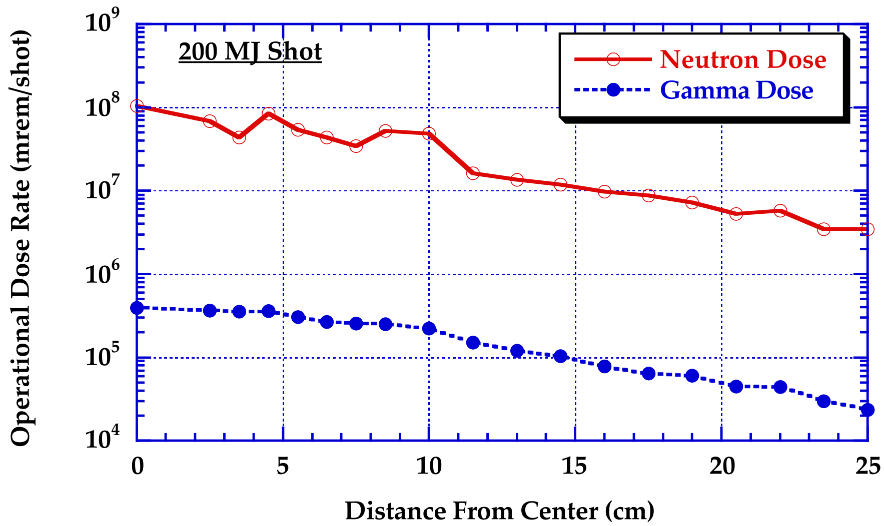

Figure 7.4. Dose rates during moderate yield shots at the top of the final focus mirror assembly.

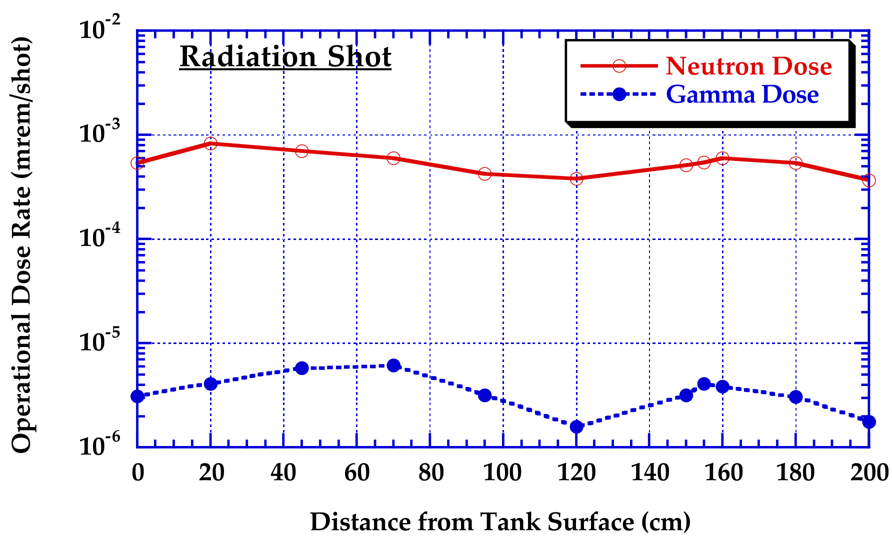

Figure 7.5. Dose rates during radiation shots at the side of the final focus mirror assembly.

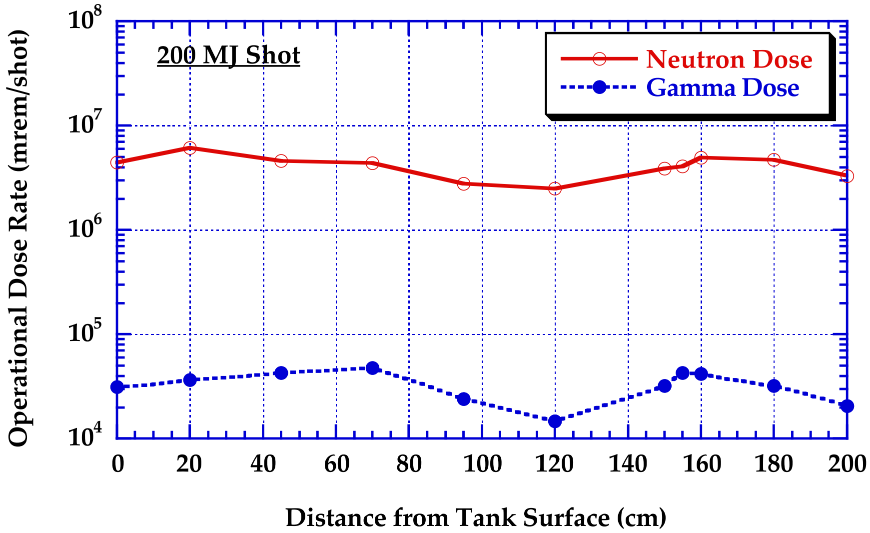

Figure 7.6. Dose rates during moderate yield shots at the side of the final focus mirror assembly.

7.3 Biological Dose Rates

The neutron flux obtained from the neutron transport calculations is used in the activation calculations. The calculations are performed using the computer code DKR-PULSAR [5] with the FENDL-2 [6] activation cross section library. The neutron transmutation data used is in a 46-group structure format. The decay gamma source data is in 21-group structure format. The calculations are performed assuming one year of operation. Using the DKR-PULSAR code allows for appropriate modeling of the pulse sequence in ICF chambers. In a previous analysis of the Laboratory Microfusion Facility [7], it was shown that assuming an equivalent steady state operation (where the flux level is reduced to conserve fluence) results in underestimating the dose rates at shutdown by several orders of magnitude. The underestimation becomes negligible within a week from shutdown. The large underestimation within a short period of time following shutdown is because the activity during this time is dominated by short-lived radionuclides. The activities of short-lived isotopes are usually sensitive to the operational schedule before shutdown due to its buildup during the on-time event with subsequent decay during the dwell time. On the other hand, the long-term activity is dominated by long-lived radionuclides whose activity is determined by the total neutron fluence regardless of the temporal variation of the flux level. The decay gamma source produced by the DKR-PULSAR code is used to calculate the biological dose rate after shots around the final focus mirror assembly. The adjoint dose field is then determined by performing a gamma adjoint calculation using the DANTSYS code with the flux-to-dose conversion factors representing the source at the point where the dose is calculated. The decay gamma source and the adjoint dose field are then combined to determine the biological dose rate at different times following shutdown.

Biological dose rates are calculated at the top and the side of the final focus mirror assembly for different times following shots. Figure 7.7 shows a comparison between the biological dose rates at the two locations following radiation shots. As shown in the figure, hands-on maintenance at the top of the assembly is possible within several minutes following radiation shots. In this analysis, the limits for hands-on maintenance were assumed to be 2.5 mrem/hr. Figure 7.8 shows a comparison between the biological dose rates at the same two locations following moderate yield shots. In this case, hands-on maintenance is possible around the side and top of the mirror assembly after a few days following shots. Faster access is possible by allowing higher limits of dose exposure, which is possible for maintenance workers exposed to fewer hours of radiation exposure per year.

The gamma decay of the activated Al-5083 alloy dominates the dose rates at all times following shutdown. The dose rates within the first few minutes following shots are dominated by the decay of ^{24m}Na ($T_{1/2}$= 20.2 ms) produced from the ^{27}Al (n,α) reaction. During the first few hours, the doses are dominated by ^{24}Na ($T_{1/2}$ = 14.96 hr) produced from ^{23}Na (n,γ), ^{24}Mg (n,p), and ^{27}Al (n,γ) reactions and ^{27}Mg ($T_{1/2}$ = 9.45 min) produced from ^{26}Mg (n,γ), ^{27}Al (n,p), and ^{30}Si (n,α) reactions. The dose rates during the first week continue to be dominated by the decay of ^{24}Na. ^{54}Mn ($T_{1/2}$ = 312.2 d) is the dominant nuclide in the period up to ten years following shots. At times beyond 10 years after shutdown, the dose rates are caused by the decay of the ^{26}Al ($T_{1/2}$ = 7.3 x 10^5 yr). ^{26}Al is produced via the ^{27}Al (n,2n) reaction.

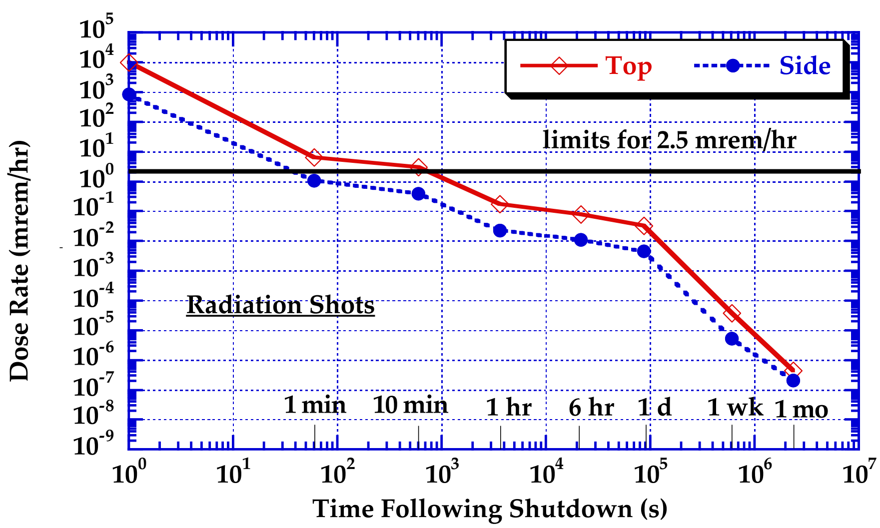

Figure 7.7. Biological dose rates following radiation shots.

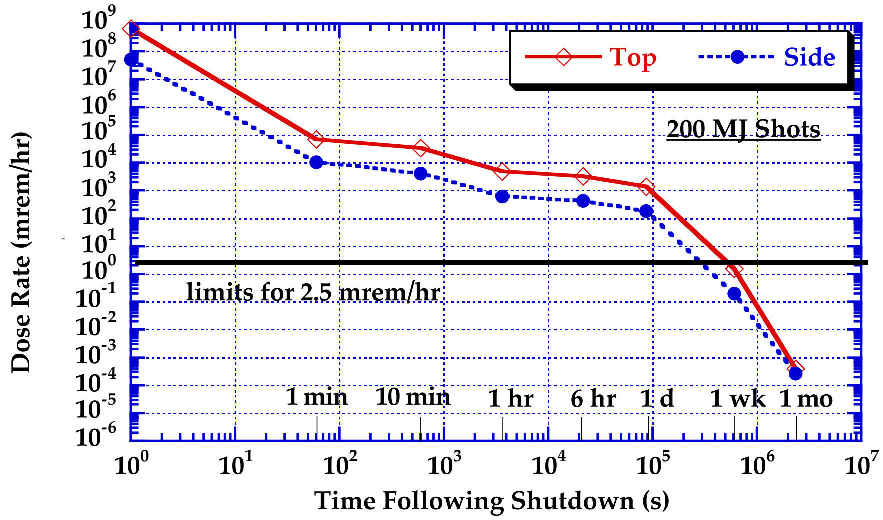

Figure 7.8. Biological dose rates following moderate yield shots.

References for Section 7

[1] R.E. Alcouffe et al., "DANTSYS 3.0, One-, Two-, and Three-Dimensional Multigroup Discrete Ordinates Transport Code System," RSICC Computer Code Collection CCC-547, Contributed by Los Alamos National Laboratory, August 1995.

[2] R. MacFarlane, "FENDL/MG-1.0, Library of Multigroup Cross Sections in GENDF and MATXS Format for Neutron-Photon Transport Calculations," Summary Documentation by A. Pashchenko, et al., Report IAEA-NDS-129, Rev. 3, International Atomic Energy Agency (Nov. 1995).

[3] D.L. Henderson, M.E. Sawan, and G.A. Moses, "Radiological Dose Calculations for the Diode Region of the Light Ion Fusion Target Development Facility," Fusion Technology, 13 (1988) pp. 594.

[4] Sally Gonzales, et al., "Final Focus Lens Assembly Conceptual Design Review," WBS 1.09.03.09, Sandia National Laboratory, March 30, 1999.

[5] J. Sisolak, et al., "DKR-PULSAR2.0: A Radioactivity Calculation Code that Includes Pulsed/Intermittent Operation," to be published.

[6] A. Pashchenko et al., "FENDL/A-2.0: Neutron Activation Cross-Section Data Library for Fusion Applications," Report INDC(NDS)-173, IAEA Nuclear Data Section, March 1997.

[7] H.Y. Khater and M.E. Sawan, "Dose Rate Calculations for a Light Ion Beam Fusion Laboratory Microfusion Facility," Proc. IEEE 13th Symposium on Fusion Engineering, Knoxville, TN (October 1989) 1412-1415.

8. Safety Issues in X-1

In this section, we present a brief review of some of the safety issues associated with the use of plutonium in X-1. Pure plutonium expands sharply with temperature. If plutonium is heated to 120°C, the volume increases by about 11%. In pure form, plutonium is a hard and brittle metal, like cast iron, but which spontaneously ignites in air to form PuO_2. PuO_2 is a stable ceramic material with an extremely low solubility in water or body fluids and with a high melting point (2390°C). As shown in Table 8.1, plutonium metal reaction with air is dependent on its metal form.

Table 8.1. Plutonium metal reaction with air.

Forms and Ambient Conditions	**Reactions**
Non-divided metal at room temperature (corrodes)	Relatively inert, slowly oxidizes
Divided metal at room temperature	Readily reacts to form plutonium dioxide
Particles over ~1 mm diameter	Spontaneously ignites at ~500°C
Finely divided particles under ~1 mm diameter	Spontaneously ignites at ~ 150°C [1]
Humid, elevated temperatures	Readily reacts to form Pu dioxide

Plutonium can reach human beings through ingestion, contamination of open wounds, and inhalation. Ingestion is not a significant hazard, because plutonium passing through the gastrointestinal tract is poorly absorbed and is expelled from the body before it can do harm. The main threat to humans comes from inhalation. While it is very difficult to create airborne dispersion of a heavy metal such as plutonium, certain forms, including the insoluble PuO_2, at a particle size less than 10 µm, are a hazard. If inhaled, much of the material is immediately exhaled or is expelled by mucous flow from the bronchial system into the gastrointestinal. Some, however, will be trapped and readily transferred, first to the blood or lymph system and later to other parts of the body, notably the liver and bones. It is here that the deposited plutonium alpha radiation may eventually cause cancer. According to ICRP 60, 0.05 fatal cancers are produced per ingested or inhaled Sv of plutonium. A fatal cancer is induced by the inhalation or the ingestion of 0.14 mg and 30 mg of plutonium, respectively.

The International Atomic Energy Agency (IAEA) set the following limits for occupational exposure:

- An effective dose of 20 mSv/yr averaged over five consecutive years.
- An effective dose of 50 mSv in any single year.
- An equivalent dose to the lens of the eye of 150 mSv/yr.
- An equivalent dose to the extremities (hands and feet), or skin of 500 mSv/yr.

In addition, the IAEA set the following limits for public exposure:

- An effective dose of 1 mSv in any single yr.
- In special circumstances, an effective dose of up to 5 mSv in any single year provided that the average dose over five consecutive years does not exceed 1 mSv/yr.
- An equivalent dose to the lens of the eye of 15 mSv/yr.
- An equivalent dose to the skin of 50 mSv/yr.

Table 8.2 shows values for the committed effective dose per unit intake via inhalation and ingestion for workers from various plutonium isotopes. Similar data are given in Tables 8.3 and 8.4, for members of the public for intake by ingestion and inhalation, respectively [2].

Table 8.2. Worker's committed effective dose per unit intake {e(g)[a]} via inhalation and ingestion (Sv/Bq) from various plutonium isotopes.

Nuclide	Half-life (a)	Inhalation				Ingestion	
		Type[b]	f_1[c]	$e(g)_{1\,\mu m}$[a, d]	$e(g)_{5\,\mu m}$[a, d]	f_1[c]	$e(g)$[a]
^{236}Pu	2.85	M	5.0×10^{-4}	1.8×10^{-5}	1.3×10^{-5}	5.0×10^{-4}	8.6×10^{-8}
		S	1.0×10^{-5}	9.6×10^{-6}	7.4×10^{-6}	1.0×10^{-5}	6.3×10^{-9}
						1.0×10^{-4}	2.1×10^{-8}
^{238}Pu	87.7	M	5.0×10^{-4}	4.3×10^{-5}	3.0×10^{-5}	5.0×10^{-4}	2.3×10^{-7}
		S	1.0×10^{-5}	1.5×10^{-5}	1.1×10^{-5}	1.0×10^{-5}	8.8×10^{-9}
						1.0×10^{-4}	4.9×10^{-8}
^{239}Pu	2.41×10^4	M	5.0×10^{-4}	4.7×10^{-5}	3.2×10^{-5}	5.0×10^{-4}	2.5×10^{-7}
		S	1.0×10^{-5}	1.5×10^{-5}	8.3×10^{-6}	1.0×10^{-5}	9.0×10^{-9}
						1.0×10^{-4}	5.3×10^{-8}
^{240}Pu	6.54×10^3	M	5.0×10^{-4}	4.7×10^{-5}	3.2×10^{-5}	5.0×10^{-4}	2.5×10^{-7}
		S	1.0×10^{-5}	1.5×10^{-5}	8.3×10^{-6}	1.0×10^{-5}	9.0×10^{-9}
						1.0×10^{-4}	5.3×10^{-8}
^{241}Pu	14.4	M	5.0×10^{-4}	8.5×10^{-7}	5.8×10^{-7}	5.0×10^{-4}	4.7×10^{-9}
		S	1.0×10^{-5}	1.6×10^{-7}	8.4×10^{-8}	1.0×10^{-5}	1.1×10^{-10}
						1.0×10^{-4}	9.6×10^{-10}
^{242}Pu	3.76×10^5	M	5.0×10^{-4}	4.4×10^{-5}	3.1×10^{-5}	5.0×10^{-4}	2.4×10^{-7}
		S	1.0×10^{-5}	1.4×10^{-5}	7.7×10^{-6}	1.0×10^{-5}	8.6×10^{-9}
						1.0×10^{-4}	5.0×10^{-8}
^{241}Am	432	M	5.0×10^{-4}	3.9×10^{-5}	2.7×10^{-5}	5.0×10^{-4}	2.0×10^{-7}

[a] The committed effective dose per unit intake {e(g)} is the sum of the doses to all organs and tissues, weighted by their sensitivities to radiation and integrated over a lifetime, from the intake of unit activity of a radionuclide.

[b] For inhalation of particulates, types M and S denote, respectively, moderate and slow clearance from the lung. For plutonium, insoluble oxides are S; all other compounds are M; for americium, all compounds are M.

[c] The gut transfer factor f_1 represents the portion of the intake transferred to body fluids in the gut. For inhalation the f_1 values are valid for the component of the intake cleared from the lung to the GI tract. For compounds of plutonium, the gut transfer factor f_1 is: 1×10^{-4} for nitrates, 1×10^{-5} for insoluble oxides, and is taken as 5.0×10^{-4} for all other compounds. For compounds of americium, the gut transfer factor f_1 is 5×10^{-4} for all compounds.

[d] The 1 and 5 μm subscripts of the committed effective dose per unit intake {e(g)} 'represent' the diameters of the particles.

Table 8.3. Committed effective dose per unit intake {e(g)[a]} via ingestion (Sv/Bq) for members of the public.

Nuclide	Half-life (a)	Age ≤ 1 a		f_1[b] for age >1 a	Age				
		f_1[b]	e(g)[a]		1–2 a e(g)[a]	2–7 a e(g)[a]	7–12 a e(g)[a]	12–17 a e(g)[a]	>17 a e(g)[a]
^{236}Pu	2.85	0.005	2.1×10^{-6}	5.0×10^{-4}	2.2×10^{-7}	1.4×10^{-7}	1.4×10^{-7}	8.5×10^{-8}	8.7×10^{-8}
^{238}Pu	87.7	0.005	4.0×10^{-6}	5.0×10^{-4}	4.0×10^{-7}	3.1×10^{-7}	2.4×10^{-7}	2.2×10^{-7}	2.3×10^{-7}
^{239}Pu	2.41×10^{4}	0.005	4.2×10^{-6}	5.0×10^{-4}	4.2×10^{-7}	3.3×10^{-7}	2.7×10^{-7}	2.4×10^{-7}	2.5×10^{-7}
^{240}Pu	6.54×10^{3}	0.005	4.2×10^{-6}	5.0×10^{-4}	4.2×10^{-7}	3.3×10^{-7}	2.7×10^{-7}	2.4×10^{-7}	2.5×10^{-7}
^{241}Pu	14.4	0.005	5.6×10^{-8}	5.0×10^{-4}	5.7×10^{-9}	5.5×10^{-9}	5.1×10^{-9}	4.8×10^{-9}	4.8×10^{-9}
^{242}Pu	3.76×10^{5}	0.005	4.0×10^{-6}	5.0×10^{-4}	4.0×10^{-7}	3.2×10^{-7}	2.6×10^{-7}	2.3×10^{-7}	2.4×10^{-7}
^{241}Am	432	0.005	3.7×10^{-6}	5.0×10^{-4}	3.7×10^{-7}	2.7×10^{-7}	2.2×10^{-7}	2.0×10^{-7}	2.0×10^{-7}

[a] The committed effective dose per unit intake {e(g)} is the sum of the doses to all organs and tissues, weighted by their sensitivities to radiation and integrated over a lifetime, from the intake of unit activity of a radionuclide.

[b] The gut transfer factor f_1 represents the portion of the intake transferred to body fluids in the gut.

Table 8.4. Committed effective dose per unit intake {e(g)[a]} via inhalation (Sv/Bq) for members of the public.

Nuclide	Half-life (a)	Type[b]	Age ≤ 1 a		f_b^1 for age >1 a	Age				
			f_1[c]	e(g)[a]		1–2 a e(g)[a]	2–7 a e(g)[a]	7–12 a e(g)[a]	12–17 a e(g)[a]	>17 a e(g)[a]
^{236}Pu	2.85	F	0.005	1.0×10^{-4}	5.0×10^{-4}	9.5×10^{-5}	6.1×10^{-5}	4.4×10^{-5}	3.7×10^{-5}	4.0×10^{-5}
		M	0.005	4.8×10^{-5}	5.0×10^{-4}	4.3×10^{-5}	2.9×10^{-5}	2.1×10^{-5}	1.9×10^{-5}	2.0×10^{-5}
		S	1.0×10^{-4}	3.6×10^{-5}	1.0×10^{-5}	3.1×10^{-5}	2.0×10^{-5}	1.4×10^{-5}	1.2×10^{-5}	1.0×10^{-5}
^{238}Pu	87.7	F	0.005	2.0×10^{-4}	5.0×10^{-4}	1.9×10^{-4}	1.4×10^{-4}	1.1×10^{-4}	1.0×10^{-4}	1.1×10^{-4}
		M	0.005	7.8×10^{-5}	5.0×10^{-4}	7.4×10^{-4}	5.6×10^{-5}	4.4×10^{-5}	4.3×10^{-5}	4.6×10^{-5}
		S	1.0×10^{-4}	4.5×10^{-5}	1.0×10^{-5}	4.0×10^{-5}	2.7×10^{-5}	1.9×10^{-5}	1.7×10^{-5}	1.6×10^{-5}
^{239}Pu	2.41×10^{4}	F	0.005	2.1×10^{-4}	5.0×10^{-4}	2.0×10^{-4}	1.5×10^{-4}	1.2×10^{-4}	1.1×10^{-4}	1.2×10^{-4}
		M	0.005	8.0×10^{-5}	5.0×10^{-4}	7.7×10^{-5}	6.0×10^{-5}	4.8×10^{-5}	4.7×10^{-5}	5.0×10^{-5}
		S	1.0×10^{-4}	4.3×10^{-5}	1.0×10^{-5}	3.9×10^{-5}	2.7×10^{-7}	1.9×10^{-5}	1.7×10^{-5}	1.6×10^{-5}
^{240}Pu	6.54×10^{3}	F	0.005	2.1×10^{-4}	5.0×10^{-4}	2.0×10^{-4}	1.5×10^{-4}	1.2×10^{-4}	1.1×10^{-4}	1.2×10^{-4}
		M	0.005	8.0×10^{-5}	5.0×10^{-4}	7.7×10^{-5}	6.0×10^{-5}	4.8×10^{-5}	4.7×10^{-5}	5.0×10^{-5}
		S	1.0×10^{-4}	4.3×10^{-5}	1.0×10^{-5}	3.9×10^{-5}	2.7×10^{-5}	1.9×10^{-5}	1.7×10^{-5}	1.6×10^{-5}
^{241}Pu	14.4	F	0.005	2.8×10^{-6}	5.0×10^{-4}	2.9×10^{-6}	2.6×10^{-6}	2.4×10^{-6}	2.2×10^{-6}	2.3×10^{-6}
		M	0.005	9.1×10^{-7}	5.0×10^{-4}	9.7×10^{-7}	9.2×10^{-7}	8.3×10^{-7}	8.6×10^{-7}	9.0×10^{-7}
		S	1.0 × 10–4	2.2 × 10–7	1.0 × 10–5	2.3 × 10–7	2.0 × 10–7	1.7 × 10–7	1.7 × 10–7	1.7 × 10–7
^{242}Pu	3.76×10^{5}	F	0.005	2.0×10^{-4}	5.0×10^{-4}	1.9×10^{-4}	1.4×10^{-4}	1.2×10^{-4}	1.1×10^{-4}	1.1×10^{-4}
		M	0.005	7.6×10^{-5}	5.0×10^{-4}	7.3×10^{-5}	5.7×10^{-5}	4.5×10^{-5}	4.5×10^{-5}	4.8×10^{-5}
		S	1.0×10^{-4}	4.0×10^{-5}	1.0×10^{-5}	3.6×10^{-5}	2.5×10^{-5}	1.7×10^{-5}	1.6×10^{-5}	1.5×10^{-5}
^{241}Am	432	F	0.005	1.8×10^{-4}	5.0×10^{-4}	1.8×10^{-4}	1.2×10^{-4}	1.0×10^{-4}	9.2×10^{-5}	9.6×10^{-5}
		M	0.005	7.3×10^{-5}	5.0×10^{-4}	6.9×10^{-5}	5.1×10^{-5}	4.0×10^{-5}	4.0×10^{-5}	4.2×10^{-5}
		S	0.005	4.6×10^{-5}	5.0×10^{-4}	4.0×10^{-5}	2.7×10^{-5}	1.9×10^{-5}	1.7×10^{-5}	1.6×10^{-5}

[a] The committed effective dose per unit intake {e(g)} is the sum of the doses to all organs and tissues, weighted by their sensitivities to radiation and integrated over a lifetime, from the intake of unit activity of a radionuclide.

[b] For inhalation of particulates, types F, M and S denote, respectively, fast, moderate and slow clearance from the lung. For plutonium, insoluble oxides are S; all other compounds are M; for americium, all compounds are M. When no specific information is available, the recommended default absorption type for particulate aerosols is M

[c] The gut transfer factor f_1 represents the portion of the intake transferred to body fluids in the gut. For inhalation, the f_1 values are valid for the component of the intake cleared from the lung to the GI tract. For compounds of plutonium, the gut transfer factor f_1 is: 1×10^{-4} for nitrates, 1×10^{-5} for insoluble oxides and is taken as 5.0×10^{-4} for all other compounds. For compounds of americium, the gut transfer factor f_1 is 5×10^{-4} for all compounds.

8.1 Containment

Plutonium containment is achieved by barriers (static containment) and airflow using ventilation systems to establish pressure gradients (dynamic containment). As shown in Figure 8.1, static containment is normally provided by three physical barriers between the plutonium and the environment. Primary containment is the barrier between the worker and plutonium. Workers are permitted within the zone between the primary and secondary barriers. Plutonium is permitted in this zone only if it is totally contained in a transfer or storage container. Tertiary containment includes the building and the associated systems and is complemented by the dynamic containment provided by the building ventilation system. Dynamic containment is based on a series of negative pressure differentials where the pressure is lowest in areas where plutonium is contained. If a leak occurs, the flow is from the low contamination area toward the high contamination area. Monitoring should be carried out continuously to detect any failure of containment.

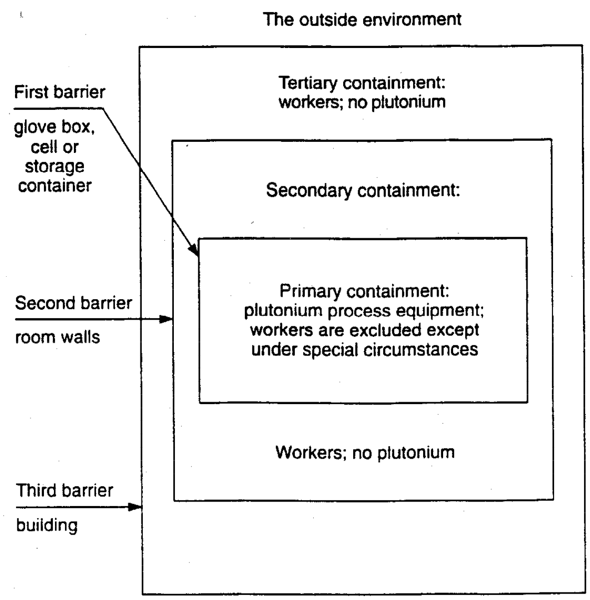

Figure 8.1. Schematic drawing of three-physical-barrier static containment.

To estimate the potential hazard associated with the accidental release of plutonium to the environment, off-site early doses are estimated using the Sv/Ci values calculated using the MACCS2 code [3]. Table 8.5 gives the number of mg of plutonium that would produce 0.01 Sv at the site boundary. The off-site dose calculations are performed using the following (worst release) conditions:

- Ground release
- Atmospheric stability class F
- 1 km site boundary
- 1 m/s wind speed.

Table 8.5. Number of mg of Pu producing 0.01 Sv at the site boundary.

Isotope	ED	LD
Pu-236 ($T_{1/2}$ = 2.87 y)	0.35	0.25
Pu-237 ($T_{1/2}$ = 45.2 d)	389	180
Pu-238 ($T_{1/2}$ = 87.7 y)	4.78	3.27
Pu-239 ($T_{1/2}$ = 2.41e4 y)	1224	821
Pu-240 ($T_{1/2}$ = 6.56e3 y)	334	224
Pu-241 ($T_{1/2}$ = 14.4 y)	43.9	28.2
Pu-242 ($T_{1/2}$ = 3.75e5 y)	20547	13698
Pu-243 ($T_{1/2}$ = 4.956 h)	79.1	67.7
Pu-244 ($T_{1/2}$ = 8e7 y)	4.64e6	3.06e6
Pu-245 ($T_{1/2}$ = 10.5 h)	5.3	5.26
Pu-246 ($T_{1/2}$ = 10.85 d)	6.37	5.02

ED Whole body early dose, the dose is from initial exposure; i.e., cloudshine during plume passage, 7 days of groundshine, and 50-year dose commitment from radioactivity inhaled during plume passage.

LD Whole body latent dose from release due to both initial exposure and chronic exposure (50 yr).

8.2 Release Limits

Ensuring safety is a crucial process in the ZX and X-1 designs. One of the design goals is to ensure that the impact of an accident on the workers as well as the surrounding population is sufficiently minimal. It is also important to show that no evacuation of the surrounding population is required in case of an off-site release of plutonium. Based on the limits shown in Tables 8.2, 8.3 and 8.4 the worker or public committed effective dose could be limited to less than 0.01 Sv if the permissible release of plutonium is limited to about 0.7 mg if the plutonium is inhaled. If the plutonium is ingested, then the permissible release of plutonium drops to about 4 µg. In case of an accident during which plutonium is dispersed by wind, the regulatory limits [4] require that the radiation dose at the 1 km site boundary be less than 0.01Sv for this condition to be met. The level of off-site dose is dependent on the wind and weather condition. Based on the values shown in Table 8.5, our preliminary calculation suggests that in order to meet the limit for no evacuation (early dose of 0.01 Sv), the maximum permissible release of plutonium must be limited to less than 900 mg. Of course, one would like to stay well below that value. In addition, dose to the workers would be the limiting factor for the amount of permissible release of plutonium. Calculation of required containment factors depends on the amount of plutonium to be used in any ZX or X-1 experiment.

References for Section 8

[1] U.S. Department of Energy, "Assessment of Plutonium Storage Safety Issues at DOE Facilities," DOE/DP-0123T (Washington, DC: U.S. DOE, Jan. 1994.

[2] Sutcliff, W.G., et al., "Perspective on the Dangers of Plutonium," Rep. UCRL-ID-118825, Lawrence Livermore National Laboratory, Livermore, CA (1995).

[3] M.L. Abbott, S.L. Harms, and A.S. Rood, "Dose Calculations for Accidental Airborne Releases of ITER Activation Products," Idaho National Engineering Laboratory Report, EGG-EEL-10994 (1993).

[4] Manual of Protective Action Guides and Protective Actions for Nuclear Incidents, EPA Report EPA-520/1-75-001, September 1975 (Revised June 1980).

9. Dust Transport Modeling

9.1 TEXAS-NC Past Work

Initial benchmark calculations for shock tubes have been performed using the noncondensable gas version of the TEXAS computer code to simulate flow aspects of pulsed power conditions. This work was reported at the Global '99 Conference on Future Nuclear Systems [1].

Results from simulations of experiments on the Wisconsin Shock Tube show that valves will need to be closed in times likely faster than 5 ms. The calculated results for pressure match those of the experiment very well. Differences can be attributed wall friction and to turbulence caused by the non-uniform cross-sectional area at the driver/driven interface and at the change from circular to square cross-section in the driven section.

A simulated 10 μm steel "dust" particle positioned just below the driver section of the Wisconsin Shock Tube at the beginning of the simulation follows the shock wave rather closely down the tube. It arrives near the end of the tube less than 2 ms behind the shock front and attains speeds exceeding 700 m/s. The particle then is buffeted by the shock wave reflection and is prevented from reaching the end of the tube.

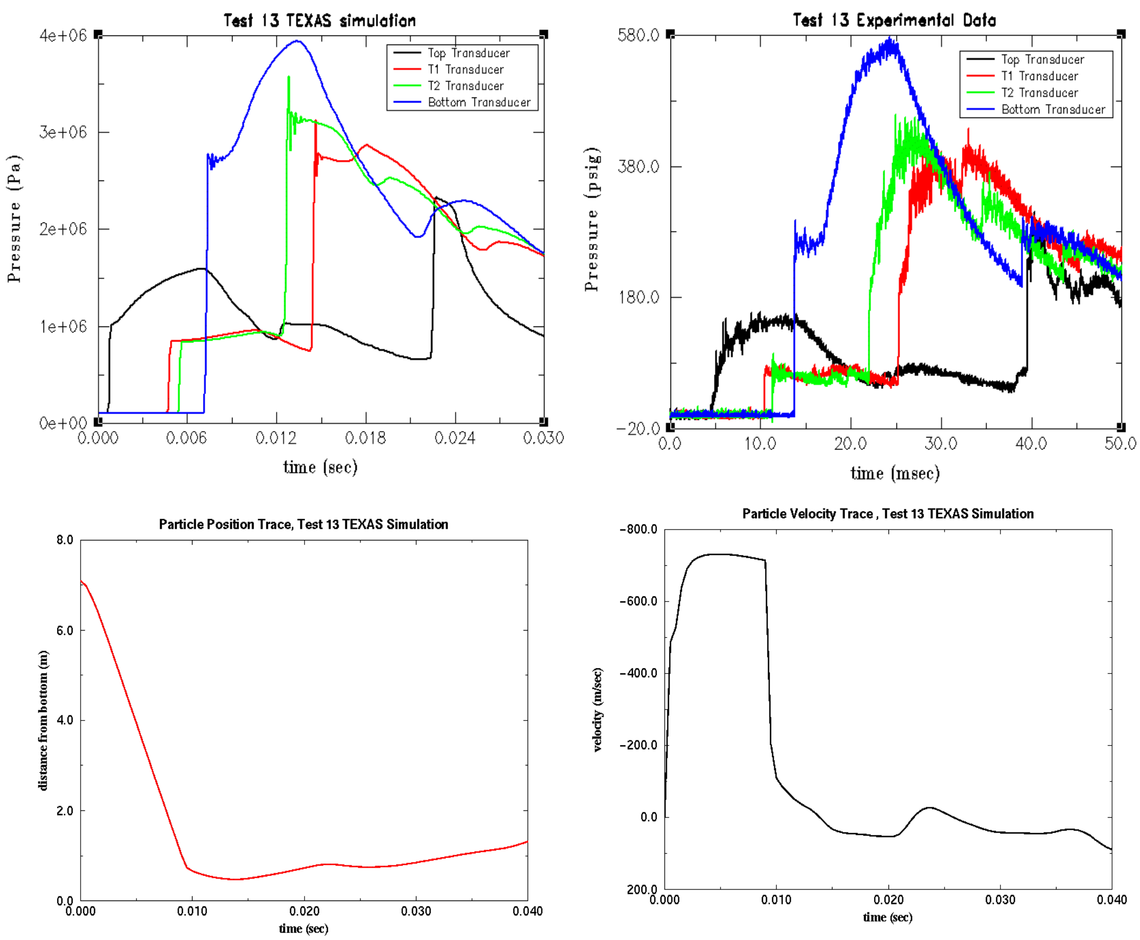

Figure 9.1. Pressure and simulated particle transport results for Test 13.

A similar calculation to Test 13 was made for a fictitious shock tube with a linear rate of increase in cross-sectional area over seven tube sections. The driver section was equivalent to Test 13. Results showed much lower pressure than for Test 13. This was expected because the expanding shock tube's volume is much larger than the Wisconsin Shock Tube, where cross-sectional area actually decreases twice. The shock speed was slower as a result of the expansion, taking over 8 ms to reach the bottom of the tube rather than 7 ms as observed in the simulation of Test 13. The simulated 10 μm steel "dust" particle also takes slightly longer to reach its maximum displacement from its initial position.

9.2 TEXAS-NC Recent Work

Because the speed of the shock wave in the TEXAS simulation of Test 13 was faster than observed in the experiment, a simulation was also run of the previous SIGMA experiments [2]. These experiments were chosen because the shock tube had constant cross-sectional area. The SIGMA experiments were also chosen because they had an air driver section and that could demonstrate the ability of TEXAS to handle shocks in different materials.

The case shown in Figure 9.2 is for air at 20.4 MPa driving water at atmospheric pressure. Initial shock arrival times at the two transducers match nearly perfectly with experiment, validating the code's predictions. The magnitude of the shock also compared well with experimental values.

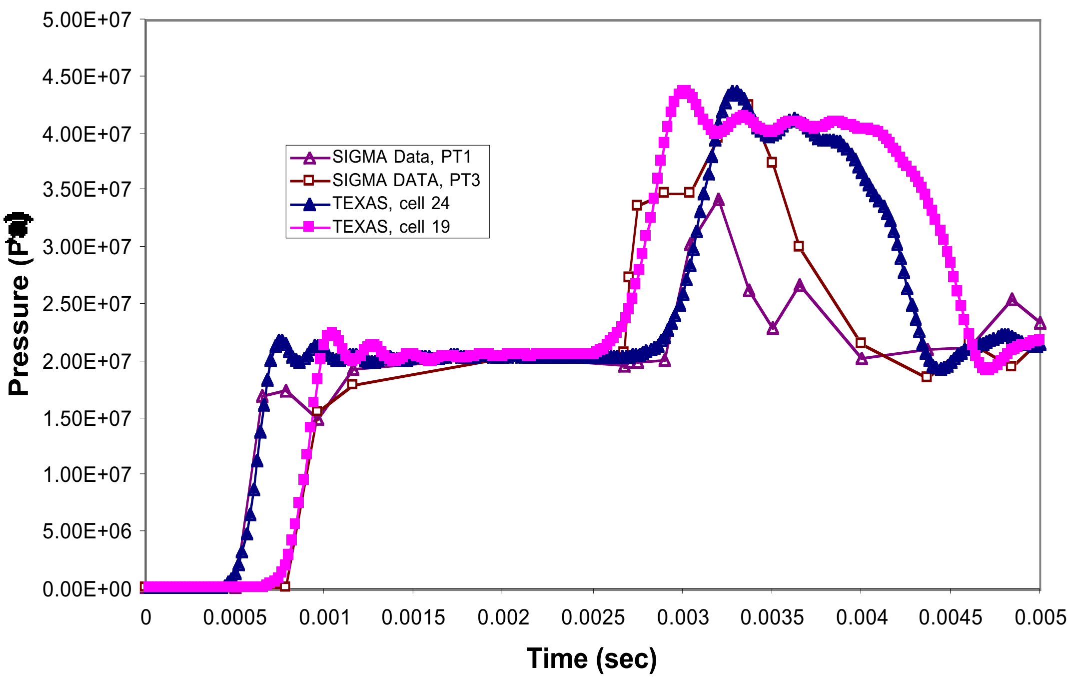

Figure 9.2. Pressure results for TEXAS simulation of SIGMA experiment with a constant cross section and all liquid driven section, 204 bar.

9.3 Hand Calculations for Z-pinch IFE Flow Regime

Dust and debris in Z-pinch IFE experiments are likely to be subject to inertially dominated flow, not Stokes flow. Some of this dust and debris may consist of melted structural material that will break up into tiny fragments from hydrodynamic forces exerted on them in the flow. This means that the particles will be accelerated significantly by the expanding fireball created from the fusion microexplosion. Figure 9.3 shows schematically what is expected to happen.

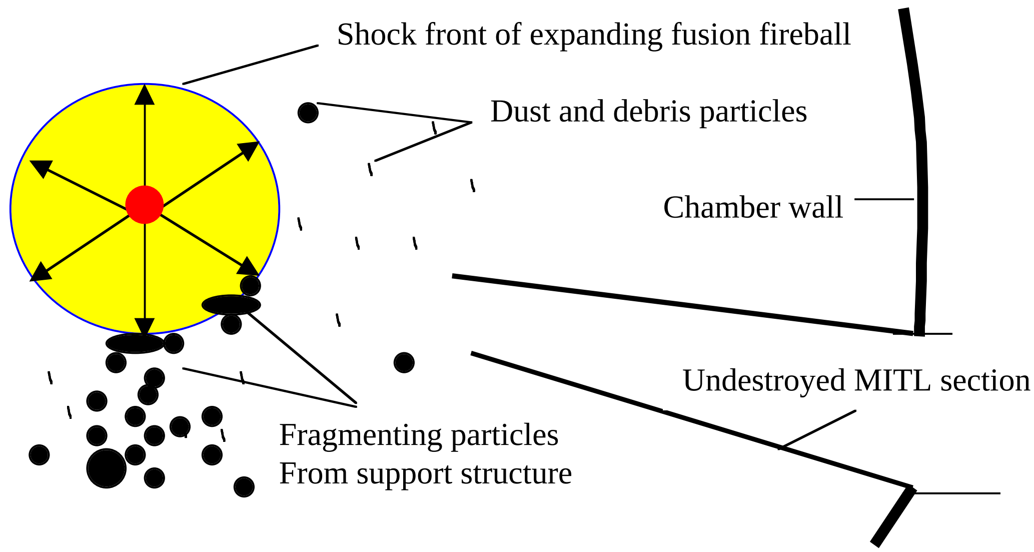

Figure 9.3. Dust and debris fragmenting from the fusion microexplosion.

Simple hand calculations for Reynolds (acceleration in flow) and Weber (fragmentation) numbers using data approximating fusion microexplosions were used to ensure that conditions expected in experiments on ZX or X-1 are appropriate for modeling with TEXAS-3D.

9.3.1 Reynolds Number for Dust and Debris Acceleration in the Flow

In inertially dominated flow regimes such as that created from a fusion microexplosion, particles of any significant size will travel well behind the leading edge of the expanding shock front. The following hand calculations show that particles in the size range of interest for high yield fusion Z-pinch experiments do not flow directly with the gases in the chamber.

Table 9.1 summarizes these calculations for particles of several different diameters with the following properties: gas density = 0.23 g/cm^3, gas velocity = 34,000 m/s, gas viscosity = 8 w^{-5} Ns/m, particle density = 7,800 kg/m^3, chamber radius = 3 m, particle surface tension = 0.5 N/m [3-5]. The data clearly show that particles 10 µm or greater in size are not subject to the Stokes flow regime. Also, the final velocity of all particles greater than 10 µm is significantly less than the gas velocity, and times of flight to the edge of the chamber lag significantly behind the shock front arrival time of 90 ms.

Table 9.1. Reynolds number and drag effects for varying particle diameters.

D_p (m)	Re	t_{flight} (s)	v_{final} (m/s)
10 microns	0.9775	0.0003092	19407
100 microns	9.775	0.002232	2688
1 millimeter	97.75	0.01408	426
1 centimeter	977.5	0.07303	82.15
10 centimeters	9775	0.231	25.98

9.3.2 Weber Number as it Pertains to Fragmentation of Liquid Debris

Much of the structure near the target in high-yield ICF experiments will be destroyed. Within some tens of centimeters everything may be vaporized, and material near the edges of remaining structure may be melted from X-ray heating. Therefore, when the shock front from the fusion microexplosion arrives, there is the potential for significant fragmentation. Modeling this process is important in predicting where the dust and debris mass ultimately resides.

Table 9.2 shows results for a parametric study of particle breakup time versus initial diameter using the same parameters as in Table 8.1. Note that the smallest particle size (10 μm) is below the critical Weber number for breakup. For large particles, the breakup times are very fast. However, as they break up the remaining portion of the particle will become smaller and smaller, thus breaking up slower and slower. The only data shown here are the times for the first fragment to form although thousands of fragments may eventually be created. For 100 μm particles, the breakup time is not much shorter than the travel time for the shock front.

Table 9.2. Weber number and particle breakup time for varying particle diameters.

D_p (m)	We	D_{frag} (m)	$t^{breakup}$ (s)
10 μm	5.318	N/A	N/A
100 μm	53.18	2.2257E-5	2.284E-7
1 mm	531.8	2.2257E-5	1.867E-9
1 cm	5318	2.2257E-5	7.118E-12
10 cm	53176	2.2257E-5	5.314E-13

9.4. TEXAS-3D Recent Work

A 3D version of TEXAS is currently under development. This is important for the application of the code in IFE experiments because machines on which these experiments are performed have complex geometries. The present status of the TEXAS-3D code development is incomplete. The continuous Eulerian fluid fields are operational, and the heat transfer package is in the process of testing. All of the subroutines have been modified from the one-dimensional version of the code, and their application in three-dimensions is still being tested. Parallel work to complete the code is under way, including implementation of the heat and mass transfer package for the Eulerian phases, introduction of Lagrangian particles, and development of a general equation of state.

Several recent general improvements have been made to the code. First, all of the subroutines for the Eulerian framework of TEXAS-3D have been updated to FORTRAN-90 and the code has been adapted to run on a PC platform. Second, comments have been added to many subroutines in order to facilitate development. Third, input has been removed from internal subroutines to an external file. Fourth and finally, an update procedure has been developed to ensure that new versions are consistent and multiple code developers can work together effectively. This procedure has been used successfully through four versions, and a fifth version is imminent.

9.4.1 TEXAS-3D Sample Problems

Three sample problems demonstrating the capability of the two Eulerian phases of the code have been developed. These sample problems are calculated with each new version of the code to ensure that results are consistent between versions.

9.4.1.1 Driven Cavity

In this problem, an initially still 1 m^3 box containing a uniform fluid has its top panel suddenly pulled at a constant velocity. This is like having a pan of water full to the brim and then continuously pulling a sheet of plastic wrap over its top. The movement of the top panel of the box induces a swirling motion in the fluid. Eventually, a steady state condition is achieved and the calculation is stopped. The TEXAS-3D velocity field and pressure distribution results have been compared to an equivalent calculation using FLUENT. Results generally matched within 10%. Figure 9.4 shows the velocity field at an early time step and near steady state conditions.

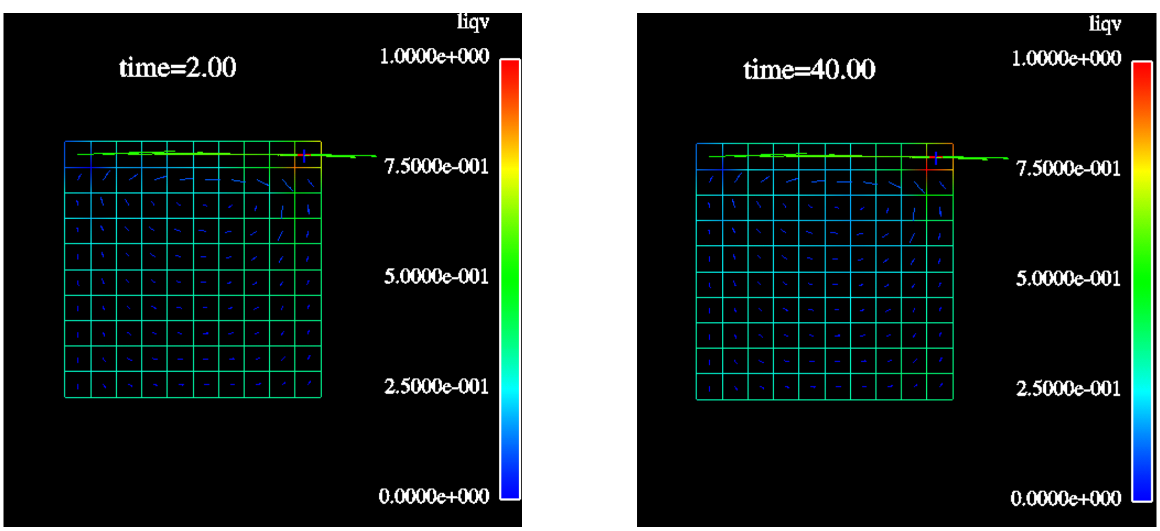

Figure 9.4. Driven cavity velocity field at early time and steady-state conditions.

9.4.1.2 Broken Dam

In this problem, a 1 m length in a 4 m long box is initially filled with water. The remaining portion of the box is filled with air. At the beginning of the calculation, the water is allowed to crash down and spread across the box as the “dam” breaks. Results showing the position of the attachment point of the water at the base of the box as a function of time compare very well with experiment. The maximum error is less than three percent from the time the dam breaks to the time the attachment point at the edge of the crashing wave reaches the far edge of the box. Figure 9.5 shows the wave front at different times during the calculation.

9.4.1.3 Rising Bubble

In this problem, a 1 m tall by 1 m wide box is initially filled with a uniform air/water mixture of 50% void fraction. At time zero, gravity begins to pull the water down to the bottom of the box, while the air rises to the top of the box. Results have not been compared with any experimental data at this time, but the expected trends are observed, as shown in Figure 9.6. The red (top of the scale) color represents water, while the blue (bottom of the scale) represents air.

9.5 Next Steps

The Lagrangian particle phase in TEXAS-3D will first be implemented for only one particle and without fragmentation. Plans for benchmark calculations to check for proper motion and heat transfer characteristics within the code have been made. Once these capabilities have been demonstrated, fragmentation and multiple particles will be introduced.

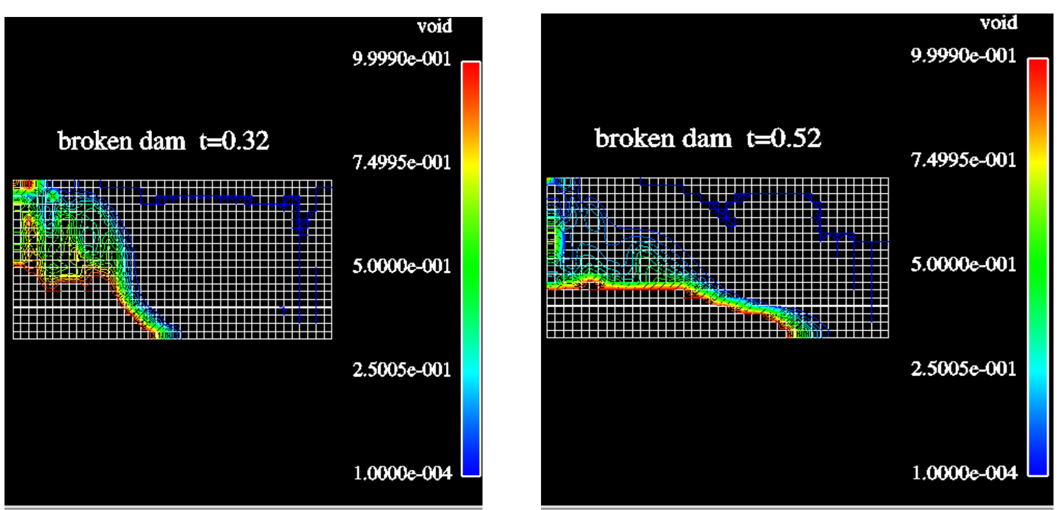

Figure 9.5. Broken dam wave front position at two different times.

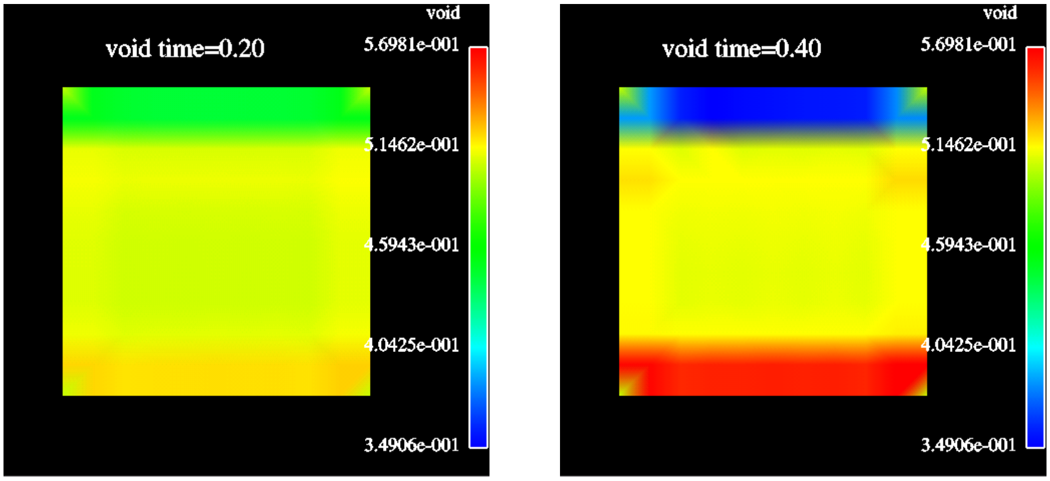

Figure 9.6. Rising bubble void fraction at two different times.

References for Section 9

[1] T.T. Utschig, "Nuclear Energy from Pulsed Power and Associated Dust Transport Calculations," Proceedings of the International Conference on Future Nuclear Systems, Global '99, "Nuclear Technology – Bridging the Millennia", Snow King Resort, Jackson Hole, WY (August 29 - September 3, 1999).

[2] T.G. Theofanous, W.W. Yuen, K. Freeman, and X. Chen, "Propagation of Steam Explosions: ESPROSE.m Verification Studies," Advanced Reactor Severe Accident Program, DOE/ID-10503 (August 1996).

[3] M.L. Corradini, J. Murphy, S. Nilsuwankosit, D. Pineau, B. Shamoun, J. Tang, and S. Wang, "Fuel-Coolant Interaction Analyses with TEXAS-V Vapor Explosion Model," University of Wisconsin Nuclear Safety Research Center Report.

[4] B. Badger et al., "LIBRA – A Light Ion Beam Fusion Conceptual Reactor Design," University of Wisconsin Fusion Technology Institute Report, UWFDM-800 (July 1989).

[5] T.T. Utschig, "Calculations for Surge Tank Heat Transfer in LIBRA-LiTE," Independent Study Report, NEEP 690, UW-Madison (1994).

10. Preliminary Design of Confined EOS Experiments on Z

Experiments are in progress on Z and are expected on ZX where small (<< 1 g) samples are shocked by magnetic pressure in the MITLs or in the current return can of a shorted load [1, 2]. Similar experiments, where z-pinch x-rays are used to drive shocks, are also in progress on Z. It is expected that a desire to perform such experiments with materials that are either toxic or radiologically hazardous will arise. In the experiments, a strong shock, generated by the MITL or return can current, passes through the material and carries the sample in the direction of the shock. On the other hand, in the x-ray experiments, some material is vaporized and blown back toward the source, with most of the material going away from the source. In the process, the sample in converted to vapor or small fragments. If the vapors and fragments in a hazardous material experiment are allowed to freely move throughout Z or ZX target chamber, the impact on safety, operations and waste disposal are obvious. A system to contain hazardous vapors and fragments would therefore be very beneficial to Z and ZX. Here, we suggest a system to contain hazardous vapors and fragments on Z and/or ZX that have been devised at the University of Wisconsin. We will also suggest experiments to perform on Z and future analysis we wish to perform on this system.

Initially, we suggested a containment system that is roughly conical or triangular, with the point of the cone or triangle placed directly behind the sample. This system is designed to recover samples that are placed on the MITLs. A system to recover x-ray driven samples or those on a current return can would be different and probably be related in some way to the presently existent diagnostics box. Cones may be more effective in the long run; triangles, easier to fabricate and test in initial experiments. A schematic picture of the containment system is shown in Figure 10.1. This concept assumes that the entire sample is directed upward.

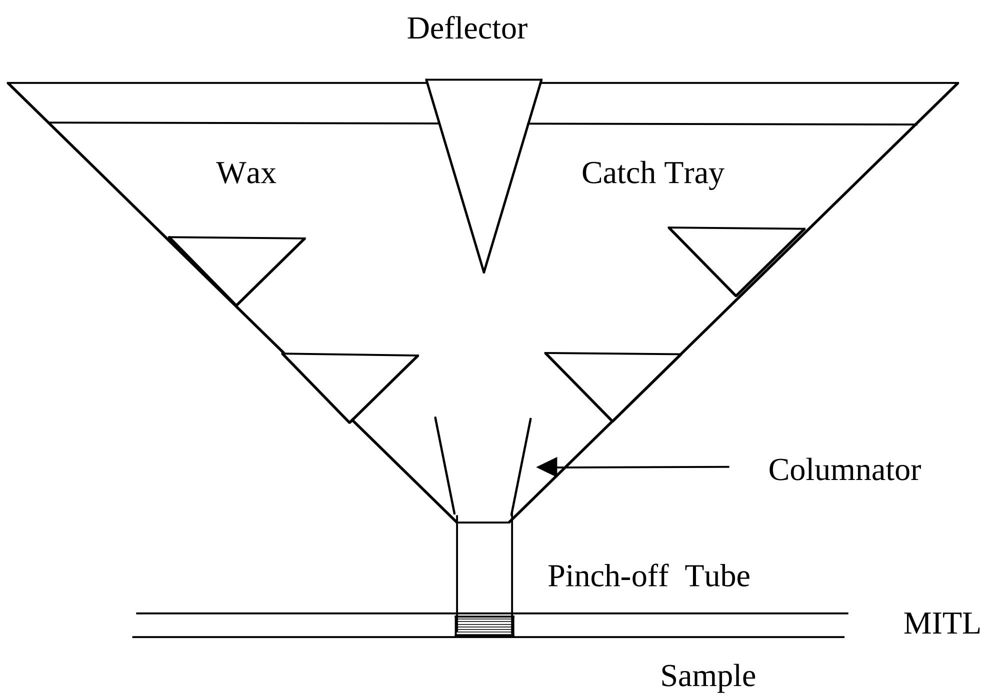

Figure 10.1. Schematic picture of containment system.

The containment system uses a columnator and a deflector cone or wedge to direct the sample remnants into a sticky wax and a series of catch trays, where the material is trapped. The columnator also keeps hazardous pieces from falling out of the containment system before the system is sealed. A pinch-off tube allows the containment system to be sealed after the shot with the material inside. The picture does not show how fiber optics could be put into the system for VISAR diagnostics of the shock. It also does not show that the walls of the system must be thick enough to sustain the internal pressure and impulse from the sample remnants. The containment system could be made of steel or any other strong material. A detailed analysis of the system has not yet been performed, so the dimensions are yet unknown. The energy in the sample remnants needs to be known before we can proceed with analysis. We expect that a cone or triangle 15 cm high by 15 cm across the base would be sufficient.

We propose that this type of containment system be tested on a Z shot. Perhaps on a shot where magnetically generated shocks are already planned, it would not be too much additional effort to build and place such a device. We would suggest that a confinement system could be machined into two halves of a block of steel. Each half would be 2.5 cm thick and the machining depth would be 1.25 cm. A deflection triangle and catcher trays could either be machined into the blocks or placed in after a cavity is machined. Columnator fins and a pinch-off tube could then be added and the assembly bolted together. VISAR fiber optics could be added during final assembly. A first test would just confirm that the system is not breached. Any problems of integration into the Z system would be worked out during the first test. After the shot, the system would be opened and the trapping of sample material in the wax and catch trays, which should be painted with something sticky, would be confirmed. The sizes of sample fragments would be measured. On subsequent tests, the system could be instrumented to measure the dynamics on the system and the particles in it. This, or an experiment without the containment system, needs to measure the velocity of the debris plume, a needed input for calculations of containment system behavior. In addition, a sample whose fragments can be detected in the Z chamber could be shot to confirm that the sample remnants remain trapped in the system. As part of these experiments, the UW would perform 1-D BUCKY [3] code simulations of the shock transit through the sample and response of the system to the debris loading.

References for Section 10

[1] C.A. Hall, et al., "Aluminum Hugoniot Measurements on the Sandia Z Accelerator," 41st Annual Meeting of the APS Div. Plas. Phys. (Seattle, WA, November 1999), Bull. APS <u>44</u>, 104 (1999).

[2] J.R. Asay, et al., "Insentropic Compression of Iron on the Z Accelerator," 41st Annual Meeting of the APS Div. Plas. Phys. (Seattle, WA, November 1999), Bull. APS <u>44</u>, 104 (1999).

[3] R.R. Peterson, et al., "The BUCKY and ZEUS-2D Computer Codes for Simulating High Energy Density ICF Plasmas," Fusion Technology <u>30</u>, 783 (1996).

11. Planning of Experiments on Z

The Z accelerator is a unique facility for performing high x-ray fluence experiments [1]. One subset of experiments that could be done are those related to inertial fusion energy (IFE) target chamber dynamics. In IFE, target chamber dynamics (TCD) is an integral part of the target chamber design and performance. TCD includes target output, deposition of target x-rays, ions and neutrons, vaporization and melting of target chamber materials, radiation-hydrodynamics in target chamber vapors and gases, and chamber conditions at the time of target and beam injections. An understanding of TCD is required to design a target chamber that is economically viable, and does not pose a threat to safety or the environment. Computer codes have been developed that model TCD phenomena. BUCKY [2], written at the University of Wisconsin, is one example of such a code. BUCKY is a 1-D Lagrangian radiation-hydrodynamics computer code, with realistic atomic physics, multi-group radiation diffusion, x-ray and ion deposition physics, and vaporization, melting and re-condensation physics. Validation of codes with small but relevant experiments is critical because full-scale experiments will not be possible until ignited target experiments occur on lasers or z-pinches.

Pulsed power machines provide a unique environment in which to perform IFE-TCD validation experiments in two important ways: they do not require the very clean conditions which lasers need and they currently provide large x-ray and ion energies. Z-pinch experiments on the Z accelerator at Sandia National Laboratories (SNL) presently can produce approximately 2 MJ of > 100 eV blackbody x-rays in a several ns pulse. The spectrum is colder than what is expected from IFE targets, but the achievable fluences and pulse widths are IFE relevant. X-ray vaporization and chamber gas radiation-hydrodynamics can be studied with Z as an x-ray source. These x-rays could produce high energy density plasmas that mimic phenomena in target explosions that lead to target emissions. The RHEPP accelerator at SNL can produce several J/cm^2 of several 100 keV ions of many species and IFE relevant pulse widths, which could be used to simulate target ion stopping in vapors and gases and ion melting and vaporization.

Here we will propose several such experiments. They are broken down into the following areas:

- Target output
- Target chamber gas radiation-hydrodynamics
- X-ray vaporization
- Ion beam deposition and response.

We have performed some preliminary design of experiments in these four areas. By preliminary, we mean conceptual pictures of the experiments with some approximate scaling of parameters. Pre-shot computer simulations have yet to be performed.

11.1 Target Output

Target output (x-rays, ions and neutrons) drives the TCD. For direct-drive targets, the major non-neutronic component to the output is energetic ions from the rapid expansion of the ablator after target ignition and burn. Computer simulations with BUCKY have predicted that the plastic ablator of the SOMBRERO target expands at 0.5 cm/ns, which leads to C ions with an energy of 1.7 MeV. The density of the target chamber required to stop these ions is sensitive to the ion energy. The presence of such energetic ions needs to be confirmed with experiments. The BUCKY calculation assume that all of the ions in a Lagrangian shell are moving at the same speed, a conjecture that has not been tested experimentally.

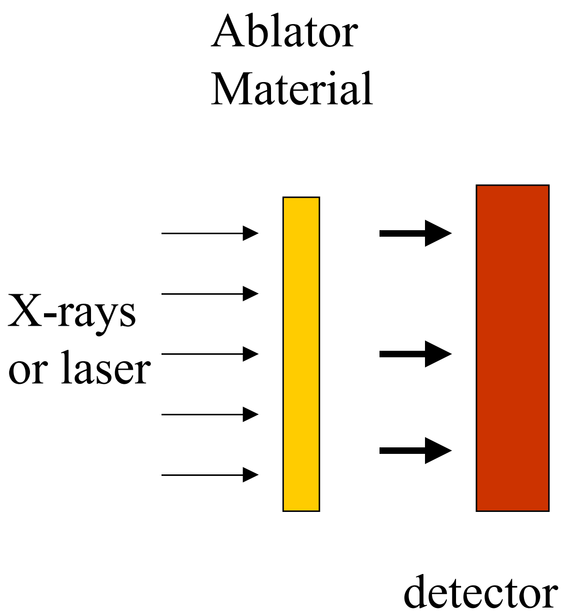

Figure 11.1. Target ion output experiment.

An experimental concept is sketched in Figure 11.1. A foil of ablator material is driven on one side by Z x-rays and the energy of the ions in the resulting expansion is measured. If one places a 100 μm thick CH (Paralene-N) foil 10 cm from a 2 MJ x-ray burst from a z-pinch, the x-ray fluence is 1600 J/cm^2. If the deposition length in the CH, Δx is 1 μm, if the deposition is fast enough that heat transfer and expansion are not important, and if the Grueneisen coefficient for CH, Γ, is 2, then the pressure generated on one side of the foil,

$$P = \frac{\Gamma F}{\Delta x} \quad ,$$

is 3.2 x 10^7 MPa. If the density of the CH, ρ, is 1 g/cm^3, the foil is accelerated at

$$a = \frac{P}{\rho \quad l} \quad .$$

The foil would reach a velocity of

$$V = a \, \Delta t \, ,$$

where V is 1.5 x 10^8 cm/s if the x-ray pulse width, Δt, is 5 ns. This is close enough to the BUCKY prediction for the SOMBRERO target to make the experiment relevant. The key to achieving these conditions is a short enough deposition length, which may require a high atomic number dopant in the plastic.

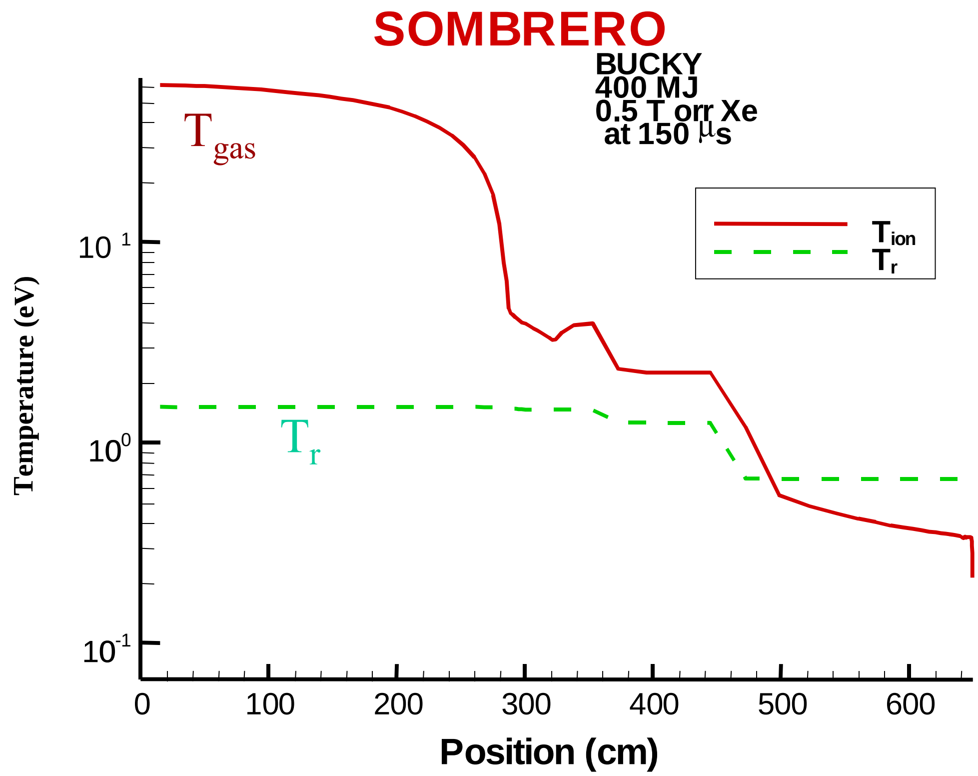

Figure 11.2. Sample target chamber gas radiation hydrodynamics conditions.

11.2 Target Chamber Gas Radiation-Hydrodynamics

In gas protected IFE target chambers, the radiation-hydrodynamics induced in the gas by target output deposition is of great importance. The gas absorbs the target x-rays and debris ions and protects target chamber structures from direct damage. However, the gas becomes hot enough to radiate energy onto the structures or launch shocks that can be damaging. The rate that energy is radiated to the structures must be slow enough for thermal conduction to carry away the heat or the structure will become damaged.

BUCKY models the radiation-hydrodynamics of hot gases in 1-D. The conditions in the SOMBRERO target chamber gas as calculated by BUCKY are shown in Figure 11.2. The gas is 0.5 torr of Xe. The gas and the radiation in this case are at quite different temperatures. The radiation transport is calculated within a radiation diffusion model, which requires that the radiation is nearly in equilibrium with the medium. Therefore, the BUCKY model may be pushed beyond the limits of validity. Experiments are required to validate that BUCKY is doing this calculation correctly.

Such an experiment is shown in Figure 11.3. Here, we propose to use x-rays from Z in a hohlraum to heat a truncated cone filled with gas to about 100 eV. The gas should be thin enough that the radiation temperature and material temperature are out of equilibrium, as in the SOMBRERO case.

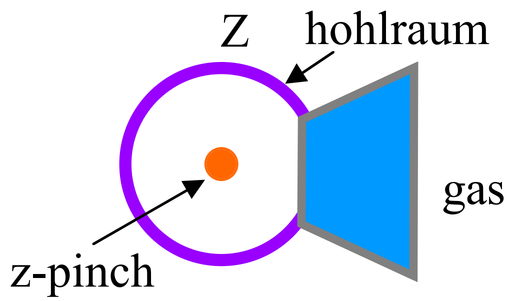

Figure 11.3. Z experiment to study IFE target chamber gas radiation-hydrodynamics.

Diagnostics might include microdots of dopant they would emit x-rays when the radiation wave reaches various positions along the cone.

Figure 11.4 shows how the radiation emitted by the gas is quite sensitive to the opacity of the chamber gas. These BUCKY results show how the radiation power reaching the wall of the SOMBRERO chamber changes as the Planck opacity is varied. The higher the Planck opacity, the greater the radiant power on the wall. This is because radiation emission from the gas limits the radiant heat flux, the gas being optically thin. The opacity of the Xe gas is calculated with the EOSOPC code [3]. These opacity calculations need validation through experiment. An experiment like that shown in Figure 11.5 would suffice. Here, a volume of gas is tamped to keep its density constant and is heated by Z x-rays. The opacity in the visible and UV are of greatest interest in this problem, so an appropriate visible and UV source would then probe the gas and a transmission spectrum be measured. A measured frequency dependent opacity could then be compared with that predicted by the EOSOPC code.

11.3 X-ray Vaporization

In some IFE chamber concepts, x-rays are allowed to reach the surface of chamber structures. BUCKY models this. Using the available x-rays on Z, which realistically can reach fluences of 1000 J/cm^2, IFE chamber materials such as Flibe, Li and PbLi can be studied. This fluence is well above the typical IFE chamber fluences in these concepts of a few 100 J/cm^2. The BUCKY predictions of the amount of vaporized material and the recoil impulse can be validated.

11.4 Ion Beam Deposition and Response

In these concepts allowing vaporization, the vapor is created before the debris ions from the target reach the structure. The ions deposit in the vapor and heat it, causing it to radiate to the structure and possibly causing more vaporization. The RHEPP accelerator can provide ions of reactor relevant energy, species, pulse width and fluence. A vapor could be created by a pre-pulse with ions, since RHEPP is rep-rateable. The ions from the diode would then stop in the vapor, heating it and causing it to radiate. A time-dependent visual spectrometer would then validate BUCKY predictions of the radiation emitted from the vapor.

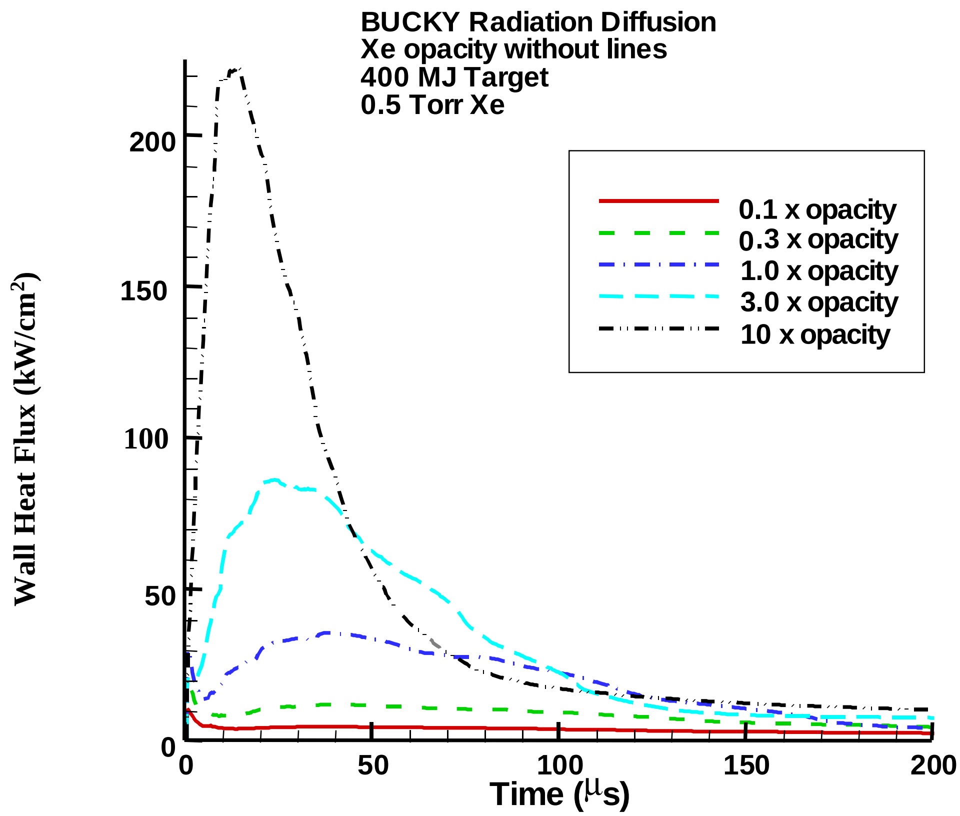

Figure 11.4. Sample target chamber gas radiation hydrodynamics are shown to be sensitive to Planck opacity.

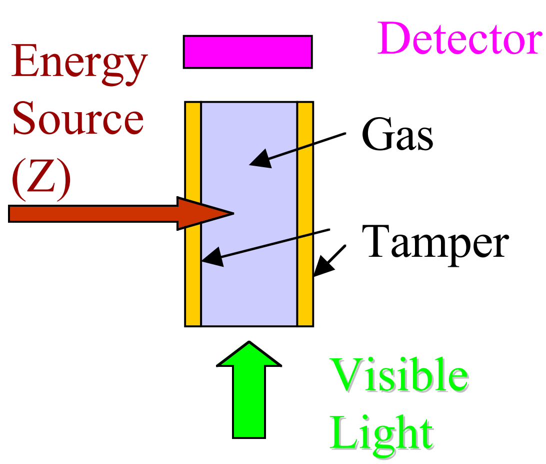

Figure 11.5. Gas opacity experiment.

References for Section 11

[1] M.K. Matzen, “Z Pinches as Intense X-ray Sources for High-Energy Density Physics Applications,” Phys. Plasmas 4, 1519 (1997).

[2] R.R. Peterson, et al., “The BUCKY and ZEUS-2D Computer Codes for Simulating High Energy Density ICF Plasmas,” Fusion Technology 30**,** 783 (1996).

[3] P. Wang, “EOSOPC - A Code for Computing the Equations of State and Opacities of High Temperature Plasmas with Detailed Atomic Models,” University of Wisconsin Fusion Technology Institute Report UWFDM-933 (December 1993).

12. Conclusions

The work performed by the Fusion Technology Institute at the University of Wisconsin-Madison in CY 1999 has highlighted some of the critical issues that face the current operators of Z, as well as those facing operators of the potential ZX or X-1 facilities. This work has illustrated the complex relationship between the target output spectra and the chamber gas. It has also highlighted the difficult issues associated with the containment of target debris, radioactive dust and fusion products such as neutrons. We clearly have not solved all of the immediate problems nor have we elucidated all of the future hurdles that will have to be overcome. However, the work has illustrated the importance of developing analytical tools and computer models early in the design of a future Z pinch facility. The tools need to be benchmarked against experimental conditions, at least as close as they can be given the limitations of present devices. Such development takes time and it is important to encourage researchers to "think outside the box" now, before the demands of a construction project consume all of the human and financial resources that can be devoted to this kind of endeavor.

Acknowledgement

This work has been supported by the U.S. Department of Energy.